A chemical kinetics-based approach to predict uncontrolled self-ignitions in Hydrogen Internal Combustion Engines

Politecnico di Bari

Department of Mechanics, Mathematics and Management

MECHANICAL AND MANAGEMENT ENGINEERING

Ph.D. program

SSD: IIND-06/A – Fluid Machinery

Final Dissertation

A chemical kinetics-based approach to predict uncontrolled self-ignitions in Hydrogen Internal Combustion Engines

by

Daniyal Altaf BALOCH

Supervisors:
Prof. Riccardo AMIRANTE
Prof. Elia DISTASO

Coordinator of Ph.D. Program:
Prof. Giuseppe CASALINO

Course n° 37, 01/01/2022 – 31/12/2024

Politecnico di Bari

Department of Mechanics, Mathematics and Management

MECHANICAL AND MANAGEMENT ENGINEERING

Ph.D. program

SSD: IIND-06/A – Fluid Machinery

Final Dissertation

A chemical kinetics-based approach to predict uncontrolled self-ignitions in Hydrogen Internal Combustion Engines

by

Daniyal Altaf BALOCH

Referees:
Prof. Gianluca D'ERRICO

Prof. Paolo Antonio CARLUCCI

Supervisors:
Prof. Riccardo AMIRANTE

Prof. Elia DISTASO

Coordinator of Ph.D. Program:
Prof. Giuseppe CASALINO

Course n° 37, 01/01/2022 – 31/12/2024

Acknowledgements

This work has emerged from a research project funded as a Ph.D. scholarhip through "Programma Operativo Nazionale Ricerca e Innovazione 2014-2020, risorse FSE REACT-EU" under the supervision of Prof. Riccardo AMIRANTE and Prof. Elia DISTASO.

I would like to extend my sincere gratitude to my supervisor Prof. Riccardo Amirante who provided me with a large degree of freedom to shape the project according to open ideas as well as for his generous support.

I give my special thanks to my supervisor as well as my close friend Prof. Elia DISTASO for the endless technical discussions on the present work and beyond. His contributions, dedication and passion for engineering has made me a better and improved version of myself as a researcher. I thank my colleague and friend Dr. Giuseppe Calò, for intense and comprehensive discussion on chemical kinetics, engines and more.

It would not be complete without extending my splendid gratitude to my closest colleagues and friends, Francesco Sciatti, Vincenzo di Domenico and Lazzaro Zagaria for their technical discussions, coding assistance and the essential daily time-outs for some fresh air and memorable times. A very special thanks once again to my best friend Dr. Francesco Sciatti, his wife AnnaMaria Manzari and their parents for their friendship and care just like a family.

The final paragraph is dedicated to the love of my life, my beautiful and loving wife Dr. Zoha Noor who became a part of my life's journey during my Ph.D., becoming my motivation and passion to succeed even more than I ever dreamt of. Her love, care and guidance has undoubtedly made me a better version of myself.

The most important gratitude is reserved for my parents,
brothers, aunts and uncles
who have brought me up as an honest, hardworking and a loving man.
All these years of education, devotion and hard work are dedicated

to my Ammi , Abbu
and family

who have always accentuated to keep searching for more.

To infinity and beyond.

Abstract

The primary objective of the present work is to correlate the hydrogen explosive characteristics with internal combustion engine design parameters, particularly the engine compression ratio. An approach that couples the knowledge about H_2 chemical behaviour, and the in-cylinder charge thermodynamic state, has been conceptualized in the form of a unified plot to visually inspect the likelihood of an auto-ignition event. The plot cautions the possible occurrence of autoignition if the state of the charge inside the engine cylinder reaches thermodynamic conditions beyond the explosion limit curve. Having at hand such a tool enables one to cautiously design future experiments to prevent possible damage because of extreme stresses due to an undesired autoignition event.

The results of the analyses in the present work have translated into defining a maximum limit on the compression ratio that can be proposed at pre-defined intake thermodynamic state, mixture composition, engine geometry and engine speed. Predictions based on recently developed chemical mechanisms were employed for the analyses, exploiting the well-established knowledge about the chemical kinetics of hydrogen oxidation.

Thus, zero-dimensional numerical simulations were performed. Such an approach avoids also the limitations associated with experimental procedures. To evaluate the maximum safe compression ratio, both a static and a time-based approach have been employed to study the vicinity of a thermodynamic state to the autoignition limit i.e., the explosion limit of hydrogen. Three possible criteria for the definition of a maximum safe geometrical compression ratio were developed and analysed. The present work has then been finally ensembled in the form of an empirical correlation involving intake pressure, intake temperature and equivalence ratio as the variables.

Furthermore lubricant oil as a contaminant seeping through the compression rings of a piston in an internal combustion engine, is modelled to evaluate the distribution of mass and temperature inside a droplet of n-hexadecane using 0D-simulations to evaluate the variation of ignition delay time within the droplet in gas-phase and its effect on the local concentration diluting the pure hydrogen in the vicinity and hence increasing the reactivity causing an early source of self-ignition.

A final study concerning developing detonations from hot spots is carried out to understand the effect of a temperature gradient other than 'linear' within the hot spot that could change the detonation response diagrams and subsequently the modes of reacting front propagation. Such detonations with high peak pressures are detrimental to components inside an internal combustion engine and therefore the need to study any possibility of its occurrence is crucial to a better understanding of the design.

Contents

List of Figures

List of Tables

Nomenclature

Abbreviations	
aTDC	after Top Dead Centre
bTDC	before Top Dead Centre
BDC	Bottom Dead Centre
CI	Compression Ignition
DI	Direct Injection
ECR	Effective Compression Ratio
GCR	Geometric Compression Ratio
HCCI	Homogenous Combustion Compression Ignition
HICE	Hydrogen Internal Combustion Engine
ICE	Internal Combustion Engine
KCl	Potassium Chloride
MSGCR	Maximum Safe Geometric Compression Ratio
NHRR	Net Heat Release Rate
PFI	Port Fuel Injection
RCM	Rapid Compression Machine
RPM	Revolutions Per Minute
SI	Spark Ignition
ST	Shock Tube
STP	Standard Temperature and Pressure (1 atm, 20 $°C$)
TDC	Top Dead Centre
0-D	Zero-dimensional
Symbols	
Roman	
a	Crank radius
l	Connecting rod length
N	Engine speed [rounds per minute (RPM)]
p	Pressure
s	Piston displacement
T	Temperature
V	Volume

Greek	
ε	epsilon; ratio of ECR to GCR
k	Specific heat constant
t_{TDC}	Time to reach the TDC
τ_{ID}	Ignition delay time
ϕ	Equivalence ratio
θ	Crank's angle of rotation
θ_{AI}	Auto-ignition crank angle
ω	Angular engine speed [rad/sec]

1 Introduction

Internal combustion engines have undoubtedly proved to be the pinnacle source of power for automotive propulsion and commercial transport across the globe since its very first introduction back in 1794 by Robert Street who patented the first ICE to use liquid fuel (petroleum). Spanning the ground-breaking discovery of four-stroke and two-stroke thermodynamic cycles along which came the spark-ignition (Petrol) and compression-ignition (Diesel) engines, propulsion technology has ever since been relying on these fundamental inventions that have now evolved into significantly cleaner and efficient versions of the originals through deliberate development of automotive technologies throughout the years.

With the onset of global warming since the start of the Industrial Revolution back in 1760, the use of fossil fuels and therefore the product of their combustion, dominantly CO2, has brought a trend in climate change which unequivocally has given rise to the global average temperature to alarming levels adversely affecting the earth's ecosystem. This major global concern has led the policy makers and the automotive industry to invest in incentives that could bring a paradigm shift, potentially reversing the harmful effects to the environment because of uncontrolled harmful hydrocarbon emissions as a result of burning conventional fuels in internal combustion engines.

As a consequence of this , the recent introductions of alternative automotive powertrain architectures incorporating either hybrid or zero-Carbon emissions stand-alone units like those of electric or carbon free fuels like Hydrogen, have opened an evolving challenge to establish a stable infrastructure that could support the decisions behind each powertrain architecture.

1.1 Compression ratio – a crucial engine parameter

Under the European Union Green Deal [1], the focus to develop zero-carbon emission engines has directed the automotive sector towards dedicated research on Hydrogen Internal Combustion Engines (HICEs). The performance and emission targets of an Internal Combustion Engine (ICE) pursued by the industry is pushing the development of new technologies [2], [3], [4], [5], new combustion modes [6], [7], [8], [9] and control strategies [10], [11], [12] or modifications of well-known existing setups like charge motion [13], [14], [15], fuel injection strategy and control [16], [17], [18], and turbocharging [19], [20]. However, the most fundamental variable that is chosen in any design phase is the compression ratio which imposes the peak thermodynamic states of the charge at the end of a compression stroke. In an ideal gas cycle, the thermal efficiency increases with the compression ratio. However, this cannot be increased indefinitely, because increasing it also raises the peak pressure and temperature of the charge, and consequently raises the knock propensity as well. Therefore, to extract the maximum performance figures, the compression ratio needs to be high enough to achieve the peak thermodynamic states [21] while at the same time low enough to avoid adverse effects like knocking. Therefore, an effective balance needs to be achieved within these contradicting parameters. A high compression ratio limits the mixture composition to be lean [22], while a lower compression ratio can allow a richer mixture to undergo a normal combustion. The achievable performance for an ICE is usually a compromise between these two and other such parameters [23]. This aspect has been considered in the present work to arrive at an analytical solution towards selection of a compression ratio based on mixture composition and intake state of the charge.

1.2 Abnormal combustion in HICEs

While trying to maintain the balance between performance and selection of geometry for a HICE, the industry's objective to acquire the correct design parameters has mainly been limited by the occurrence of pre-ignition [24], [25], [26]. A pre-ignition event can be defined as the ignition of the charge mixture before, when it is "intended by design". Usually, in literature and the automotive industry, pre-ignition is almost always considered to be an ignition that happens before the initiation of a spark and therefore is usually associated to Spark Ignition (SI) engines. However, for the purpose of this work and for general clarity, one should refer to the intended start of combustion time. For instance, in a

homogenously compressing mixture, if the charge auto-ignites before the intended time due to an uncontrolled increase in pressure and temperature, it can still be considered a pre-ignition. Pre-ignitions can result in detrimental effects in different ways depending on the fuel metering strategy being Direct Injection (DI) or Port Fuel Injection (PFI). Abnormal combustion such as a backfire in PFI H_2 engines have been reported [26] to significantly reduce the volumetric efficiency [27] apart from the physical damage to intake and fuel systems [28], [29]. The causes associated with backfires have been mainly attributed to high temperature residual exhaust gas and hot spots [30], [31] which indicates the need to control a basic thermodynamic state of the charge, namely, the temperature. In DI engines, pre-ignitions could be caused by thermal and mass inhomogeneities around the injected hydrogen jet. The mass inhomogeneity allows different fuel-air equivalence ratios (ϕ) around the injection where a richer mass fraction of the mixture may pre-ignite the charge. Thermal inhomogeneities promote temperature gradients within the mixture around hot spots such as high temperature exhaust deposits and spark plug tips.

1.3 Lubricating oil contamination – a key cause of pre-ignitions

One of the major reasons of pre-ignition in HICEs was through contamination of the pure H_2-air charge with lubricating oil. This contamination alters the mixture composition and therefore its chemical state promoting a much earlier ignition. The presence of lubricating oil in the primary charge and its role in pre-ignition phenomenon have been largely studied in engines fuelled with conventional gasoline [32], [33], [34], [35], [36], and, more recently, these investigations have been extended by Distaso et al. to the case of hydrogen [37], [38]. Furthermore, it should be considered that a direct link between the formation of soot particles and lubricant oil was demonstrated, regardless of the fuel feeding the engine [39], [40], [41]. The presence of hydrocarbons with long chains enables soot precursor formation in low-carbon content fuels opening the way to carbonaceous deposit formation [42], [43], [44] and unveiling a possible secondary way by which lubricant oil can promote pre-ignition events.

Undesired combustion of hydrogen can also be associated differently to Spark Ignition (SI) or Compression Ignition (CI) engines. In SI engines, engine knock or detonation can be caused by the interaction between the propagating flame front and the detonation wave [45], [46] generated at a hot spot within the end-gas. To understand the possibility of such an event, it is crucial to know the chemical and

thermodynamic state of the end-gas which may or may not ignite due to that hot-spot. On the other hand, pre-ignition in hydrogen fuelled SI engines, i.e., ignition of charge before the spark has been struck, can be explained by the hydrogen-oxygen chain reaction [47]. In CI engines, where combustion of the charge occurs as a result of a desired auto-ignition, the higher compression ratios ensure that the peak temperature and pressure values inducing an auto-ignition are reached at the end of the compression stroke. Auto-ignition of any fuel in air, is a consequence of the underlying chemical reactions that promote such a transition which leads to understanding the chemical kinetics of the fuel. Engines operating on more advanced combustion modes, like the Homogenous Combustion Compression Ignition (HCCI) engines, are limited at high load conditions due to rapid pressure rise rate, short combustion duration and ringing operation [48]. Ringing operation in HCCI engine is one of the major challenges at high engine load conditions [49], which limit the HCCI engine operation range and can also damage engine parts and is characterized by ringing intensity which also can be predicted by chemical kinetics of the fuel [50].

1.4 The significance of explosion limits in HICE design

The combustion event in an ICE needs to be controlled and optimized to acquire the maximum work from the full engine cycle while avoiding undesired effects such as knocking and overheating of crucial components. To avoid any undesired autoignition conditions for hydrogen, its explosion limit must be studied in detail. The explosion limit of a fuel-oxidant mixture is the locus of pressure and temperature values that distinguish between an explosive and non-explosive reaction of the said mixture composition. This limit, in practice, is an isometric line with a constant value of ignition delay time. Hydrogen has a peculiar z-shape explosion limit as first reported by B. Lewis and G. von Elbe [51] for H_2-O_2 mixture at stochiometric conditions experimentally acquired in a constant-volume spherical chamber. The main emphasis in literature has been on the ignition delay time which is used to validate numerical kinetic mechanisms compared to experimental data: e.g., ignition delay times for H_2-air mixtures have been experimentally observed in rapid compression machines [52], [53] and shock tube experiments [54] under varied conditions.

1.5 Goals and structure of this work

The aim of the present work is to provide possible systematic approaches for guiding the choice of geometrical and operating parameters of a HICE, exploiting the well-established knowledge about hydrogen chemistry, to be employed in a preliminary design stage of the engine. To achieve this purpose, the information related to the chemistry of hydrogen oxidation process needed to be translated in terms of ICE design. The first step consisted in the analysis of existing data about the explosion limit of hydrogen available in the literature. However, since these data are generally influenced by the employed apparatus, numerical chemical kinetics of hydrogen was chosen to serve the purpose and avoid the limitations incurred through experimental setups. The kinetic mechanism most suitable to the selected range of operation was chosen from literature and used in Zero-dimensional (0-D) numerical simulations carried out using Ansys CHEMKIN Pro code [55] to reproduce the explosion limits. Different mixture compositions of hydrogen with air and pressures and temperatures spanning in wide ranges were considered in order to cover possible operating range of a HICE, encompassing low, partial, and full load conditions. As a result, a wide database of thermodynamic states along the explosion limits characterized in terms of mixture reactivity (H_2 reactivity map) was developed and used in subsequent calculations.

1.5.1 Static, time-based and integral criteria for GCR calculation

Two general approaches to evaluate a safe Geometrical Compression Ratio (GCR) were proposed and analysed in the present work. The first can be considered a "static criterion" since it is based on the comparison between the in-cylinder motoring conditions in the proximity of the TDC and the H_2-air explosion limit. A range of peak operating points rather than fixed values were considered to evaluate a safe GCR. A time-based approach was then developed by comparing the instantaneous charge ignition delay time (τ_{ID}) with the time remaining to reach the TDC (t_{TDC}) as the charge mixture is compressed through a piston displacement (tangency criterion). For each piston position, the corresponding instantaneous ignition delay time of the mixture (τ_{ID}) was calculated by means of the reactivity map developed earlier to evaluate any possibility of auto-ignition along the compression stroke. The cumulative effect of heat release during compression has also been considered in order to develop a more conservative method towards the definition of a safe GCR for the engine (integral criterion).

1.5.2 Maximum GCR – an empirical correlation

In the final part of the work, the synergized result of the above objectives has then been assembled into a simple empirical correlation to evaluate the autoignition probability of the charge. The expression covers a wide range of typical engine operating points with intake pressure ranging from 1 to 1.5 bar, intake temperature from 300 to 400 K and equivalence ratio from 0.1 to 1. The motive behind this thorough yet fundamental approach is to build a strong foundation for HICE development using a systematic approach that is consistent and methodical.

1.5.3 Lubricating oil and early onset of self-ignition

Moving onwards from pure H_2/air mixtures, a further investigation is carried out if the lubricant oil chemical characteristics can be at the basis of the onset of certain uncontrolled self-ignition modes of the charge. Considering a lubricant oil droplet suspended in a H_2/air environment, an analytical model was developed to derive essential information about mixture composition and thermodynamic conditions that might establish where oil contamination occurs. The results were used to initialize zero-dimensional numerical simulations performed in the OpenSMOKE++ framework with the aim of highlighting charge reactivity variations induced by the presence of oil vapour in the vicinity of an oil droplet. A reduced chemical model, developed for this very purpose in a previous recent work, was employed in the simulations for emulating the reactivity properties of the $H_2/oil/air$ mixture.

1.5.4 Evolving detonation from hot spots – 1D transient simulations

Abnormal combustion due to presence of hot spots, requires a detailed analysis of the reacting front propagation evolving as a result of these hot spots inside an engine's combustion chamber interfering with the combustion wave propagation originated by design through spark in SI or desired auto-ignition in DI HICEs. Hotspots, being localized regions of temperature gradients, develop into detonation in different modes that depends on hot spot size as well as the temperature gradient and its shape within the hot spot. In this work, the detonation through an exponential shape of the temperature gradient is studied numerically by solving transient auto-ignition processes of stochiometric H_2/air mixtures initiated by non-uniform exponential initial temperatures in a one-dimensional "planar" domain are studied and compared with linear gradients.

The chapters to follow can be outlined as below:

Chapter 2 The application of hydrogen-air explosion limits to engine relevant conditions is explored. Numerical reaction mechanism best suitable for our application is selected through comparison to available experimental data. A reactivity map encapsulating multiple explosion limits with specified ignition delay times is developed necessary to model an efficient equation to acquire instantaneous ignition delay times for any arbitrary thermodynamic state inside the combustion chamber.

Chapter 3 The maximum threshold on geometrical compression ratio of a hydrogen internal combustion engine is numerically calculated utilizing the explosion limits of H_2/air in relation to engine geometry and in-cylinder operating conditions. Three sequentially upgraded criteria that define the maximum GCR without auto-ignition of the charge are described in detail those being static, time-based and integral criteria.

An empirical correlation encapsulating the intake pressure, intake temperature and equivalence ratio of a H_2/air mixture is eventually developed based on the generated H_2 reactivity maps and the three criteria defined in this chapter.

Chapter 4 The onset of earlier self-ignition as compared to pure H_2/air mixtures is studied with lubricant oil as a contaminant. An analytical model with the aim of obtaining expressions for the temperature and species distributions in the region close to the droplet surface is developed to assess the spatial variation of the mixture ignition delay time, induced by the oil droplet without the need of performing complex and time demanding CFD simulations.

Chapter 5 The presence of hot spots inside the combustion chamber that form a source of locally high temperature sources leading to a locally propagating reacting front could evolve into sub-sonic or supersonic evolving detonations and hence resulting in

abnormal combustion. The temperature gradient as proved by earlier studies has a major effect on the type of detonation as well as its possibility. In this work, unlike previous works where the temperature gradient is taken as linear within the hot spot, an exponential trend of temperature is taken into consideration that is more representative of an actual hot spot. The difference is compared through 1D detonation simulations comparing the detonation response diagrams between the different trends of temperature profile within the hot spot.

2 H_2 explosion characteristics in engine relevant conditions

Ascertaining the possibility of autoignition during the compression stroke of an ICE, basing the analysis on the chemistry of the fuel-oxidant mixture, requires the knowledge of its self-ignition characteristics quantifiable through the assessment of its explosion limits. Such limits can be derived experimentally however the progress made in developing chemical kinetics schemes allows one to calculate them in a reliable way over a wide range of operating conditions without the need to incur costs associated with setting up experiments.

2.1 Experimental vs numerical data

Figure 2-1 shows the typical Z-shaped curve identifying the three explosion limits characterizing a H_2-O_2 mixture at stoichiometric conditions ($\phi = 1$). The limits were obtained from the most referenced data until today, namely those obtained by B. Lewis and G. von Elbe [51]. On the same graph, the thermodynamic region of interest in ICE applications is highlighted. Namely, in view of the typical in-cylinder conditions that can be established along the compression stroke of an ICE, the pressure p was defined to be between 1 and 100 $bars$, and the temperature T between 750 K and 1600 K. The lower temperature value is based on the lowest ignition temperature for a H_2-air mixture at a pressure of 100 bar. Numerically calculated ignition delay times for H_2-air mixtures between pressures of 5 and 30 bar performed in a previous work [38] suggested a temperature range between 860 and 1200 K. Thus, a lower temperature limit of 750 K seems to be appropriate for this study. The upper limit is chosen to account for peak temperatures achieved during the compression stroke of an engine having significantly higher compression ratios for comparison purposes (as it will be discussed later in the work).

The region on the left-hand side of the entire explosion limit curve in Figure 2-1 marks a 'non-explosive' region and that on the right-hand side, an 'explosive' one. The transition in explosivity from weakly to strongly explosive behaviour is delimited by the extended 2nd explosion limit (red dotted line) [56]. The extension differentiates between the dominant reactions happening in those temperature ranges, namely, HO_2 chemistry dominating on the left and $H+O_2$ branched chain mechanism speeding up the H_2 oxidation on the right of the extended 2nd explosion limit [38]. The focus, in this study, however, is restricted to the 3rd explosion limit only.

The usage of these experimental data available in the literature [51], [52], [54] for the definition of a limited operational region for a HICE needs a cautious approach. The data are generally influenced by the apparatus being used as well as the conditions under which the experiments are performed influence the ignition delay times for the mixture and hence significantly affect the calculation of a safe GCR for an ICE. This represented a crucial step towards the development of the results presented in this work. For instance, it is known that the relative position of the explosion limits significantly varies with the vessel size and wall material [51]. Although in the experiments by Lewis and von Elbe [51] the spherical chamber was coated with Potassium Chloride (KCl) to reduce the interaction of the reacting species with the walls, the effect on radical depletion/termination at the walls at both low and high pressures were non-negligible and consequently affected the measured ignition delay time values. To eliminate such external factors that affect or undermine the intrinsic chemical behaviour of the fuel, numerical chemical kinetics of hydrogen was chosen to serve the purpose and avoid the limitations incurred through experimental setups and determine H_2 explosion limits in engine-relevant operating conditions in addition to the added convenience to be pre- and post-processed with the ability to rapidly change either the reaction mechanism parameters or the engine operating conditions. This provides the feasibility to create large datasets for varying conditions of interest.

Unlike in the experiments where the explosion of the mixture was logged only if it occurred within an arbitrary time window of observation, with a numerical approach, this limitation is eliminated and therefore the ignition delay times for a sweep of temperature values at a given pressure can be evaluated as will be shown in Section 2.3. If the experimental explosion limit (Figure 2-1) represents an ignition delay time greater than, for instance, 1 second, it shall not prove to be a suitable explosion limit for ICE applications where ignition delay times much shorter need to be considered for a quantifiable comparison.

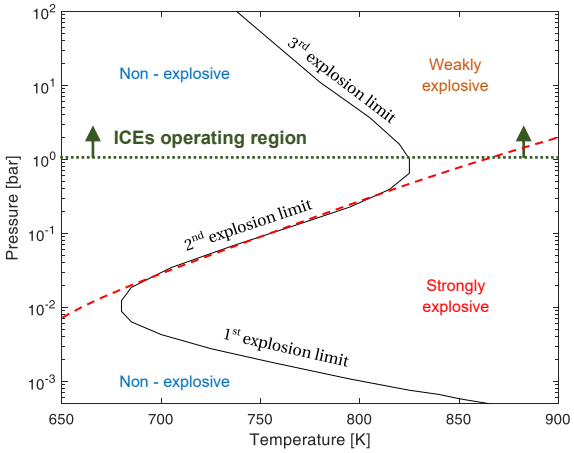

Figure 2-1 Experimental explosion limit [51] of H_2-O_2 mixture at $\phi = 1$.

2.2 Reaction mechanism selection

Chemical kinetic mechanisms found in literature have been validated through different experimental setups like Rapid Compression Machines (RCMs) [53] and Shock Tubes (STs) [54] to compare the ignition delay times τ_{ID}. RCMs, being the closest in construction to ICEs, should indeed provide τ_{ID} values that can be expected during an ICE operation. Therefore, at this point, the need to perform a critical analysis of existing mechanisms is introduced to select the one that is most appropriate and applicable within the range of operating conditions used for the purpose of this study.

Mittal et al. [52] compared four different mechanisms between RCM experimental data and 0-D constant volume homogenous batch reactor model simulations meanwhile also utilizing the effect of heat losses in the form of an "effective volume" term so that, consistent ignition delay times could be simulated. O'Connaire-2004 mechanism performed very well for pressures of $15, 30$ and $50\ bars$ between temperatures of 940 and 1060 K [52]. Validation results by Hu et al. [54] provided that among the twelve different kinetic mechanisms investigated in that work, the Kéromnès 2013 kinetic mechanism [57] estimated the ignition delay times with the least error across the entire pressure and temperature ranges in [54]. The capability of the Kéromnès 2013 kinetic mechanism in reproducing experimental data is reported in Figure 2-2 for the reader's convenience. Furthermore, Kéromnès et al [57] have validated the mechanism for different oxidation studies (ignition delay times, flame speed, species profiles) and for a wide range of pressures (1–70 bar), temperatures (900–2500 K), and equivalence ratios (0.1–4.0). Therefore, it was decided to proceed with kinetic mechanism by

Kéromnès [57] to reproduce the explosion limits in an organized, identifiable manner for the researchers in the field of HICE development.

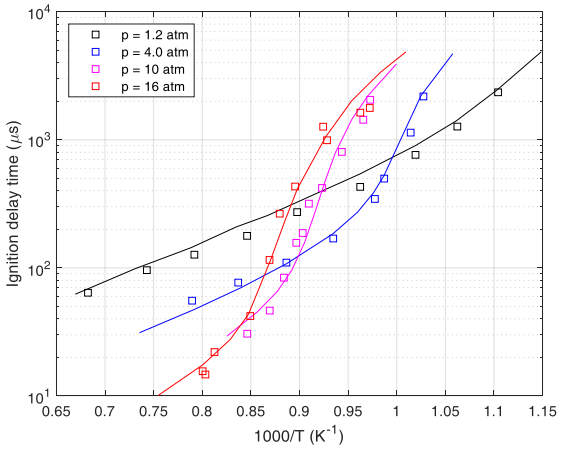

Figure 2-2 Performance of Kéromnès kinetic mechanism [57] against shock tube experiments [54] at $\phi = 1$ and pressures equal to 1.2, 4.0, 10 and 16 atm. Square markers represent experimental data and solid lines represent numerical simulations.

To perform the analyses proposed in the present work using the mechanism by Kéromnès 2013, explosion limits obtained from 0-D closed homogenous batch reactor simulations in Ansys CHEMKIN Pro code [55] were compared with those reported in reference simulation results available in the literature. Liang et al [58] validated the same mechanism against the results obtained from the eigenvalue analysis for the Z-shape explosion limits of $H_2/O_2/CO$ mixture [56]. The same setup used in [58] was selected to perform this analysis, in which a simulation duration of 1 *second* and a mixture composed of fuel (99% H_2 + 1% CO) and oxidant (100% O_2) were considered. The comparison is reported in Figure 2-3. A very good agreement is obtained from the intermediate- to high-pressure regime, which is the one of interest for the present work.

Although not essential for the purpose of this investigation, it is worth mentioning that for obtaining accurate results in the low-pressure regime it is required to model the radical species' depletion process occurring at the wall surfaces. In fact, in a 0-D simulation, the interaction with a material boundary is not directly modelled and, thus a comparison with experimental data in the literature necessitates the inclusion of the radical depletion aspect that affects the reactivity and hence the coordinates of the explosion limits. This behaviour can be taken into account by the introduction of additional reactions enclosing the so-called "sticking coefficients", with the aim of emulating the sticking process of radical species on the walls and the way it affects the rest of the reactions occurring at that specific temperature and pressure. These coefficients represent the pre-

exponential factor in the related modified Arrhenius equation i.e., $k = AT^b e^{-E_a/(RT)}$ [59], [60]. As shown in Figure 2-3(a), without implementing sticking coefficients to adhesion reactions between surface material (KCl) and radical species, the mechanism would not perform in the same way shown in [58]. As found in previous studies [56], termination of radicals at wall has a strong effect on the low-pressure explosion limits. To accommodate the effect of surface kinetics, sticking coefficients for radicals H_2O_2, HO_2, H, OH, O were set as 3e-4 for H_2O_2, 3e-3 for HO_2 and 8e-3 for H, OH and O. According to the values reported in [51], [56], the results obtained, after the implementation of these additional surface reactions, are shown in Figure 2-3(b) which appears to be consistent with that of [58]. This aspect was investigated to highlight that the observed discrepancies in the low-pressure regime can be entirely attributable to surface-interaction processes and are not due to numerical difficulties of the mechanism in calculating the gas-phase chemistry.

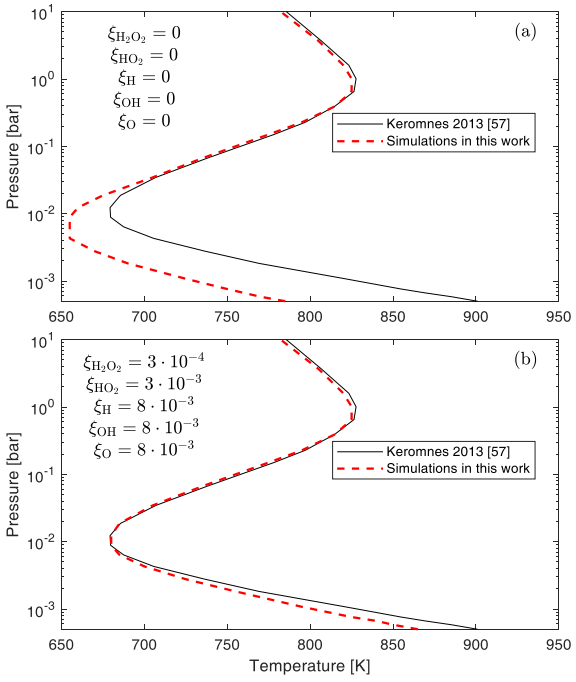

Figure 2-3 Mechanism validation with sticking coefficients (a) disabled (b) enabled. With sticking coefficients enabled, the simulations in this work match those with that in literature [58] simulated with the Kéromnès mechanism [57].

2.3 Development of a H_2 reactivity map for engine applications

As a first step of the proposed analysis, a wide database of thermodynamic states and corresponding ignition delay times was developed for H_2-air mixtures through numerical simulations employing the selected mechanism. From these data it was possible to highlight H_2 explosion limits' dependencies upon pressure, temperature, and equivalence ratio. Furthermore, the created database was also used to extract possible τ_{ID} values at the thermodynamic conditions achievable during a compression stroke of an ICE. Such values were employed in the assessment of possible critical conditions for auto-ignition, performed in the subsequent parts of the present work.

2.3.1 Numerical simulations setup

The simulations were performed using a 0-D closed homogenous batch reactor model in Ansys CHEMKIN Pro code [55]. The closed homogeneous batch reactor model was employed for solving the time-dependent balance equations for the total mass, gas-phase species, and energy. Table 2-1 shows the range of p, T and ϕ that the simulation data set occupies. The discretization of the grid was at $\Delta T = 1\ K$ for the entire temperature range, $\Delta p = 1\ bar$ between 1 and 30 $bars$ and then $\Delta p = 10\ bar$ between 30 and 100 $bars$, and $\phi = 0.1, 0.2, 0.5$ and 1. The ignition delay time is calculated by the temperature inflection point method i.e., between start of simulation and the time where the temperature profile reaches the maximum slope. The explosion limit on the pressure-temperature ($p - T$) plot was numerically simulated without including any effects of heat loss since for that to be accounted for, the experimental trace for pressure is needed [53] and in any case, it is a facility dependent term and hence a variable. Therefore, to be a consistent benchmark, it was justified to continue with 0-D simulations with a constant volume, adiabatic and complete combustion assumption. The constant volume assumption used in 0-D simulations can be justified through the purpose of achieving thermodynamic equilibrium of the charge's state based on a quasi-steady transformation during each spatial instant of the piston's movement. Despite the constant volume assumption for the calculation of ignition delay times (τ_{ID}) for individual thermodynamic states, the integral criterion (Section 3.3) takes into consideration the cumulative heat release associated to τ_{ID} that have been calculated with a constant-volume assumption and therefore, quantitively, combines the individual thermodynamic states as the piston is displaced.

The simulations duration in the present work was kept equal to 1 $second$, namely, for each pressure and temperature combination, a wait time equal to 1 $second$ was applied to record any ignition of the mixture within this period.

Table 2-1 Ranges of interest for pressure, temperature, and equivalence ratio in the present work along with the p, T discretization applied.

Pressure range	$1\ bar \leq p \leq 100\ bar$
Temperature range	$750\ K \leq T \leq 1600\ K$
Equivalence ratio range	$0.1 \leq \phi \leq 1$
Temperature discretization	$\Delta T = 1\ K\ \forall\ T$
Pressure discretization	$\Delta p = 1\ bar\ \forall\ p \leq 30\ bar$
	$\Delta p = 10\ bar\ \forall\ p > 30\ bar$

2.3.2 Results

As an example, representative of the obtained results, Figure 2-4 illustrates various isometric ignition delay time (iso-τ_{ID}) contours from a time of 1 s to 1 ms at (a) $\phi = 1$ (b) $\phi = 0.5$ and (c) $\phi = 0.1$. All the data obtained from these simulations were used to develop a reactivity map from which the τ_{ID} value can be extracted for any arbitrary (p, T, ϕ) set within the limits of the sample data. To identify the thermodynamic states for autoignition, the explosion limit of H_2-air for a constant and very short ignition delay of 1 ms has been chosen as the threshold. An extended representation of the 3rd explosion limit obtained in a (p, T, ϕ) space through iso-τ_{ID} curves of 1 ms is visualized in Figure 2-5 for $0.1 \leq \phi \leq 1$. Such a surface separates the explosive region from the non-explosive one and highlights the dependency of this explosion limit upon the main variables of interest.

It is possible to observe that a leaner mixture reduces the reactivity which is reflected by a shift of the iso-τ_{ID} curve towards the right of the reference iso-τ_{ID} curve at $\phi = 1$ (Figure 2-6(a)). On the contrary, the reactivity is increased as the mixture gets richer beyond $\phi = 1$ and shifts towards the left and hence, at a certain fixed pressure, the temperature required for auto-ignition is reduced. This increase in reactivity asymptotically slows downs around $\phi = 3$ where the following explosion limits at increasing ϕ start getting closer to the preceding one (Figure 2-6(a)). The only opposed difference is observed at very low pressures of 1 to 2 bar where the reactivity decreases as ϕ increases from stochiometric condition (Figure 2-6(b)). At such low pressures, the intermolecular interaction between H and O atoms decrease and the termination reactions overcome the rate of branching reactions [51] and hence the observed decrease in reactivity.

Figure 2-6 primarily provides a fundamental trend of the translation of the explosion limit as ϕ increases or decreases beyond stochiometric conditions. For DI HICEs where inhomogeneous ϕ values much higher than 1 are expected within the injected jet, a knowledge of the explosion limits for $\phi > 1$ can help identify any possibility of auto-ignition during the transient injection phase.

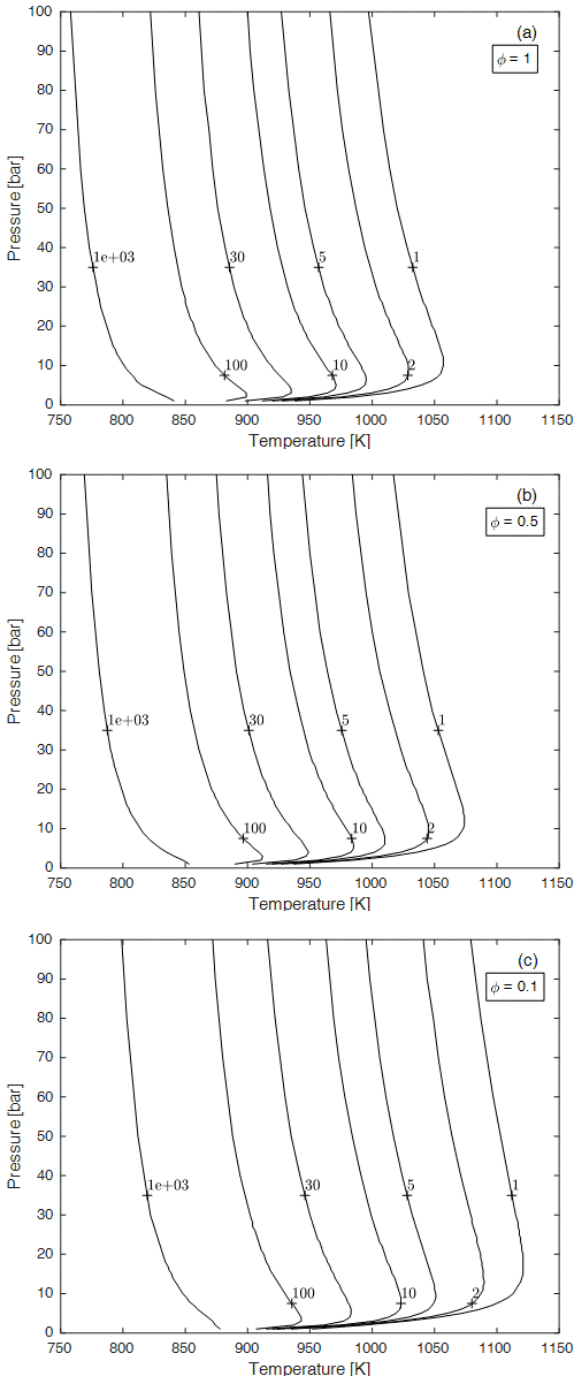

Figure 2-4 Isometric ignition delay time (iso-τ_{ID}) contours in milliseconds (ms), for H_2-air mixture, numerically simulated at (a) $\phi = 1$ (b) $\phi = 0.5$ and (c) $\phi = 0.1$.

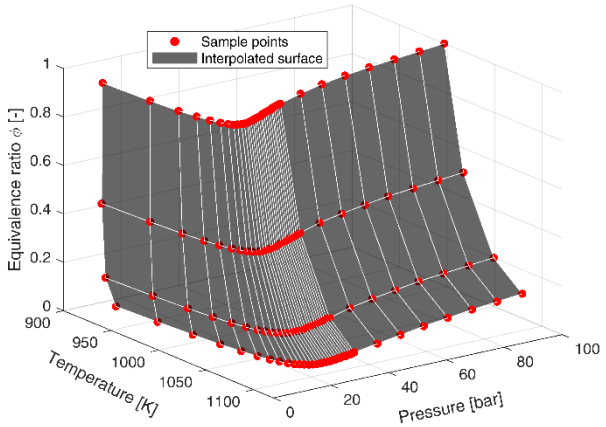

Figure 2-5 Interpolation surface for calculation of thermodynamic states (p, T) at the explosion limits ($\tau_{ID} = 1$ ms) between stochiometric ($\phi = 1$) and very lean ($\phi = 0.1$) H_2-air mixtures.

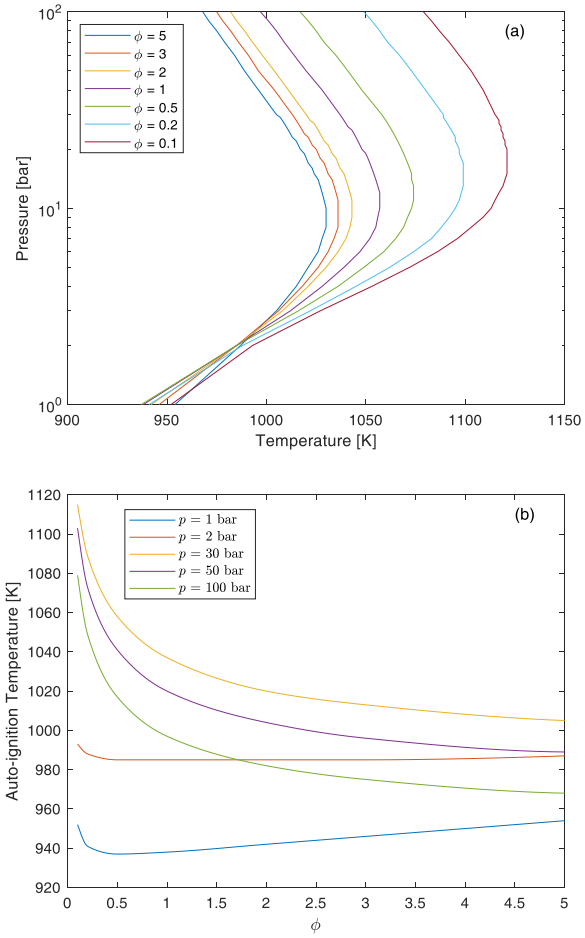

Figure 2-6 (a) Effect of ϕ variation on H_2-air explosion limit. (b) Effect on auto-ignition temperature at the explosion limit (τ_{ID} =1 ms) as the mixture moves from very lean ($\phi = 0.1$) to very rich conditions ($\phi = 5$).

3 Compression ratio selection criteria

This chapter provides three evolving criteria for the calculation of a safe maximum Geometrical compression ratio that doesn't induce auto-ignition at the given intake condition of pressure and temperature and homogenous mixture composition. The first criterion is a static one depending solely on the peak thermodynamic states achieved at the end of the compression stroke. The second criterion is a time-based one considering the displacement and speed of the piston as the charge is compressed. The third and final criterion is based on the integral and hence cumulative approach to consider heat release at each crank rotation as the mixture is compressed resulting in an earlier autoignition than the one calculated by the first static criterion.

3.1 Static criterion: engine operation limits based on motored in-cylinder p and T states

3.1.1 Evaluation of thermodynamic conditions during compression in ICEs

In order to assess if the engine operation can be considered safe or not, the thermodynamic state (p, T) of the charge, as it is compressed through the piston's displacement towards TDC, needs to be known at each instant of the crank's rotation θ. The state of the charge being known, the τ_{ID} is calculated using the iso-τ_{ID} reactivity map developed in the previous part of the work.

The simplest criterion employable for determining whether a GCR can be considered safe or not, can be based on the assessment of the mixture's explosive characteristics corresponding to motored in-cylinder pressure and temperature peaks. Under the hypothesis of the mixture to be an ideal gas having negligible friction within the fluid, and therefore assuming the compression stroke of the

engine to be isentropic, the compression curve, is obtainable by calculating the incremental pressure increase p_{2j} through incremental temperatures T_{2j}, where subscript "j" represents the increments, namely:

$$p_{2j} = p_i \cdot \left[\frac{T_{2j}}{T_i}\right]^{k/k-1} \tag{3-1}$$

The subscript "i" in p_i and T_i (Equation (3-1)) represents the thermodynamic state at the start of the compression at BDC ($\theta = -180°$) and will be termed as "intake" conditions from here onwards. A specific heat ratio $k = 1.4$ is chosen as that for air at STP. At a specified GCR and intake values of pressure p_i and temperature T_i, the TDC position on the compression curve can be visualized and its vicinity to a possible auto-ignition can be co-evaluated. The peak thermodynamic state at TDC ($\theta = 0$) can be calculated as:

$$p_2^{GCR}|_{\theta=0} = p_i \cdot (GCR)^k \tag{3-2}$$

$$T_2^{GCR}|_{\theta=0} = T_i \cdot (GCR)^{k-1} \tag{3-3}$$

3.1.2 Comparing in-cylinder conditions with H_2 explosion limits

According to this first criterion, the maximum GCR achievable without causing auto-ignition is defined as the one for which the pressure and temperature coordinate at TDC is the intersection point between the compression curve and the explosion limit, with the latter fixed at 1 ms. This choice is to find out the peak pressure and temperature values achievable without autoignition, provided that the system is adiabatic, and no external sources cause the peak p, T values to increase beyond what is expected in an isentropic compression.

Figure 3-1(a) shows safe and unsafe conditions simply by independent variations in p_i, T_i and GCR from a reference intake case of $p_i = 1\ bar$, $T_i = 300\ K$, $GCR = 20$. On the compression curve for this reference case, the TDC state at two different GCR values, namely $GCR = 20$ and $GCR = 25$, are indicated by a "blue square" (safe) and a "red cross" (unsafe) respectively. All GCR values corresponding to peak in-cylinder pressure and temperature values beyond the explosion limit (red cross symbols) pose an unsafe condition i.e., occurrence of autoignition. The curve with a higher intake pressure ($p_i = 1.25\ bar$) than the reference ($p_i = 1\ bar$) does not induce autoignition at TDC while maintaining the same $GCR = 20$, as that of the

reference case. However, the curve with a higher intake temperature ($T_i = 350\ K$) than the reference ($T_i = 300\ K$) shows that autoignition occurs well before the TDC, namely, at around 13.5 CAD bTDC (brown 'plus' markers) with the same $GCR = 20$. The 13.5 CAD bTDC is shown as an example piston position (at an engine speed of 1000 RPM) to represent the intersection point for the worst case ($p_i = 1\ bar, T_i = 350\ K$) in Figure 3-1(a) where the mixture state surpasses the explosion limit and evolves into an autoignition. The same piston position is also shown on the two other compression curves for the same GCR to help visualize their relative margin from autoignition. It should be noted by the reader that the calculation of the p and T values as a function of CAD, and hence engine speed, is described later in Section 3.2.

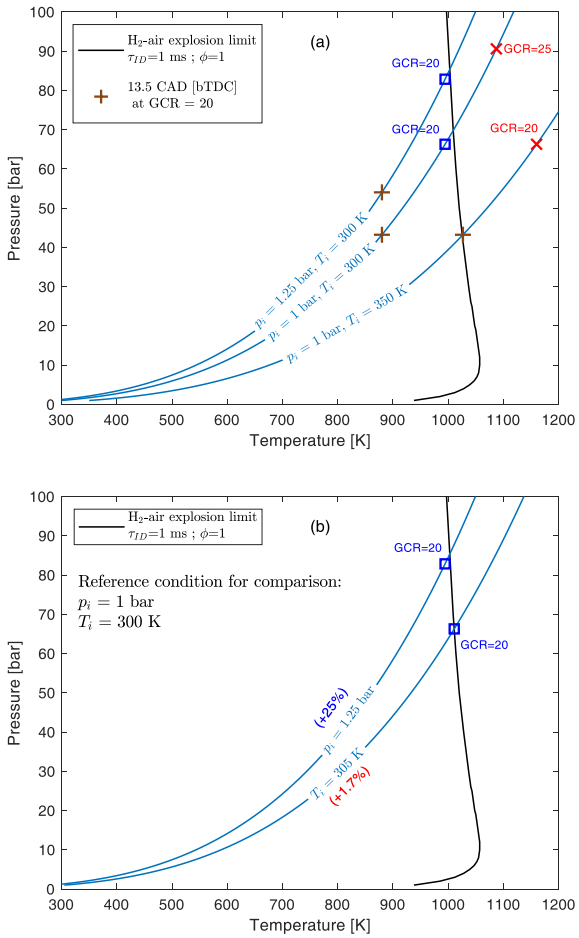

Figure 3-1 (a) Variation of GCR, p_i, and T_i on the $p-T$ plot. (b) Sensitivity analysis of autoignition occurrence through increase in intake pressure and temperature.

It must be pointed out that this is not a conservative approach to predict autoignition and therefore τ_{ID} values greater than 1 ms will be also considered in the subsequent parts of the present work, forming a broad range of peak p, T values. However, this first simple approach can be exploited to perform a

preliminary analysis about the influence of intake temperature and pressure on the probability to reach explosive conditions. Figure 3-1(b) demonstrates that the probability of autoignition is significantly more sensitive to an increase in T_i than p_i. Considering the reference curve and $GCR = 20$, even a 25% increase in p_i (1 bar to 1.25 bar) still presents a safe condition whereas a mere 1.7% increase in T_i (300 K to 305 K) renders the mixture to be just marginally safe. This is a meaningful result since a hot spot inside the combustion chamber with just a slightly higher local temperature than the rest of the charge can cause a premature ignition of the mixture. Extensive studies by Bradley [61], [62], [63] have demonstrated such transitions of the mixture state through hot spot temperature gradients.

The peak in-cylinder states evaluable through Equations (3-2) and (3-3) are only representative of ideal isentropic conditions without considering dynamic pressure effects or heat loss through the system. One way of simplifying these effects in a real engine is by using the Effective Compression Ratio (ECR) instead of GCR. A parameter named epsilon ε has been introduced in the present work to account for these effects by correcting the GCR value as follows:

$$ECR = \varepsilon \cdot GCR \tag{3-4}$$

Therefore, Equations (3-2) and (3-3), accordingly become:

$$p_2^{ECR}|_{\theta=0} = p_i \cdot (ECR)^k \tag{3-5}$$

$$T_2^{ECR}|_{\theta=0} = T_i \cdot (ECR)^{k-1} \tag{3-6}$$

Conditions that constitute ε may include charge inertial and dynamic effects due to inlet valve closing and heat exchange. The range of ε is defined from 0.7 to 1.1 representing the cases of low and high ECRs according to literature data [64]. Such a parameter can also enclose correction for the non-ideal behaviour of the gas during compression. Based on the concept of ε and analysis methods presented in this work, a clustered region of operating points i.e., probable thermodynamic conditions at TDC of a real engine, is drawn on the $p - T$ plot. This enclosed region is obtained by simultaneously plotting various compression curves represented by different intake conditions and then bounded by the TDC operating point values corresponding to the extreme range values of ε i.e., 0.7 and 1.1 which relate to $ECR = 0.7 \cdot GCR$ and $ECR = 1.1 \cdot GCR$, respectively.

In Figure 3-2, four different intake conditions with pressures from 1 to 1.5 bar and temperatures from 300 to 400 K are shown. The higher end of the intake conditions i.e., 1.5 bar and 400 K, utilized in the present work can be associated to

a non-intercooled turbocharged engine. The choice of these intake conditions is to show how such turbocharged conditions impact the vicinity of the in-cylinder charge's state to the explosion limit as the charge is compressed towards the TDC. A review study on HICEs [65] has presented previous experimental works with intake-air pressure-boosting applications up to $p_i = 2.6\ bars$. A maximum intake pressure of 1.5 $bars$ has also been reported by Lynch et al. [66]. The higher intake temperature of 400K is also justified through previous studies where pre-heating of intake-air for DI CI HICEs has been performed up to 120℃ [67]. Furthermore, such a high temperature can also be associated to any heat exchange between any residual gas that gets mixed with the fresh charge of the subsequent cycle. This is deliberately done to acquire higher temperatures for HCCI applications in HICEs as also presented by Aleiferis et al. [68]. This effect is a consequence of valve overlap and therefore scavenging of the in-cylinder mixture. Therefore, intake conditions expressed in the present work seem to be reasonably representative of real conditions in HICEs.

The TDC region is represented as a shaded area for three different values of $GCR = 9, 16$ and 26 in Figure 3-2 (a), (b) and (c), respectively. The operating points in this enclosed region that lie on the left of the explosion limit are considered safe while those on the right would induce auto-ignition of the charge mixture. Through this visual representation it can immediately be evaluated if the intake charge would end up in auto-ignition beginning from a specific intake condition. All the intake conditions end up in the safe zone at TDC for $GCR = 9$ (Figure 3-2(a)) even at the upper limit of $\varepsilon = 1.1$. However, for $GCR = 16$ (Figure 3-2(b)), an intake charge beginning with two out of the four initial conditions, namely ($p_i = 1\ bar$, $T_i = 400\ K$) and ($p_i = 1.5\ bar$, $T_i = 400\ K$), could auto-ignite in the TDC vicinity.

It is of paramount importance, however, to also have the option to check the autoignition probability well before the TDC, for instance, in the case of contamination by lubricating oil. A drastic change in the shape of the explosion limit and a shift towards the left in the presence of even a trace amount of lubricating oil (<1% by volume) significantly affects the pure H_2-air explosion limit and makes the charge explosive at a lower in-cylinder temperature, as it has been demonstrated by recent literature findings [37], [69]. Since lubricating oil is not considered in this section (and will be discussed in Chapter 4), and to emulate such an early autoignition, at least qualitatively at this point of the thesis, in Figure 3-2(c), at a very high $GCR = 26$, the autoignition occurs around 25 CAD bTDC for the two compression curves with intake conditions beginning with a higher temperature i.e., $T_i = 400\ K$.

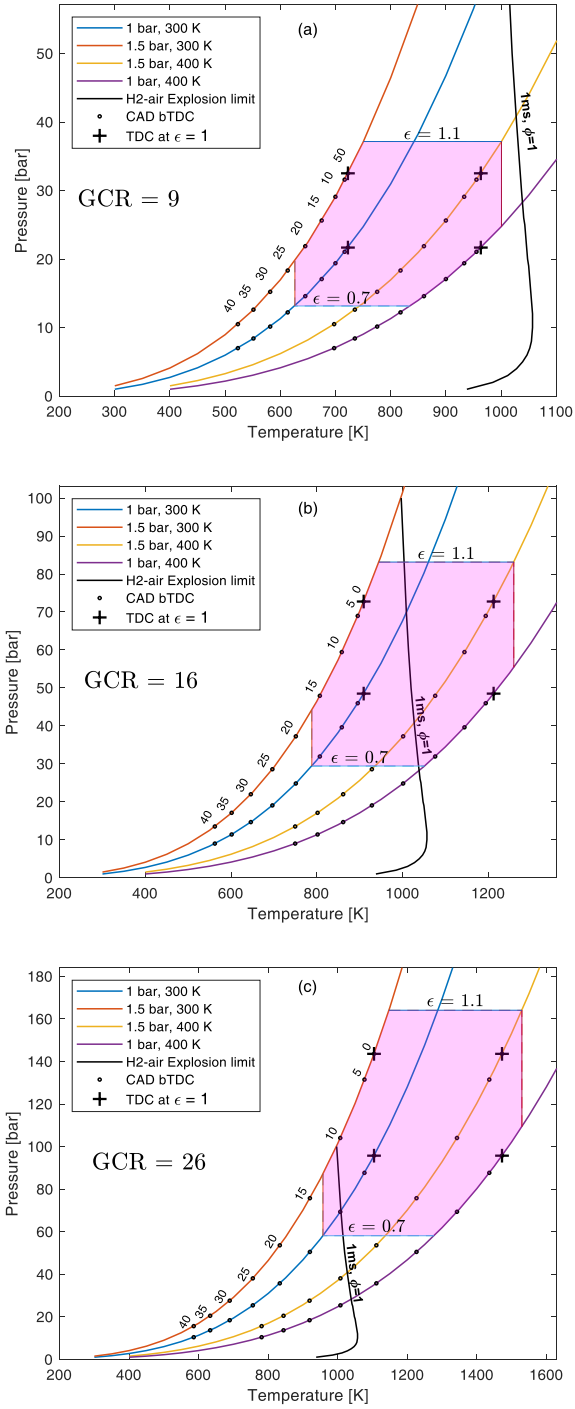

Figure 3-2 Combined compression plots for four intake states considered at (a) $GCR = 9$ (b) $GCR = 16$ (c) $GCR = 26$. The enclosed region in pink is bounded by the upper and lower limits of ε encapsulating all the possible TDC peak values in a real engine.

3.2 Time-based criteria for evaluating engine operation limits

A criterion based on motored in-cylinder peak pressure and temperature might not be sufficient at guaranteeing safe operating condition during the regular operation of an ICE, because the processes occurring inside an ICE are highly dynamic in nature. A continuous variation in load and engine speed is required according to the driver's input. This variation consequently affects the thermodynamic state of the charge mixture at any given instant and therefore the vicinity to the H_2-air explosion limit. Therefore, a static analysis cannot always ensure a HICE operation without a probability of auto-ignition. Therefore, a time-based (transient) approach monitoring a variable τ_{ID} is presented in this part of the work. For this purpose, at any instant along the stroke of the piston, the ignition delay time of the mixture needs to be calculated, along with the time remaining to reach the TDC, t_{TDC}, in order to evaluate the possibility of an autoignition event.

3.2.1 Evaluation of the τ_{ID} function

Having extensively characterized the explosion behaviour of H_2 across the 3rd explosion limit, it was possible to evaluate a function that correlates the instantaneous piston position during the compression stroke to the τ_{ID} values corresponding to the in-cylinder thermodynamic state at that same instant. The data set acquired through the iso-τ_{ID} map (Section 2.3.2) allows the τ_{ID} to be evaluated at any arbitrary thermodynamic state along the piston displacement, s. This is achieved by fitting an interpolation surface (shown in Figure 3-3 for $\phi = 1$, as an example) passing through all the known sample points on the said map.

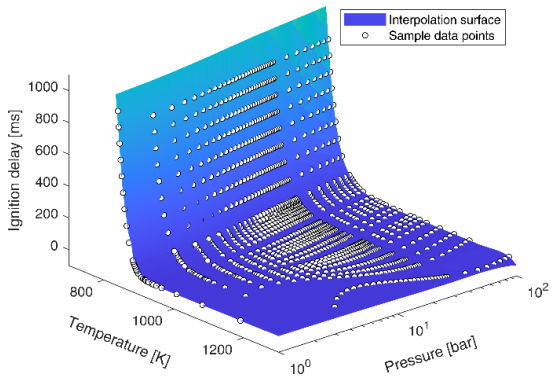

Figure 3-3 Interpolated surface for numerically simulated ignition delay times of H_2-air mixture at $\phi = 1$.

The underlying logical steps (Figure 3-4) to calculate τ_{ID} as a function of in-cylinder state (p, T, ϕ) requires knowledge of the pressure and temperature evolution during the compression stroke. Both states are calculated using isentropic relations, however, not using the GCR but an instantaneous Volume ratio namely, $VR(\theta)$, that is calculated using the instantaneous in-cylinder volume $V(\theta)$.

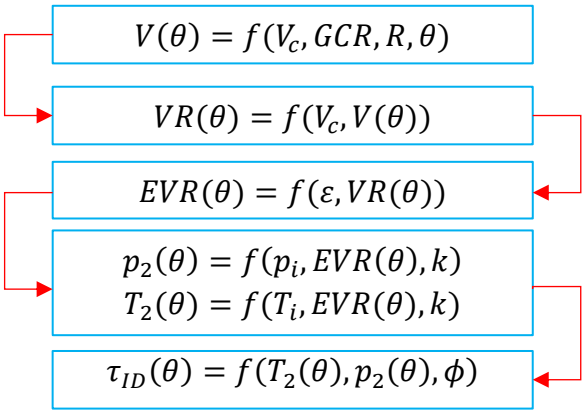

Figure 3-4 Calculation methodology for τ_{ID} as a function of engine crank rotation θ.

The instantaneous volume inside the cylinder $V(\theta)$ at each crank rotation (θ) is calculated [70] as:

$$V(\theta) = V_c \cdot \left\{1 + \frac{1}{2}(GCR - 1)\left[R + 1 - cos\theta - \sqrt{R^2 - sin^2\theta}\right]\right\} \quad (3\text{-}7)$$

$$V_c = \frac{V_d}{GCR - 1} \quad (3\text{-}8)$$

$$R = \frac{l}{a} \quad (3\text{-}9)$$

Where l is connecting rod length and a is the crank radius. The conventions used are $V(-180°) = V(BDC)$ and $V(0°) = V(TDC)$. From $V(\theta)$, the instantaneous Effective Volume Ratio $EVR(\theta)$ is calculated as:

$$VR(\theta) = \frac{V_1}{V_2} = \frac{V_d + V_c}{V(\theta)} \quad (3\text{-}10)$$

$$EVR(\theta) = \varepsilon \cdot VR(\theta) \quad (3\text{-}11)$$

The instantaneous in-cylinder pressure and temperature are calculated as:

$$p_2^{EVR}(\theta) = p_i \cdot (EVR(\theta))^k \quad (3\text{-}12)$$

$$T_2^{EVR}(\theta) = T_i \cdot (EVR(\theta))^{k-1} \quad (3\text{-}13)$$

The τ_{ID} corresponding to $p_2(\theta)$ and $T_2(\theta)$ values for a fixed ϕ are calculated through an interpolation function of the form $\tau_{ID} = f(T_2(\theta), p_2(\theta), \phi)$ acquired in MATLAB by employing the dataset of the iso-τ_{ID} map.

3.2.2 Evaluation of the time to TDC, t_{TDC}

The time remaining for the piston to reach the TDC (t_{TDC}) can be calculated as:

$$t_{TDC} = \frac{\theta_{bTDC}}{2\pi N/60} \tag{3-14}$$

where N is engine speed in Revolutions Per Minute (RPM). The t_{TDC} against τ_{ID} must be compared along the entire piston displacement. The piston moves very slowly at the stroke extremes (BDC/TDC), due to the acceleration and deceleration events and hence one can observe a non-linear behaviour for absolute piston position (s):

$$s = a \cdot cos\theta + (l^2 - a^2 \cdot sin^2\theta)^{1/2} \tag{3-15}$$

Table 3-1 Arbitrary engine geometry parameters used in the present work.

Bore	B	80 mm
Stroke	L	100 mm
Connecting rod length	l	137 mm
Crank Radius	a	50 mm (Half of stroke L)
Displacement volume	V_d	0.503 l
Clearance Volume	V_c	Variable (depends on GCR)

Equation (3-15) gives the piston position, s, as a function of θ and hence time t. Figure 3-5 shows the t_{TDC} plotted against normalized piston position, s^*, at a fixed engine speed of 1000 RPM where $s^* = 0$ corresponds to BDC and $s^* = 1$ to TDC.

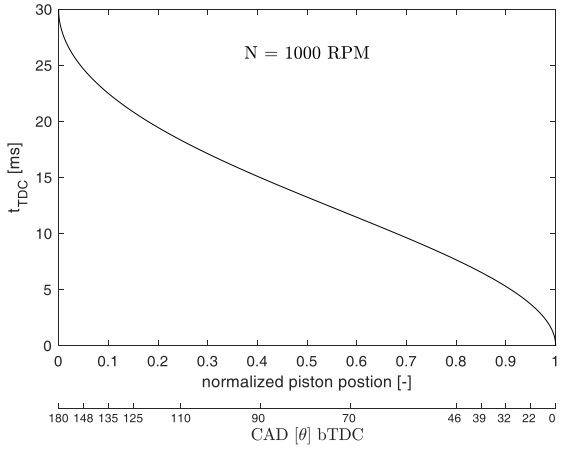

Figure 3-5 Time to reach TDC (t_{TDC}) vs normalized piston position (s^*) at 1000 RPM.

3.2.3 Tangency criterion: comparing τ_{ID} of the charge to the t_{TDC} at a specific CAD

The evolution of the in-cylinder pressure and temperature, as the piston compresses the charge towards the TDC, constitutes a transient passing of the charge's state through the iso-τ_{ID} explosion limits on a $p-T$ plot. This, essentially, means the variation of the τ_{ID} of the charge at every instant of the compression stroke. Theoretically, the charge is "safe" from auto-ignition if $t_{TDC} \leq \tau_{ID}$ along the entire compression stroke. This criterion will be referred to as the "tangency criterion" from here onwards. Figure 3-6 qualitatively demonstrates this criterion, differentiating between three example cases. The two τ_{ID} curves, one tangent (purple curve) and the other always higher than the t_{TDC} (blue curve), satisfy this criterion whereas the third τ_{ID} curve (red curve) intersects the t_{TDC} curve and therefore no more satisfies the criterion after the intersection point.

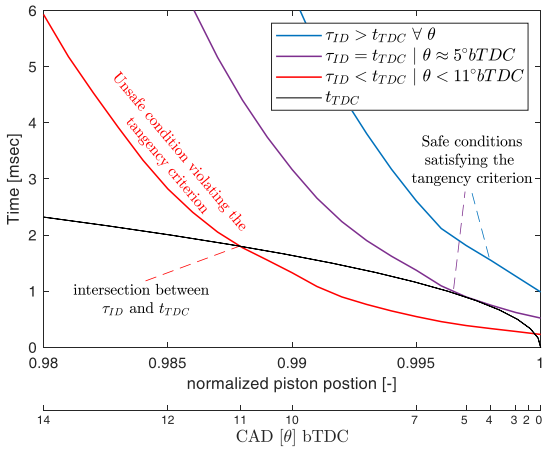

Figure 3-6 Qualitative representation of the "tangency criterion". The mixture is considered unsafe beyond the CAD where τ_{ID} gets lower than the t_{TDC} therefore declaring the charge mixture prone to autoignition.

The varying τ_{ID} is compared to the t_{TDC} curve in Figure 3-7 meanwhile verifying if the tangency criterion is satisfied. For an ideal engine with conditions considered in Figure 3-7, the traces of pressure (Figure 3-7(a)) and temperature (Figure 3-7(b)) evolution are generated utilizing the Equations (3-12) and (3-13), respectively, at both $\varepsilon = 0.7$ and $\varepsilon = 1.1$. With these traces as variables to the interpolant function for τ_{ID}, Figure 3-7(c) shows the resulting evolution of ignition delay times of the charge mixture. With a singular plot on time vs CAD (Figure 3-7(c)), both the t_{TDC} and τ_{ID} are compared. The vertical dotted line on the three plots marks the threshold CAD for marginal safety of the charge from auto-ignition at $\varepsilon = 1.1$. Just after this threshold, the tangency criterion is no longer satisfied, and the charge's

evolving state induces autoignition. However, the charge with identical intake conditions and GCR but for $\varepsilon = 0.7$ remains safe as the τ_{ID} curve at $\varepsilon = 0.7$ (blue curve) never intersects the t_{TDC} curve. Hence the tangency criterion remains satisfied unconditionally along the entire compression stroke.

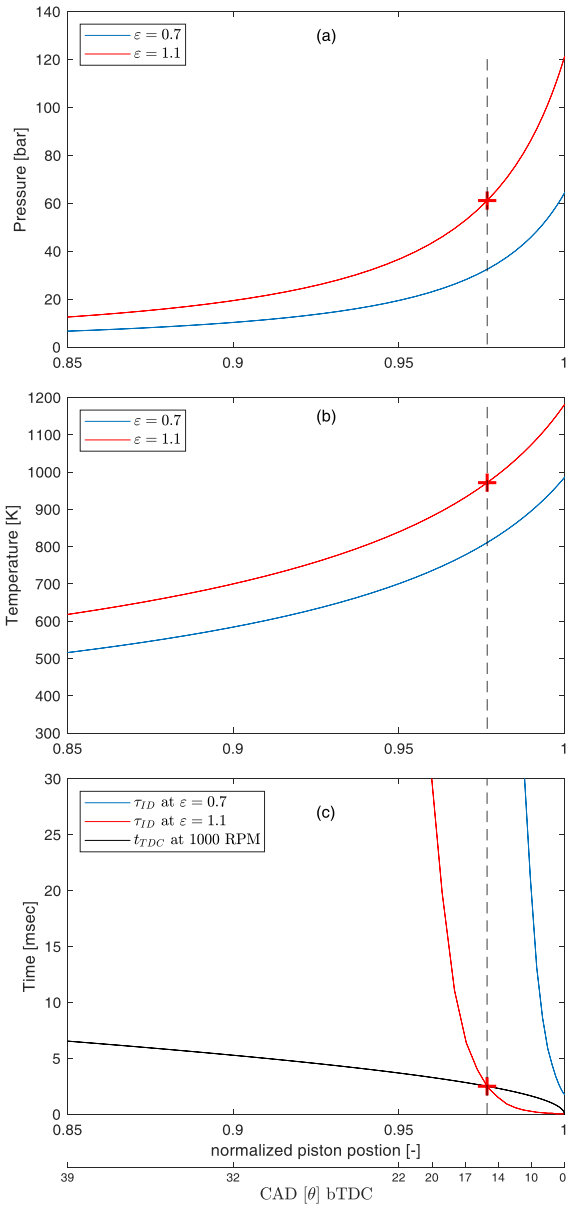

Figure 3-7 Pressure and temperature curves along piston displacement from BDC to TDC to evaluate corresponding ignition delay times. (a) Pressure trace (b) Temperature trace (c) t_{TDC} and τ_{ID} trace. $GCR = 28, p_i = 1\ bar, T_i = 300\ K, N = 1000\ RPM, \phi = 1$.

In Figure 3-6 and Figure 3-7, the supplementary x-axis for "CAD [θ] bTDC" also helps the reader to identify the non-linear progression of the piston compared to the crankshaft's rotation. This is important to know since the longer the piston dwells at the TDC the longer the charge has to evolve into a self-ignited combustion event, i.e., autoignition.

The above discussion follows below an example demonstrating how variations in the geometry (e.g., GCR) and intake thermodynamic state (e.g., T_i) affect the τ_{ID} curves shifting between unsafe and safe conditions i.e., verification of the tangency criterion, particularly in the vicinity of TDC. Starting from an arbitrary unsafe case at $GCR = 28$ (Figure 3-8(a)), a reduction of the GCR to 20 causes the rightward horizontal shifting of τ_{ID} curves now resulting in a new safe condition (Figure 3-8(b)), satisfying the tangency criterion at any piston position even at the upper limit of $\varepsilon = 1.1$. Furthermore, resuming from this new safe $GCR = 20$, if just the intake temperature of the charge is changed from $T_i = 300\ K$ to $T_i = 350\ K$ (Figure 3-8(c)), the red curve (corresponding to $\varepsilon = 1.1$) moves towards the left again and becomes no more tangent to the t_{TDC} curve and rather intersects it. Hence the GCR is further reduced until tangency is achieved again at $GCR = 14$ (Figure 3-8(d)).

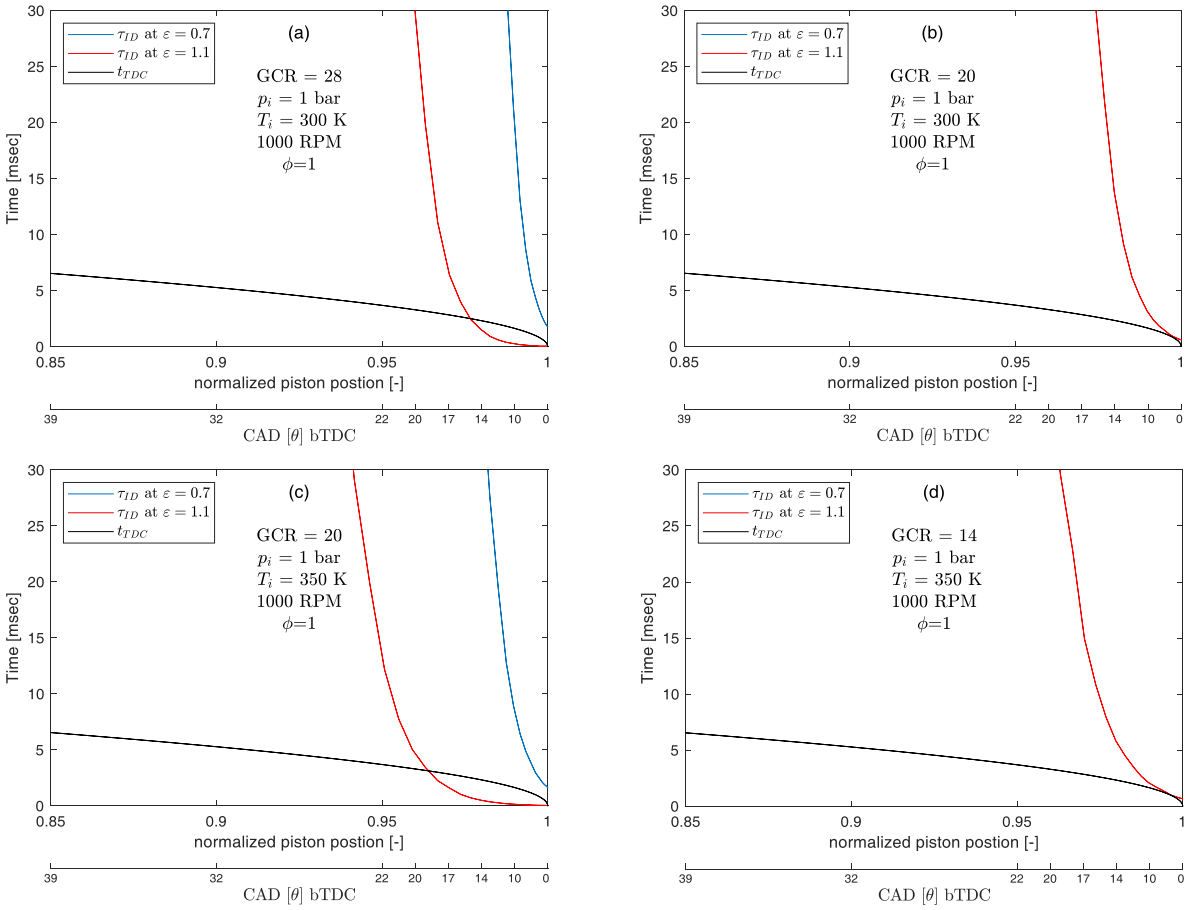

Figure 3-8 Transition from unsafe to safe conditions by varying GCR and intake temperature. (a) Arbitrary unsafe condition where τ_{ID} gets lower than t_{TDC} in the TDC vicinity for $\varepsilon = 1.1$. (b) Marginally safe condition satisfying the tangency criterion by reduction in GCR from 28 to 20. (c) Reinstating an unsafe condition by increasing the intake temperature T_i to 350 K. (d) Obtaining a safe condition again by further reduction in GCR to 14 while keeping $T_i = 350\ K$.

3.3 Integral based criterion: evaluating engine operation limits enclosing chemical heat release

The tangency criterion, although enclosing more details in comparison to the criterion based on a pure static analysis reported in Section 3.1, cannot completely guarantee an autoignition-free condition for the charge mixture. This is because the τ_{ID} is compared to t_{TDC} at each piston position without considering any chemical activity and the associated heat release at the previous stages. It must be noted that some heat is released before auto-ignition occurs. Thus, it is imperative to consider the cumulative chemical kinetics of the mixture as it is compressed inside the combustion chamber. This phenomenon was studied by Livengood and Wu [71] in which the concept of the rate of aggregate reaction is discussed to describe the relationship between ignition delay times and autoignition in homogenous mixtures. Their work emphasizes on the fact that for extremely small values of ignition delay (measured from the end of the compression process), an appreciable amount of reaction may occur during compression and thus the ideal concept of ignition delay is not strictly applicable.

This onset of autoignition through accumulation of τ_{ID} until it becomes comparable to the infinitesimal change in crank angle $d\theta$, therefore, needs to be calculated. To achieve an effective estimate of the CAD of autoignition, θ_{AI}, either before or after the TDC, the Livengood-Wu [71] integral, I, is utilized:

$$I = \int_0^t \frac{dt}{\tau_{ID}(T,p)} \tag{3-16}$$

The integral in Equation (3-16) is evaluated during mixture compression and any expansion in the engine during the time t, allowing for the changing value of $\tau_{ID}(T,p)$. The CAD at which this integral achieves a value equal to 1 corresponds to θ_{AI}. The left-hand side of Equation (3-16) is actually a ratio between concentration of pertinent reaction products to a critical concentration value considered in [71]. The database developed in the first part of the present work was used to evaluate this integral curve.

3.3.1 Numerical simulation setup

Based on Equation (3-16), it was observed that even though the charge mixture conditions for which the τ_{ID} values were always greater than t_{TDC} during the entire compression stroke, auto-ignition of the mixture still occurred because of the

integral, I, attaining a value of 1. To cross verify these conditions, 0-D real-gas compression simulations, with detailed chemistry, executed in Ansys CHEMKIN Pro, were performed to test, and validate the analytical estimations. As a prerequisite to these simulations, it was deemed necessary to understand the choice of ε for our analytical estimations that coincided with that of a real gas behaviour within the 0-D real-gas compression simulations. Based on the charge composition and thermodynamic state, the peak in-cylinder pressure and temperature values from the 0-D simulations were obtained for a motored cycle and an equivalent ε value was chosen, that corresponded to those peak values for our analytical isentropic calculations (Equations (3-5) and (3-6)). This value was found to be $\varepsilon = 0.85$. This value, within our earlier explained range of $0.7 \leq \varepsilon \leq 1.1$, is a consequence of a calibration with a 0-D simulation performed for a specific engine geometry (see Table 3-1). A value of $\varepsilon < 1$ is a result of the behaviour of the mixture as a real gas rather than ideal. Unlike the common industrial practice to vary the polytropic index to fit the peak p,T values, a strategy based on the variation of ε should represent a better choice. ε, defined in this work, is a scalar parameter independent of being linked to a specific mixture or engine. Therefore, changing the ε parameter seems to be an option more suitable in the design phase of the engine while keeping the specific heat ratio constant as $k = 1.4$ (isentropic).

3.3.2 Results

Three different cases of θ_{AI} estimation using Equation (3-16) have been explored in this section and whose results are reported in Figure 3-9.

Case 1 – Autoignition after TDC:
A primary arbitrary case with $p_i = 1\ bar$, $T_i = 410\ K$, $\phi = 0.5$, $GCR = 12$ and $N = 1000\ RPM$, the autoignition of the mixture is observed (Figure 3-9(a)). Even though the mixture has τ_{ID} values always greater than t_{TDC} during the entire compression stroke, it still auto-ignites at around $1\ CAD$ aTDC based on the Livengood-Wu integral. This condition might be considered a dangerous one for a SI engine because it could be representative of the occurrence of end-gas autoignition. To compare Equation (3-16) with the results from the 0-D simulations, the parameter of Net Heat Release Rate (NHRR) is chosen since it identifies the CAD where the maximum energy is released by the charge's autoignition. An enlarged view of the same conditions is represented in Figure 3-9(b) in which one can verify that the maximum slope of NHRR profile is achieved at almost the same CAD at which the integral I achieves a value of 1. In this case, the θ_{AI} evaluated using the integral and analytical calculations is 0.6995° while that

acquired at the maximum NHRR from 0-D simulation is 1.188°, resulting in an error of less than 0.5°. The start of the rising NHRR in Figure 3-9 (b) at around 8° $bTDC$ can be explained through the study of the reaction pathways that become dominant at the p and T values close to the TDC. Such a rise in NHRR is associated to the chain-branching explosion that ends up in a thermal explosion giving the maximum NHRR.

Case 2 – Autoignition before TDC:
A 10 K increase in the intake temperature i.e., $T_i = 420\,K$ (Figure 3-9(c)), while keeping the same conditions of case 1, causes an autoignition before the TDC at $\theta_{AI} = 3.5°\ bTDC$ calculated with Equation (3-16). The max NHRR from the 0-D simulation occurs at $\theta_{AI} = 2.76°\ bTDC$, resulting in an absolute error of less than 0.74°. Therefore, higher intake temperatures of the homogenous mixture or an equivalent presence of a hot spot provoking a temperature gradient within the charge can cause the charge to auto ignite before the TDC which in turn would cause an increase in the compression work, decreasing the net-work produced by the engine cycle.

Case 3 – No autoignition:
The final case is an example of decreased $T_i = 395\,K$ (Figure 3-9(d)) for which, ideally, the charge never self-ignites since I never approaches a value of unity and instead asymptotically attains constant value of about 0.8. Even the NHRR acquired from 0-D simulation is reduced by five orders of magnitude as compared to cases 1 and 2. The intake conditions for this case do not entail any heat release from chemical kinetics of the charge that is fast enough to be compared with the piston motion passing through the TDC i.e., $\tau_{ID} \gg dt$. At TDC ($\theta = 0°$) with $d\theta$ taken as 1°, $dt = 0.167\,ms$ and $\tau_{ID}|_{\theta=0°} = 4\,ms$ which gives a τ_{ID} that is about 24 times greater than dt taken by the piston to move 1 CAD.

To further broaden the results, over a span of intake pressures (1 to 2 bar) and temperatures (400 to 450 K), Figure 3-10 shows the θ_{AI} values compared between the analytical calculations in this work and those achieved from 0-D real-gas compression Ansys CHEMKIN simulations. The comparison shows a great deal of coherence between the two results with an absolute average error of 0.38° across the temperature range considered. Such a result allows the engine designer to use the analytical calculations, presented in this work, with confidence to estimate θ_{AI} and therefore construct the geometry as well as the plan an engine operating map (load vs engine speed) that ensures a safe performance for the HICE without the need to indulge in computationally expensive simulations, at least for the preliminary global design of the engine.

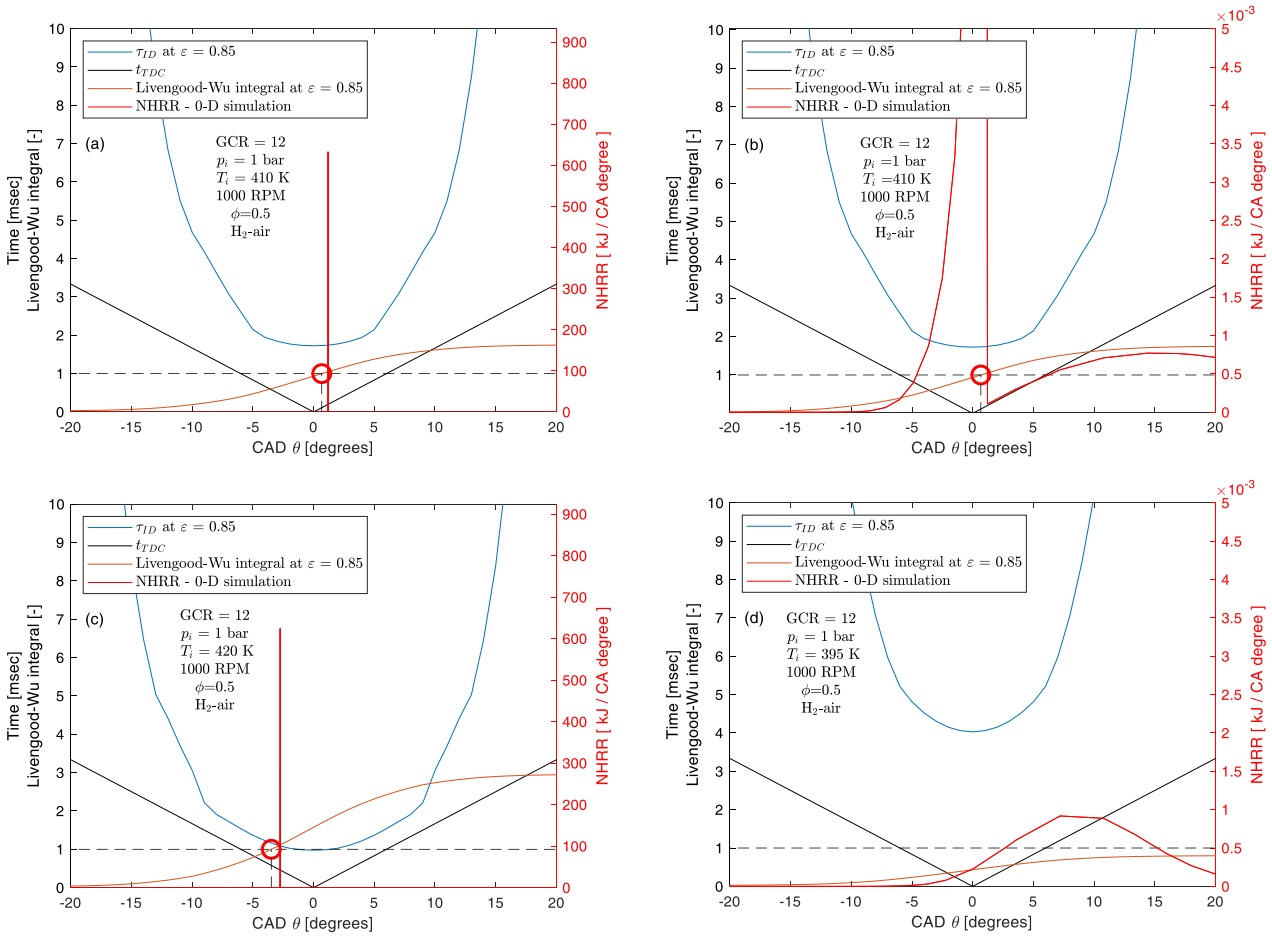

Figure 3-9 Estimation of Autoignition CAD using Livengood-Wu integral (a) Case 1: θ_{AI} after TDC (b) Enlarged view of Case 1 (c) Case 2: θ_{AI} before TDC (d) Case 3: No autoignition. For both Case 1 and Case 2, even though the tangency criterion estimates the mixture to be safe from autoignition, the integral criterion allows to calculate the possibility of autoignition utilizing the aspect of accumulated heat release during both the compression and expansion stroke.

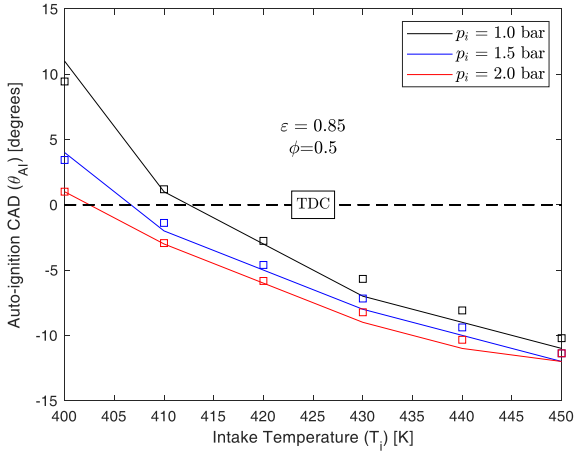

Figure 3-10 Comparison of Autoignition CAD θ_{AI} acquired by analytical calculation (present work) at $\varepsilon = 0.85$ (solid lines) and 0-D real-gas compression CHEMKIN simulations (square markers). Engine geometry used is that of Table 3-1.

The successful validation of the θ_{AI} for a single value of $\varepsilon = 0.85$ provides the necessary grounds to now calculate the range of θ_{AI} values for an entire epsilon range from 0.7 to 1.1. This ε range contributes, in effect, to the non-periodic nature of an ICE where in each cycle the operating conditions during the compression stroke may slightly vary, for instance due to a slight variation in engine speed causing a change in pressure evolution inside the intake ducts and causing a higher or lower ECR, therefore leading to a different θ_{AI} than the preceding cycle. The orange shaded region in Figure 3-11 illustrates this 'range' for the intake conditions considered. Instead of plotting the τ_{ID} curves just for a single $\varepsilon = 0.85$, two τ_{ID} curves, one each for the two extremes of ε i.e. 0.7 and 1.1 are plotted. The corresponding θ_{AI} values for the two cases are identified by the Livengood-Wu Integral (Equation (3-16)) attaining a value of 1 (red circles). Within this range could lie the infinite possibilities of the occurrence of an auto-ignition event in the case of a real engine.

A visual representation of the range of θ_{AI} values spanning over an intake temperature range between 350 K and 450 K, ε values of 0.7 and 1.1, and $\phi = 0.5$ is shown in Figure 3-12(a) for two intake pressures, namely, $p_i = 1\ bar$ (green area) and $p_i = 2\ bar$ (blue area). Figure 3-12(b) shows the θ_{AI} range for $p_i = 1.5\ bar$ while also indicating a map of isometric-epsilon (iso-ε) lines to conveniently find the appropriate θ_{AI} values for a specific ε.

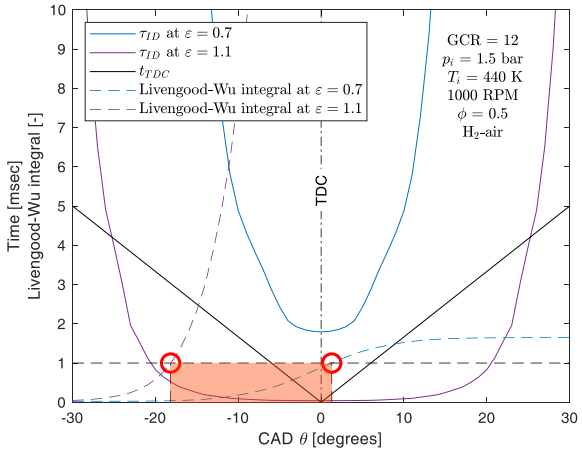

Figure 3-11 Range of possible θ_{AI} values for a charge mixture with ε between 0.7 and 1.1. The orange shaded region encapsulates all the possible values of θ_{AI} that maybe expected in a real engine for the engine parameters considered.

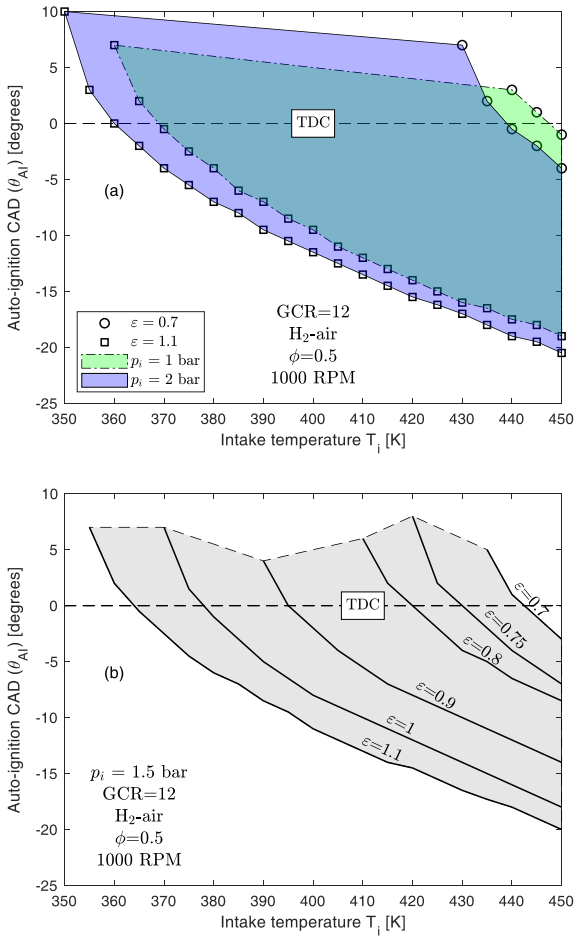

Figure 3-12 Auto-ignition CAD θ_{AI} across a range of intake temperatures for (a) $p_i = 1\ bar$ and $p_i = 2\ bar$ (b) $p_i = 1.5\ bar$ with iso-ε lines.

Explicitly, for SI HICEs, the integral criterion does not however quantify a direct parameter such as a "safe or optimized spark timing", therefore, quantitatively, it does not evaluate any possibility of knock due to end-gas autoignition. However, it does clearly identify, in a preliminary analysis, when to initiate the spark. The presented approach can provide an initial insight to both pre-ignition (before spark) and end-gas autoignition (post-spark). To avoid any pre-ignition, the energizing of the spark or more appropriately, the beginning of the flame propagation should take place before the maximum of the NHRR is reached due to evolving chemical reactivity as the charge is compressed. For instance, in Figure 3-9(b), for the conditions mentioned in the figure (and in a supposed case of a SI HICE), the spark should be ignited, at least, before the I achieves a value of 1. Figure 3-9(b) is for $\varepsilon = 0.85$ but the designer can be even more conservative and impose a higher value of ε up to a reasonable 1.1, as implemented in the present work, which will result in an earlier θ_{AI} and therefore the spark timing, in case of a SI engine, can be advanced further. Regarding end-gas autoignition, if, for instance, a simplified two-zone model is considered and the turbulent flame speed

is known, the θ_{AI} of the unburnt mixture being compressed towards TDC can still be calculated using I providing the engine designer a baseline to tweak the spark timing accordingly. Of course, this would require a modified equation for I to include the reduction of the unburnt volume as the flame propagates and the burned mass fraction increases.

3.4 Development of a correlation for evaluating engine operation limits

As a final objective of the present work, follows the development of a summarized form of an analytical expression that includes the effect of equivalence ratio ϕ and intake conditions (p_i, T_i) to evaluate, in a preliminary design phase, the safe GCR that is feasible for a HICE in real engine conditions.

The limit to the Maximum Safe GCR (MSGCR) is applied by observing the GCR value that initiates the first autoignition at a specified ϕ. The methods to find the MSGCR are those presented in Section 3.3, obtaining the first GCR that allows the Livengood-Wu integral to reach a value of 1. The precision to calculate MSGCR was set by imposing an increment of $\Delta GCR = 0.01$ while checking Equation (3-16).

Figure 3-13 shows the MSGCR limit at atmospheric intake conditions, $N = 1000\ RPM$ and $\varepsilon = 1$, i.e., $ECR = GCR$, for the entire range of equivalence ratios ϕ between 0.1 and 1. The comparison between MSGCR calculated on the basis of tangency criterion and that on the basis of the Livengood-Wu integral (Equation (3-16)) is also demonstrated suggesting the latter to be a more conservative approach and therefore more suitable to developing an analytical correlation for practical purposes.

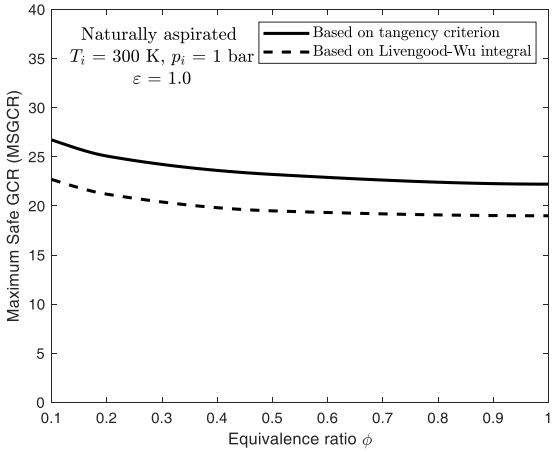

Figure 3-13 Maximum Safe GCR (MSGCR) limit for a naturally aspirated HICE at 1000 RPM and $\varepsilon = 1$ ($ECR = GCR$) for the intake conditions considered.

By analysing the trend of MSGCR as a function of equivalence ratio ϕ in Figure 3-13, a power law equation has been chosen to best suit and fit the data. The equation developed is validated for the ranges $1\ bar \leq p_i \leq 1.5\ bar$, $300\ K \leq T_i \leq 400\ K$, $0.1 \leq \phi \leq 1$ and $\varepsilon = 1$.

$$MSGCR = a \cdot \phi^b + c \tag{3-17}$$

where:

$$a = a(T_i) + a(p_i) = \left(32\, e^{-\frac{|d|}{200}T_i}\right) + (-0.4p_i + 0.6) \tag{3-18}$$

$$b = -0.28 \tag{3-19}$$

$$c = 128\, e^{-\frac{|d|}{200}T_i} \tag{3-20}$$

$$d = 1.425 \tag{3-21}$$

For ε value other than 1, Equation (3-17) needs to be divided by that ε value to get the correct MSGCR corresponding to a higher or lower ECR. Figure 3-14 shows the HICE operating region for two different but typical cases of intake conditions: (a) $p_i = 1\ bar$, $T_i = 300\ K$; and (b) $p_i = 1.5\ bar$, $T_i = 400\ K$.

These two cases, respectively, represent a HICE that is naturally aspirated at standard atmospheric conditions and one that is turbocharged but without any intercooling of the charge before entering the combustion chamber. The red cross-hatched region represents the range of operation when $\varepsilon = 1.1$ i.e., ECR is 1.1 times GCR. This region is upper bounded by the red curve and is the MSGCR limit avoiding auto-ignition. The blue curve for GCR limit ($\varepsilon = 0.7$) gives the possibility to achieve a higher MSGCR because of the lower ECR. The grey single-hatched region is rather a region of operation when the designer is sure of the ε value to be between 0.7 and 1.1 and can operate safely avoiding auto-ignition.

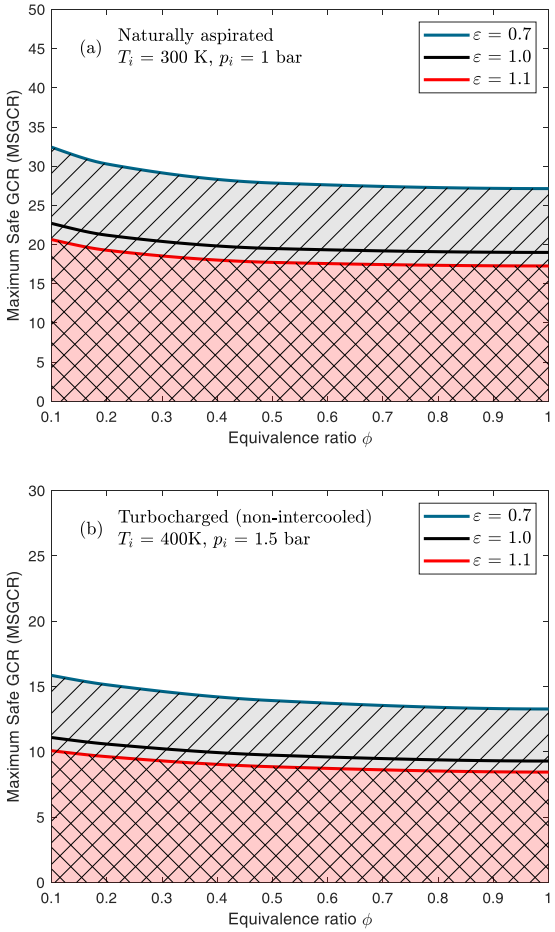

Figure 3-14 Optimal engine operation region for two different intake conditions (a) Naturally aspirated at STP (b) Turbocharged non-intercooled. The red cross-hatched region spans all the possible safe GCR values upper bounded by $\varepsilon = 1.1$ (red curve). The entire area under the MSCGR limit at $\varepsilon = 0.7$ (blue curve) provides all the safe GCR values that can be used without autoignition.

Figure 3-15(a) represents the goodness of fit at $\varepsilon = 1$ for our analytical expression spanning the whole range of initial conditions (p_i, T_i, ϕ) and Figure 3-15(b) shows the fit quality for $\phi = 1$ only.

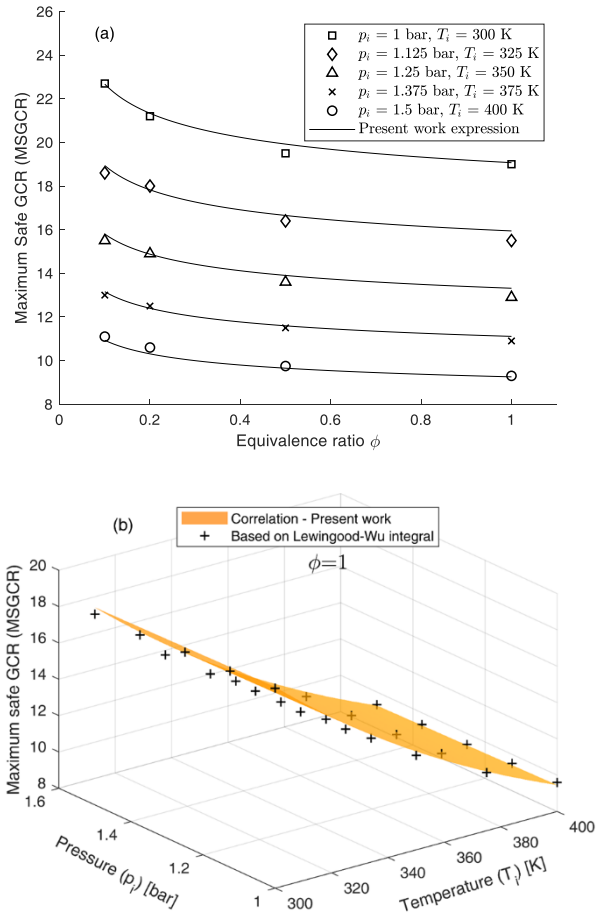

Figure 3-15 Goodness of fit - analytical expression (a) across entire ϕ range of interest (b) at stochiometric conditions ($\phi = 1$).

The second pressure-dependent term in Equation (3-18) well approximates the pressure variation at a constant temperature (Figure 3-16). Figure 3-16(a) at $T_i = 300\ K$ shows that the correlation is overestimating the MSGCR at both $p_i = 1\ bar$ and $p_i = 1.5\ bar$ whereas in Figure 3-16(b), the correlation is, in fact, underestimating the MSGCR. It is due to the fact that the coefficients b and d (Equations (3-19) and (3-21)) that control the shape and vertical position of the curve respectively are simplified such that a single constant value for both coefficients cover the entire range of the temperatures and pressures with minimal overestimation or underestimation at different intake conditions. The discrepancies might be reduced by using higher degree polynomial fits for coefficients b and d, but increasing the level of complexity of the proposed analytical expression. Thus, the proposed formulation can represent a good compromise. Furthermore, it is worth noting that the fact that the correlation underestimates the MSGCR at higher T_i, provides a stricter limit, in line with a more conservative approach that should be followed when safety considerations are involved. In fact, in such operating conditions, there is a higher probability to

quickly evolve into an auto-ignition than the case at the lower T_i. This justification can be associated to a higher sensitivity towards intake temperature in comparison to intake pressure as shown during the sensitivity analysis reported in Figure 3-1(b).

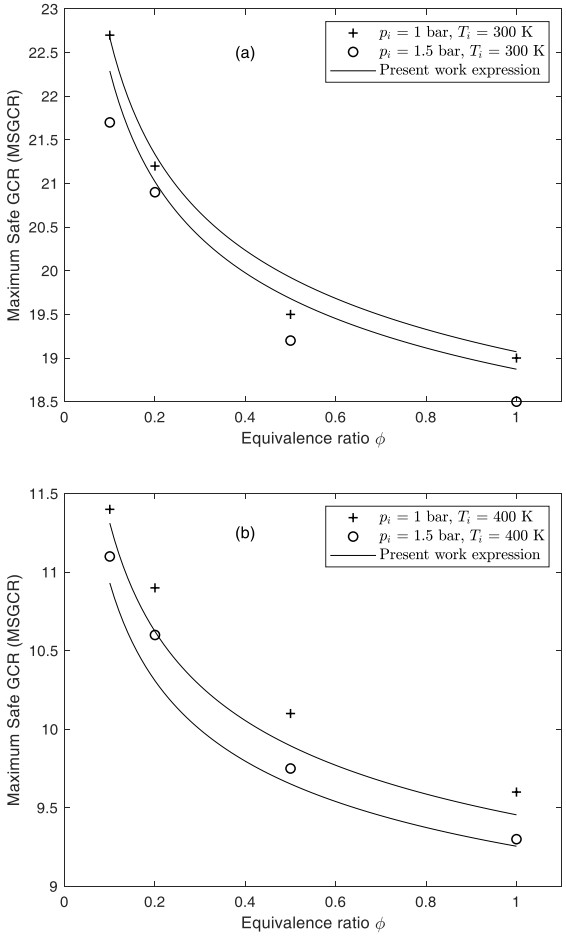

Figure 3-16 Estimation accuracy of Equation (3-17) to evaluate variation of intake pressure p_i at constant intake temperatures T_i .
(a) $T_i = 300\ K$ (b) $T_i = 400\ K$.

4 Lubricant oil – a source of undesired self-ignition

Hydrogen has regained attention in response to the urgent need of abandon fossil fuels due to the adverse impact that greenhouse gas emissions from the transportation sector are producing on the climate. The scientific research in the field of Internal Combustion Engines (ICEs) has continued to produce innovation in the last few decades for further developing this propulsion system. New combustion techniques [72], [73] and architectures [74], [75], [76] coupled with new strategies for controlling the combustion process [77], [78], [79] and more accurate and cost-effective sensors [80], [81], [82] have been proposed. However, in order to still consider ICEs a sustainable option for the future, the attention needs to be necessarily shifted on the fuels used for feeding the system [83], [84]. Hydrogen can give new possibilities of development to ICEs, by replacing fossil fuels in those applications in which the battery-based technologies are still not mature.

Although hydrogen is one of the most studied fuels, there exist criticalities that need to be addressed for rendering hydrogen ICEs ready for the marketplace [85], [86], [87]. Among these, there is the uncontrolled spontaneous premature ignition of the charge, which reduces the combustion control, limits the engine power output and forces the operation in very lean conditions in order to avoid potential engine failure [87], [88]. The onset of some abnormal combustion modes that arise even in the absence of any significant charge or temperature inhomogeneity might rely on the presence of lubricant oil contamination within the combustion chamber. Fundamental research showed that a relative short alkane molecule like n-heptane can increases the reactivity of H_2/air mixtures in the low-temperature range even by more than one order of magnitude [89]. Considering that the main components of base oils are normal alkanes having a number of carbon atoms ranging from 15 to 54 [90], lubricant oil results considerably more reactive than n-heptane ad might have more pronounced effects on the reactivity of H_2/air mixtures.

Evidence linking the presence of lubricant oil inside the combustion chamber to particularly severe detonation phenomena is already reported in the literature in the case of highly boosted gasoline engines, especially at low speeds and high loads [91], [92]. Lubricant oil significantly accelerates gasoline ignition [93], [94], and, in the case of hydrogen, the effects might be even more relevant, bearing in mind the larger difference in the molecular structure existing between hydrogen and lubricant oil, in comparison to that existing between gasoline and lubricant oil. Recent works on hydrogen ICEs have started to link the onset of abnormal combustions to the presence of "sensitive spots" whose generation has been ascribed to lubricant oil contamination [88], [95], [96].

It is worth to mention that there is also a secondary pathway by which lubricant oil can interfere with the regular evolution of the combustion process. Lubricant oil can represent a significant source of nano-sized soot particles, as observed in recent experiments [97], [98], [99], [100], since the formation of soot precursor species is facilitated in the case of the long-chain hydrocarbons constituting lubricant oil [42], [101]. When carbonaceous deposits are formed, these can serve as additional sensitive spots, able to initiate an uncontrolled ignition of the charge [92].

Understanding the reaction pathways involved in the oxidation of lubricant oil and its interaction with hydrogen could play a crucial role in the development of efficient and reliable hydrogen ICEs. Some useful information can already be inferred from previous research even though mainly oriented to gasoline engines [102], [103], [104], [105], [106], [107], [108]. Namely, a common approach consists in the use of a single n-alkane molecule, i.e., n-hexadecane (n-$C_{16}H_{34}$), as a surrogate species for emulating lubricant oil chemical characteristics [104], [105], [106], [108].

On the basis of this same hypothesis, a reaction mechanism was developed in a recent previous work [109] for studying the reactivity behaviour of H_2/n-$C_{16}H_{34}/air$ mixtures in what can be considered the first attempt to characterize the effects induced by the interaction of hydrogen with lubricant oil. It was found that lubricant oil can significantly increase the charge reactivity, especially in the low-temperature range. The results showed that lubricant oil surrogate species remains highly more reactive than H_2 for a wide range of temperatures, as it can be observed in Figure 4-1, which is reported as an example for the reader's convenience (observe the existence of regions 2 and 3). This result pointed out that the presence of lubricant oil can facilitate the mixture ignition at temperatures considerably lower than those at which hydrogen usually auto-ignites (at a given pressure). In [109] several H_2/n-$C_{16}H_{34}/air$ mixtures having different compositions were analysed as well, highlighting that very small amounts

of lubricant oil are sufficient to promote the auto-ignition of the charge. However, those analyses did not provide information about the effective amounts of lubricant oil that can be found where oil contamination occurs, namely in the vicinity of oil droplets.

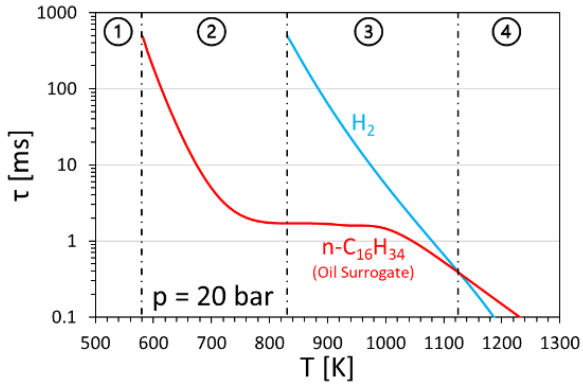

Figure 4-1. Results obtained in [109] regarding the ignition behaviour of $n\text{-}C_{16}H_{34}/air$ and H_2/air mixtures at a pressure of 20 bar and an equivalence ratio of 0.5.

The aim of the present work is to find out if a lubricant oil droplet suspended in a H_2/air environment can effectively represent a sensitive spot from which a chemical process can start and propagate throughout the charge. To this purpose, a relatively simple analytical model is developed to derive reasonable profiles of the temperature and the mass fraction around the droplet. The results were used to initialize zero-dimensional numerical simulations performed in the OpenSMOKE++ framework. n-hexadecane was selected as a surrogate chemical species to model the chemical and physical behaviour of lubricant oil and the reduced chemical model, developed in [109] was employed in the simulations for emulating the reactivity properties of $H_2/oil/air$ mixtures. With this approach it was possible to study the charge reactivity variations induced by the presence of oil vapour in the vicinity of an oil droplet, providing quantitative information with small computational efforts.

4.1 Analytical model

Modelling the vaporization of a liquid oil droplet in an environment consisting of hydrogen and air is not a trivial task. The mathematical description of the heat and mass transfer processes involves complex partial differential equations that are usually solved through numerical integration techniques, when a detailed description of the related physical processes is required. However, the present

work does not aim at providing a comprehensive description of the evaporating behaviour of an oil droplet, but, more practically, it is rather focused on the attempt of highlighting the potential threat to the regular engine operation constituted by the $H_2/oil/air$ gaseous mixture that forms around an oil droplet.

The present analytical model was conceived with the aim of obtaining expressions for the temperature and species distributions in the region close to the droplet surface, with a limited computation effort, but which result physically reasonable, so that they could be used to initialize reactive 0D numerical simulations. With this approach it was possible to assess the spatial variation of the mixture ignition delay time, induced by the oil droplet without the need of performing complex and time demanding CFD simulations. Despite its simplicity, this analytical model gives useful information that, coupled with chemical analyses, can provide useful insight in the problem.

4.1.1 Model description

As depicted in Figure 4-2, the model considers a single droplet existing in a quiescent, infinite medium constituted by a H_2/air mixture and in which a temperature higher than that of the droplet reigns. A spherically symmetric coordinate system was employed for describing the problem, in which the radius, r, is the only coordinate variable and has its origin at the centre of the droplet. The variables at the liquid-vapor interface are denoted with the subscript "s". Energy necessary to vaporize the liquid is transferred, in the form of heat, from the surrounding ambient to the droplet, and, simultaneously, the oil vapor diffuses from the droplet surface into the ambient gas. The interactions with any other droplets, and the effects of convection are ignored. Radiation heat transfer is considered negligible. The pressure is considered uniform and constant. The lubricant oil droplet is a single-component liquid, with zero solubility for gases and having the n-hexadecane properties. The evaporation process is considered to be much slower than the involved chemistry, so that, a quasi-steady assumption is used to describe the process. The thermodynamic parameters, such as the gas-phase thermal conductivity, λ, and specific heat, $c_{p,g}$, as well as the product of the density and mass diffusivity, $\rho\mathcal{D}$, are all considered constants. The hypothesis of unit Lewis number, $Le = \lambda\,/(c_{p,g}\rho\mathcal{D})$, is invoked.

With the above assumptions, the oil (n-hexadecane) mass fraction distribution $Y_{oil}(r)$ and the temperature distribution $T(r)$ in the gaseous ambient surrounding the droplet can be found by solving the gas-phase mass, species and energy conservation equations, the droplet gas-phase interface energy balance, and the droplet liquid mass conservation equation.

From the gas-phase mass conservation, with the assumption of quasi-steady vaporization, it can be stated that the mass flowrate, $\dot{m}$, is a constant, independent of the radius, thus:

$$\dot{m} = 4\pi r^2 \rho v = 4\pi r^2 \rho_s v_s = const\,, \tag{4-1}$$

where v is the velocity of the flow leaving the droplet surface.

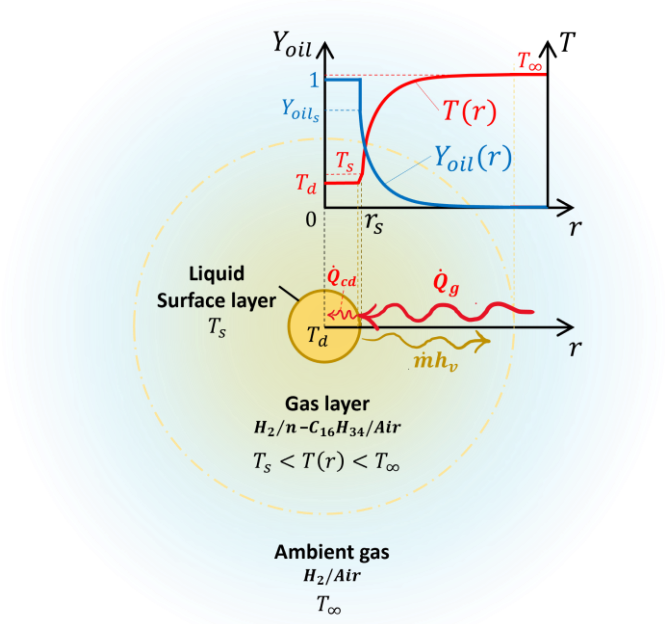

Figure 4-2. Schematization of the evaporation process according to the "onion skin" model, enclosing energy fluxes at the surface and the expected mass fraction, $Y_{oil}(r)$, and Temperature, $T(r)$, distributions.

It is possible to obtain an expression describing how the n-hexadecane concentration varies moving away from the droplet surface by solving the steady species conservation equation, which can be written as

$$\frac{d}{dr}(4\pi r^2 \rho v Y_{oil}) = \frac{d}{dr}\left(4\pi r^2 \rho \mathcal{D} \frac{dY_{oil}}{dr}\right). \tag{4-2}$$

For the vaporizing droplet, the total mass flow rate leaving the droplet surface must be equal to the sum of the mass flow rates due to the bulk convective motion of gaseous mixture at the surface and the mass diffusion rate of the vapour in the radial direction due to the existence of a concentration gradient around the droplet surface. Considering that the total flowrate is everywhere identical to the oil vapour flowrate, the condition to which the species conservation equation must be constrained can be expressed as

$$\rho_s v_s = \left[\rho v Y_{oil} - \rho \mathcal{D} \frac{dY_{oil}}{dr}\right]_s . \tag{4-3}$$

Equation (4-2) can be integrated two times with respect to r, by imposing the condition expressed by Equation (4-3) and that $Y_{oil} = Y_{oil_s}$ at the surface (where $r = r_s$), After some algebra, it is possible to find the expression that describe the n-hexadecane concentration variation along the radial coordinate, viz.,

$$Y_{oil}(r) = 1 - \frac{\left(1 - Y_{oil_s}\right) e^{-\frac{Z\dot{m}}{r}}}{e^{-\frac{Z\dot{m}}{r_s}}}, \tag{4-4}$$

where $Z = \frac{1}{4\pi\mathcal{D}\rho}$. The unity Lewis number assumption implies that $\frac{\lambda}{c_{pg}} = \rho\mathcal{D}$, thus the parameter Z can be also expressed as $Z = \frac{c_{p,g}}{4\pi\lambda}$.

The temperature distribution in the gas phase can be obtained as a solution of the gas-phase energy conservation equation, which, with the $Le = 1$ assumption, reduces to the simple Shvab–Zel'dovič form

$$4\pi r^2 \rho v \frac{d\left(c_{p,g}T\right)}{dr} = \frac{d}{dr}\left[4\pi \frac{\lambda}{c_{p,g}} r^2 \frac{d\left(c_{p,g}T\right)}{dr}\right]. \tag{4-5}$$

Assuming that the gas-phase thermal conductivity, λ, and specific heat, $c_{p,g}$, are constant, Equation (4-5) can be integrated twice with respect to r, by imposing the boundary conditions far from the droplet surface, i.e., $T = T_\infty$ for $r \to \infty$, and at the droplet surfaces, i.e., $T = T_s$ for $r = r_s$, as illustrated in Figure 4-2. The temperature distribution in the gas phase can be then obtained:

$$T(r) = \frac{(T_\infty - T_s) e^{-\frac{Z\dot{m}}{r}} - T_\infty e^{-\frac{Z\dot{m}}{r_s}} + T_s}{1 - e^{-\frac{Z\dot{m}}{r_s}}}. \tag{4-6}$$

In order to evaluate the mass species and temperature distributions, it is necessary to calculate the evaporation rate, $\dot{m}$, by writing the energy balance at the droplet surface. Figure 4-2 schematizes the instantaneous energy fluxes at the surface of the evaporating droplet. The gas-phase ambient is at a higher temperature than the droplet, so that heat ($\dot{Q}_g$) is conducted through the gas phase and transferred to the droplet surface. This energy is that required to heat up the liquid ($\dot{Q}_{cd}$) and induce the oil vaporization ($\dot{m}\Delta_v h_{oil}$). Mathematically, this can be expressed as

$$\dot{Q}_g = \dot{m}\, \Delta_v h_{oil} + \dot{Q}_{cd}\,, \tag{4-7}$$

where $\Delta_v h_{oil}$ is the heat of vaporization of the oil. The instantaneous conduction heat transfer from the gas phase, $\dot{Q}_g$, can be evaluated by applying Fourier's law,

while the instantaneous heat conducted into the droplet interior, $\dot{Q}_{cd}$, can be easily evaluated by employing the so-called "onion-skin" model, which considers the droplet as consisting of an interior region existing uniformly at its initial temperature, T_d, and a thin liquid surface layer at the surface temperature, T_s. In this model, $\dot{Q}_{cd}$ in Equation (4-7) represents the thermal power required to heat the fuel from T_d to T_s. With these assumptions, Equation (4-7) can be rewritten as

$$\left[\lambda 4\pi r^2 \frac{dT}{dr}\right]_s = \dot{m}\left[\Delta_v h_{oil} + c_{p,l}(T_s - T_d)\right] \tag{4-8}$$

where $c_{p,l}$ is the specific heat of the liquid n-hexadecane, and the temperature gradient at the interface can be obtained from the temperature distribution in the gas layer around the droplet (Equation (4-6)). After some algebra it is possible to write an expression that links the evaporation mass flow rate, $\dot{m}$, to the droplet surface temperature, T_s, namely,

$$\dot{m} = \frac{r_s}{Z}\ln\left[1 + \frac{c_{p,g}(T_\infty - T_s)}{\Delta_v h_{oil} + c_{p,l}(T_s - T_d)}\right] = \frac{r_s}{Z}\ln[1 + B]\,, \tag{4-9}$$

where $B = \frac{c_{p,g}(T_\infty - T_s)}{\Delta_v h_{oil} + c_{p,l}(T_s - T_d)}$ represents the transfer number for this specific problem.

In addition to the evaporation rate, $\dot{m}$, Equations (4-4) and (4-6) require the knowledge of the n-hexadecane mass fraction and temperature values at the droplet surface, namely, Y_{oil_s} and T_s, respectively.

It is possible to evaluate the n-hexadecane concentration at the droplet surface as a function of the mass flow rate, $\dot{m}$, by imposing to Equation (4-4) the condition that $Y_{oil} = 0$ for $r \to \infty$, namely, no oil present in the H_2/air mixture far away from the droplet:

$$Y_{oil_s} = \frac{B}{B + 1}\,. \tag{4-10}$$

A relation between Y_{oil_s} and T_s that provide closure to the problem can be obtained by assuming equilibrium between the liquid and vapor phases at the droplet surface. Such an equilibrium can be described in a simple form by employing the Clausius–Clapeyron equation, which links the partial pressure of oil (n-hexadecane) vapor at the liquid-vapor interface, p_{oil_s}, at a given temperature, T_s, to the vapor pressure estimated in a known reference state, i.e.,

$$\frac{p_{oil_s}}{p_{oil_{s,ref}}} = e^{-\frac{\Delta_v h_{oil}}{R}\left(\frac{1}{T_s} - \frac{1}{T_{s,ref}}\right)}\,, \tag{4-11}$$

where, and $T_{s,ref}$ is the boiling temperature of lubricant oil (n-hexadecane) at the reference pressure $p_{oil_{s,ref}}$ (1 atm). The oil vapour partial pressure, p_{oil_s}, can be related to the oil mole fraction, χ_{oil_s}, and mass fraction, Y_{oil_s}, as follows:

$$Y_{oil_s} = \frac{p_{oil_s}}{p} \frac{MW_{oil}}{\chi_{oil_s} MW_{oil} + (1 - \chi_{oil_s}) MW_{\infty}}, \tag{4-12}$$

where MW_{oil} and MW_{∞} are the molecular mass of the oil (n-hexadecane) and the average molecular mass of the H_2/air mixture far from the droplet, respectively.

Substituting Equation (4-12) into Equation (4-11) yields an explicit relation between Y_{oil_s} and T_s, namely,

$$Y_{oil_s} = \frac{e^{-\frac{\Delta_v h_{oil}}{R}\left(\frac{1}{T_s} - \frac{1}{T_{s,ref}}\right)} MW_{oil}}{e^{-\frac{\Delta_v h_{oil}}{R}\left(\frac{1}{T_s} - \frac{1}{T_{s,ref}}\right)} MW_{oil} + \left[p - e^{-\frac{\Delta_v h_{oil}}{R}\left(\frac{1}{T_s} - \frac{1}{T_{s,ref}}\right)}\right] MW_{\infty}}. \tag{4-13}$$

Equations (4-9), (4-10) and (4-13) can be solved simultaneously in order to evaluate the conditions at the droplet surface, namely in order to obtain $\dot{m}$, Y_{oil_s} and T_s. These values can be used to evaluate the mass fraction distribution $Y(r)$ and the temperature distribution $T(r)$ in the gaseous ambient surrounding the droplet, using Equations (4-4) and (4-6), respectively.

4.1.2 Parameters estimation

In order to evaluate the derived equations, a proper selection of appropriate mean values for the liquid- and gas-phase thermodynamics properties of the involved species and mixtures was needed.

The specific heat of liquid n-hexadecane, $c_{p,l}$, was evaluated by means of the polynomial expression provided by Zhang et al. [110], at the temperature of the liquid droplet, T_d, namely,

$$c_{p,l} = c_{p,l}^{oil}(T_d) = a_1 + a_2 T_d + a_3 T_d^2 , \tag{4-14}$$

with the coefficients reported in Table 4-1.

For the gas-phase specific heat, $c_{p,g}$, and the thermal conductivity, λ, in the gas layer surrounding the droplet, the approach suggested by Law and Williams [111] was employed. i.e., the gas-phase specific heat, $c_{p,g}$, was approximated with that of oil vapours, namely, with that of gaseous n-hexadecane, $c_{p,g}^{oil}$, as

$$c_{p,g} = c_{p,g}^{oil}(\bar{T}) ; \tag{4-15}$$

while the gas-phase thermal conductivity value was evaluated as a weighted average with respect to the value of gaseous n-hexadecane, λ_g^{oil}, and that of the H_2/air mixture, λ_∞, [111] as

$$\lambda(\bar{T}) = 0.4\,\lambda_g^{oil}(\bar{T}) + 0.6\,\lambda_\infty(\bar{T})\,. \tag{4-16}$$

The characteristic temperature, $\bar{T}$, at which these parameters were evaluated, was estimated via the so-called "one-third rule" [112], namely,

$$\bar{T} = T_s + \frac{(T_\infty - T_s)}{3}. \tag{4-17}$$

The gas-phase specific heat value at $\bar{T}$ was evaluated by means of the following polynomial expression:

$$c_{p,g}^{oil}(\bar{T}) = \frac{R}{MW_{oil}}(a_1 + a_2\bar{T} + a_3\bar{T}^2 + a_4\bar{T}^3 + a_5\bar{T}^4)\,, \tag{4-18}$$

Table 4-1 Coefficients employed in the polynomial expressions for the specific het of liquid n-hexadecane, $c_{p,l}^{oil}(T_d)$ [113]; for the specific heat, $c_{p,g}^{oil}(\bar{T})$ [109] and thermal conductivity, $\lambda_g^{oil}(\bar{T})$ [114] of gaseous n-hexadecane.

	a_1	a_2	a_3	a_4	a_5	a_6	a_7	a_8
$c_{p,l}^{oil}$	$[J/(Kg\,K)]$	$[J/(Kg\,K^2)]$	$[J/(Kg\,K^3)]$					
	1720.2	-0.53	$6\cdot10^{-3}$					
$c_{p,g}^{oil}$	$[-]$	$[1/K]$	$[1/K^2]$	$[1/K^3]$	$[1/K^4]$			
	$-3.64\cdot10^{0}$	$0.196\cdot10^{0}$	$-1.27\cdot10^{-4}$	$4.14\cdot10^{-8}$	$-5.41\cdot10^{-12}$			
λ_g^{oil}	[W/ (mK)]	[W/ (mK)]	[W/ (mK)]	[W/ (mK)]	[W/ (mK)]	[W/ (mK)]	[W/ (mK)]	$[-]$
	4.25547	-39.3553	140.965	-244.669	143.418	-48.4488	6.8884	0.152925

Table 4-2 Coefficients employed in the polynomial expression for the thermal conductivity, $\lambda_i(T)$ of the considered species.

Ref.	[115]	[115]	[116]
	N_2	**O_2**	**H_2**
a_1 $[W/(mK)]$	$-8.14736\cdot10^{-4}$	$6.85176\cdot10^{-4}$	101.93
a_2 $[W/(mK^2)]$	$1.1613984\cdot10^{-4}$	$9.39908\cdot10^{-5}$	0.3081
a_3 $[W/(mK^3)]$	$-1.1361924\cdot10^{-7}$	$-2.44914\cdot10^{-8}$	$4\cdot10^{-5}$
a_4 $[W/(mK^4)]$	$1.0617612\cdot10^{-10}$	$4.31987\cdot10^{-12}$	0
a_5 $[W/(mK^5)]$	$-5.4055704\cdot10^{-14}$	0	0
a_6 $[W/(mK^6)]$	$1.4542066\cdot10^{-17}$	0	0
a_7 $[W/(mK^7)]$	$-1.941557\cdot10^{-21}$	0	0
a_8 $[W/(mK^8)]$	$1.0105922\cdot10^{-25}$	0	0

in which R is the universal gas constant ($R = 8314.5\,J/kmol\,K$), and the coefficients were the same used in the thermodynamic dataset of the reaction mechanism [109], and are reported in Table 4-1.

For the gaseous n-hexadecane thermal conductivity value at $\bar{T}$, the polynomial expression suggested by Monogenidou et al. [114], validated in conditions varying from the triple point to 700 K and up to 50 MPa, was employed:

$$\lambda_g^{oil}(\bar{T}) = \frac{a_1 - a_2 T_r + a_3 T_r^2 - a_4 T_r^3 + a_5 T_r^4 - a_6 T_r^5 + a_7 T_r^6}{a_8 - T_r}, \tag{4-19}$$

where $T_r = \bar{T}/T_c^{oil}$, represents the ratio between the characteristic temperature $\bar{T}$ and the n-hexadecane critical temperature, $T_c^{oil} = 722\,K$ [113]. The relative coefficients are reported in Table 4-1, as well.

The thermal conductivity of the H_2/air gas mixture constituting the ambient in which the oil droplet is suspended, λ_∞, was evaluated by employing the widespread used empirical correlation proposed by Mathur et al. [117], also in accordance with the suggestion provided in a recent review work by Zhukov et al. [118] about the calculation of thermal conductivity of gas mixture containing hydrogen. Known the mixture composition expressed in terms of mole fractions, χ_i, the average thermal conductivity can be calculated as

$$\lambda_\infty(\bar{T}) = \frac{1}{2}\left[\sum_i \chi_i\,\lambda_i + \left(\sum_i \frac{\chi_i}{\lambda_i}\right)^{-1}\right]. \tag{4-20}$$

For the thermal conductivity of the $i\text{-}th$ species (with $i = H_2, N_2, O_2$) constituting the ambient gas mixture, λ_i, the following general polynomial expression was employed:

$$\lambda_i = \lambda_i(\bar{T}) = a_1 + a_2\bar{T} + a_3\bar{T}^2 + a_4\bar{T}^3 + a_5\bar{T}^4 + a_6\bar{T}^5 + a_7\bar{T}^6 + a_8\bar{T}^7\,. \tag{4-21}$$

The thermal conductivity of nitrogen, oxygen and hydrogen were evaluated using the polynomial coefficient values suggested by Abramenko et al. [119] and by Bergman et al. [120] respectively, validated in a range spanning from 80 K to 4500 K for nitrogen, from 100 to 2500 K for oxygen and from 400 K to 2000 K for hydrogen. The relative values are reported in Table 4-2. Finally, the n-hexadecane boiling temperature at reference atmospheric conditions, $T_{s,ref}$, was selected equal to 560 K and the molar heat of vaporization, $\Delta_v h_{oil} = 51.84\,KJ/mol$ at $T_{s,ref}$ [121].

4.1.3 Boundary conditions

A lubricant oil droplet can have a diameter ranging from 0.01 to 3.0 mm, according to literature data obtained through high-speed images [122]. Increasing longer induction times before ignition have been observed for droplets having increased larger sizes [123], [124]. Wang et al. [123] showed that the ignition delay time of an oil droplet having a radius of 200 μm was about 200 ms under operating conditions of 20 bar and 780 K. Considering that an ICE for automotive applications needs significantly less than 200 ms to cover one entire compression stroke, probably, a droplet radius smaller than 100 μm is required to trigger an auto-ignition event. Consequently, three different oil droplet sizes were selected for this study, namely, $r_s = 25, 50$ and 75 μm.

A temperature of the liquid in the inner region of the droplet, T_d, equal to 423 K was imposed, considering that oil droplets are usually released from the piston crevice due to the piston motion [125]. Thus, the temperature at which the oil is released should not differ much from that of the cylinder liner, which is usually lower than 500 K.

The thermo-chemical conditions of the ambient in which the oil droplet is suspended were selected in order to resemble typical conditions reigning within the combustion chamber of an ICE just before that the piston reaches the TDC, namely when undesired pre-ignitions of the charge are usually detected [123], [126]. Three (p, T_∞) values pairs were selected to analyse different scenarios, namely, $p = 30\ bar$ and $T_\infty = 800K$, $p = 50\ bar$ and $T_\infty = 900K$, $p = 70\ bar$ and $T_\infty = 1000K$. These conditions might be interpreted as either different piston locations along the last part of the compression stroke of the same engine or different thermodynamic conditions obtained with different engine architectures (compression ratios). The analyses were carried out at three different values of the fuel equivalence ratio of the H_2/air mixture surrounding the oil droplet, ϕ_∞, namely, 0.25, 0.5 and 0.75.

4.2 Numerical simulations set-up

The results obtained from the analytical model were used to initialize 0D numerical simulations performed within the open-source OpenSMOKE++ framework [127] and having the aim to quantify the ignition delay time variation along the radial coordinate, $\tau(r)$. The closed homogeneous batch reactor model with constant volume assumption was employed for solving the time dependent

balance equations for the total mass, the gas-phase species mass and energy. A criterion for the ignition delay time evaluation based on the maximum OH increase was used. The reduced reaction mechanism developed in a previous study [109] for $H_2/n\text{-}C_{16}H_{34}/air$ mixtures and consisting of 169 species and 2796 reaction was employed in the simulations. The 1D spatial domain employed in the computations with the analytical model was discretized using 50 points, distributed according to a spacing criterion based on 5 K temperature increment of the $T(r)$ function. The same values for p, T_∞ and ϕ_∞, considered in the calculations performed with the analytical model were considered for the numerical simulations.

4.3 Results and Discussion

Figure 4-3 reports the profiles of mass fraction, $Y_{oil}(r)$ (blue lines) and temperature, $T(r)$ (red lines) obtained from the analytical model, in correspondence of the three droplet radii, r_s, considered, namely 25 μm (dotted lines), 50 μm (dashed lines) and 75 μm (solid lines). The corresponding ignition delay profile, $\tau(r)$ (green lines), obtained from the 0D simulations, is reported for each condition in the bottom graph. Figure 4-3 refers to ambient conditions of $T_\infty = 900\ K$, $p = 50\ bar$, and $\phi_\infty = 0.5$. The variables are plotted against the radial distance from the droplet centre in Figure 4-3 (a), while the dimensionless distance from the droplet surface $\delta = (r - r_s)/r_s$ is considered in Figure 4-3 (b).The latter shows that the results scale with the droplet radius, as expected with the hypothesis at the basis of the model.

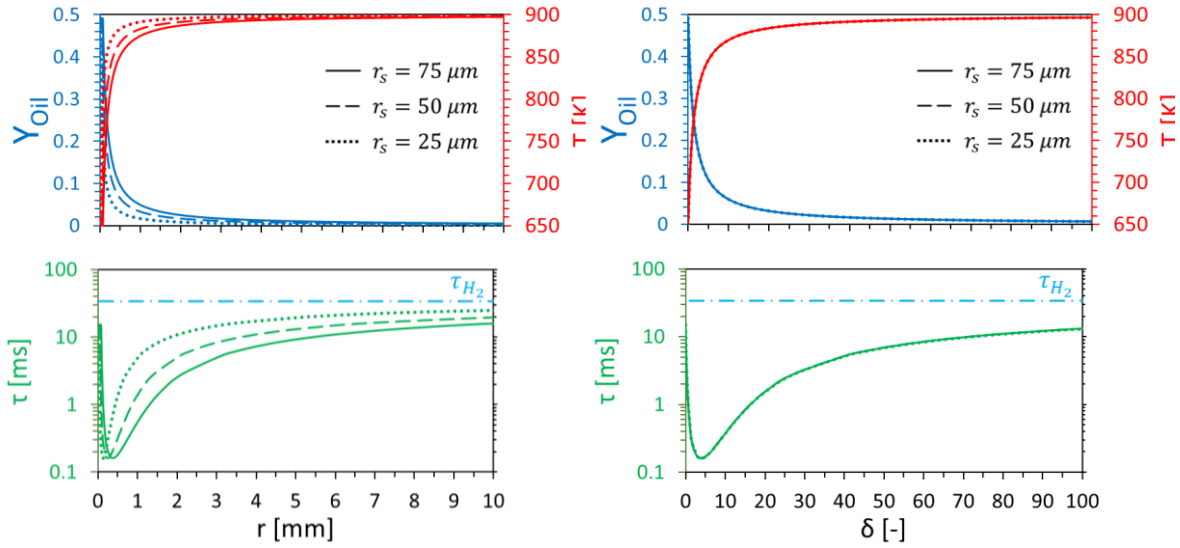

Figure 4-3. Mass fraction, Y_{oil}, and temperature, T, distributions obtained from the analytical model, together with ignition delay time distributions, τ, obtained from the 0D simulations, for three different droplet radii (25, 50 and 75 μm, at ambient conditions of $T_\infty = 900\ K$, $p = 50\ bar$, $\phi_\infty = 0.5$. The functions are plotted both against the radial coordinate, r (a) and the dimensionless distance, δ (b).

The main result is that $\tau(r)$ remains much lower than the reference value of the H_2/air mixture at the ambient conditions (τ_{H_2} light blue line) even at a significative distance from the droplet, regardless of the droplet size. Namely, in the thermo-chemical conditions of Figure 4-3, the H_2/air mixture would require about 34 ms to ignite, whereas, even at a distance equal to 100 droplet radii (where Y_{oil} is decreased to about 0.007) the H_2/oil mixture needs less than 15 ms. This suggests that the gas layer that surrounds the droplet represents an extremely high-reactive region that extends significatively far from its surface, and that even trace amounts of lubricant oil are sufficient to significantly increase the charge reactivity.

The oil mass fraction at the droplet interface, Y_{oil_s}, never exceeds a value of 0.5 (mainly due to the high ambient pressure) and moving away from the droplet, $Y_{oil}(r)$ quickly decreases, so that, at a distance equal to 5 droplet radii, its value is already less than 0.1. The temperature has an opposite trend, namely, $T(r)$ starts from a value at the droplet interface, T_s, of about 650 K, and quickly increases reaching a value of about 835 K after 5 droplet radii. Near the droplet surface, although very rich conditions are established, the temperature remains close to that of the liquid and significantly lower than that of the ambient, so that the chemical process is slowed down. Far from the droplet, the oil vapour concentration decreases drastically and with it the effects on the reactivity. As a consequence, the $\tau(r)$ function, shows a minimum located at a distance comprised between 2 and 12 droplet radii, range in which τ remains shorter than

0.5 ms, as can be more clearly observed in Figure 4-4, which reports a closer view of the values obtained in the proximity of the droplet surface.

Although a low temperature ($T_s \approx 650\,K$) and a quite significative mixture enrichment, the mixture obtained close to the droplet interface show high reactivity, with an ignition delay value that is more than halved ($\tau_s \approx 15\,ms$) in comparison to the reference value reached at infinite distance from the droplet ($\tau_\infty \equiv \tau_{H_2} \approx 34\,ms$). However, the ignition will probably start at the distance of about 4 droplet radii, where a minimum value of about 0.16 ms is recorded. It is worth to highlight that this ignition delay value is more than 2 orders of magnitude shorter than the hydrogen reference value, τ_{H_2}. As a reference, at this temperature (and pressure) the H_2/air mixture would require more than 100 ms to ignite (depending on the equivalence ratio considered).

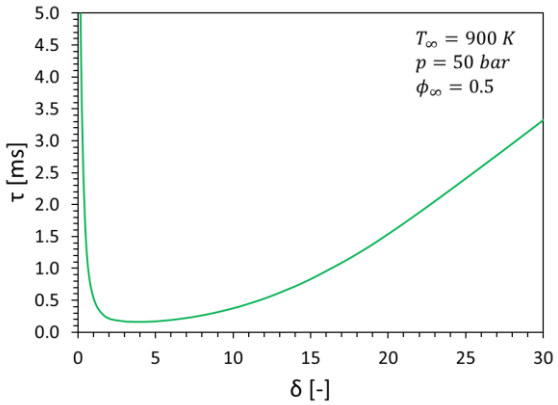

Figure 4-4. Ignition delay time, $\tau(\delta)$, variation close to the droplet surface at ambient conditions of $T_\infty = 900\,K$, $p = 50\,bar$, $\phi_\infty = 0.5$.

The extent of the effects induced by lubricant oil contamination on the charge reactivity changes depending on the thermo-chemical conditions of the ambient in which the oil droplet is suspended. Figure 4-5 (a) shows the results deriving from the calculations made at three different conditions in terms of ambient temperature and pressure, and in which the equivalence ratio, ϕ_∞, was kept constant at a value of 0.5. Although the temperature is increased from 800 to 1000 K, the oil mass fraction does not vary much from one case to another. This because the pressure was increased simultaneously with the temperature in the considered cases. The trend recorded for τ is similar to that shown in Figure 4-3 for all the considered cases, but with some peculiarities that is worth examining.

At 800 K and 30 bar, the thermodynamic conditions are not suitable for promoting the H_2/air mixture autoignition. Nevertheless, the $\tau(\delta)$ profile (green dotted line in Figure 4-5 (a)) shows a deep through, analogously to the other reactive cases.

This means that the presence of an oil droplet has the potential to drastically shift the explosion limit of hydrogen, by generating a highly reactive mixture during its vaporization even in condition in which hydrogen would not auto-ignite. At a distance of about 5 radii, the formed $H_2/oil/air$ mixture needs only about 1 ms to auto-ignite, and $\tau(\delta)$ remains shorter than 10 ms up to a distance equal to 25 radii. This is a remarkable finding, if one considers that a spontaneous ignition of the charge could be locally initiated by an oil droplet even though the thermodynamic conditions are considered safe for the operation of a hydrogen engine.

At 1000 K and 70 bar, the H_2/air mixture would require about 2.5 ms to auto-ignite. With the presence of an oil droplet, this time can be reduced to about 60 μs at a distance slightly lower than 5 droplet radii (cf. solid lines in Figure 4-5 (a)), highlighting a maximum reduction of about 98% induced by the oil vapour at the highest ambient temperature and pressure considered.

A less marked dependence upon the ambient equivalence ratio arose from the results showed in Figure 4-5 (b), in which $T_\infty = 900\,K$ and $p = 50\,bar$ were considered. This suggests that the lubricant oil effects are significative, independently of the hydrogen content in the charge. The increased reactivities is mainly attributable to the low-temperature chemistry involved in the long straight-chain alkanes oxidation, in which the H_2-O_2 system play a quite marginal role [109], [124]. The minimum value of τ is about 0.15 ms and it is recorded at approximately 4.5 radii, for all the conditions considered. It is meaningful to point out that the ignition delay shortening induced by lubricant oil is much more pronounced than that induced by an increase in the equivalence ratio value of the H_2/air mixture. Namely, τ_{H_2}, changes approximately from 53 to 26 ms, when ϕ_∞ is increased from 0.25 to 0.75 (cf. light blue lines in Figure 4-5 (b)), while the reduction induced by the oil contamination can reach up to two orders of magnitude.

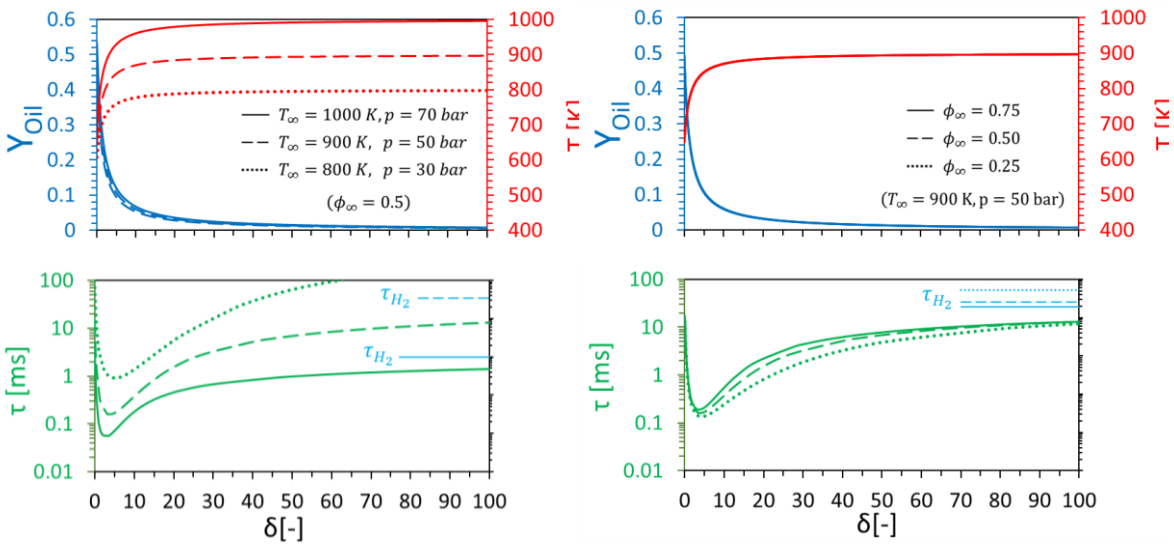

(a) (b)

Figure 4-5. Mass fraction, $Y_{oil}(\delta)$ and temperature, $T(\delta)$ distributions obtained from the analytical model, together with ignition delay time distributions, $\tau(\delta)$, obtained from the 0D simulations. Results obtained with $\phi_\infty = 0.5$ for three different pressures and temperatures (a). Results obtained at $T_\infty = 900\ K$, $p = 50\ bar$ for 3 different ambient equivalent ratios (b).

Finally, Figure 4-5 (b) shows that the extension of the region with very short values of τ increases with the decrease of the ambient equivalence ratio. Considering that a comparable minimum value of τ is obtained for the three cases (i.e., about 0.18 ms), the leanest case (i.e., $\phi_\infty = 0.25$) looks the most dangerous one. Such a result needs to be taken under particular consideration in the light of the development direction of hydrogen ICEs oriented towards lean operating combustion modes.

5 Detonation of H_2-air mixture due to hot-spots

5.1 Introduction

Within the combustion chamber of an internal combustion engine, regions of high local temperatures called hot spots can arise based on multiple reasons some of which being hot edges of intake/exhaust valves, carbon deposits as part of the emissions from previous cycles and thermal inhomogeneities of the combustible mixture or simply air (in case of DI engines).

These hot spots due to their higher local temperature envelope a certain mass of the charge that has a lower ignition delay as compared to the rest of the mixture outside the hot spot region. This thermal inhomogeneity becomes a source of ignition within an unburnt mass of charge and hence initiates a reaction front propagating radially outwards towards a decreasing temperature gradient.

If a reaction front couples with the pressure/acoustic wave it generates, the phenomenon leads to detonation with a pressure detrimental to the components of the engine. Such detonations can be either supersonic or subsonic depending on the initial temperature gradient within the hot spot from which a detonating wave front starts propagating.

In this chapter 1D detonation simulations are run using OpenFOAM and the effect of different temperature profiles within the hot spot on the resulting mode of detonation is studied and compared to identify the different modes of detonation they initiate.

5.2 State of the art

Auto-ignition, reaction front propagation, and detonation development are foundational events in combustion, and are relevant to the occurrence of engine knock. Since mixtures in practical situations are rarely homogeneous, auto-ignition would first occur at some location induced by external energy deposition, heat transfer, and turbulent energy dissipation [128].

Following Zel'dovich [129], an initial reactivity gradient arising from mixture/temperature inhomogeneities can give rise to different auto-ignition modes, including thermal explosion, supersonic auto-ignition deflagration, detonation development, subsonic auto-ignition deflagration, and simply laminar deflagration.

Bradley and coworkers [130] proposed a detonation diagram normalized by dimensionless parameters to determine the critical conditions of auto- ignition modes, which was widely utilized in the studies of engine knock [131] and deflagration-to-detonation transition (DDT) [132]. Liberman et al. [133] clarified the critical steepness of the temperature gradient for different modes and addressed the significance of chemical kinetics. The dimensionless parameters used for the Bradley diagram are further elaborated in section 5.2.1.

Chen and coworkers [134], [135] elucidated the effects of fuel properties and additives on auto-ignition and detonation development. Later, the role of temperature and concentration stratification and their interactions was investigated in Ref. [136] . Pan et al. [137], [138] identified the significance of the transient behaviour of multiple variables in auto-ignition and detonation development.

Different autoignition modes can be initiated by non-uniform initial temperatures, manifesting the transition from supersonic to subsonic combustion modes with increasing temperature gradients however in a non-monotonous trend.

Pan et al. [139] have identified a universal detonation response diagram with multiple, non-monotonic boundaries of auto-ignition modes under engine-relevant conditions. Specifically, it was shown that with increasing gradient steepness, in addition to the conventional three regimes of supersonic auto-ignition deflagration, detonation development, and subsonic auto-ignition deflagration, the reaction front propagation speed would first decrease dramatically and then increase, hence inducing additional detonation regimes. Consequently, two detonation peninsulas were identified, with the first corresponding to the well-established Bradley detonation peninsula and the

second manifesting a broader detonation regime. Figure 5-1 shows the detonation peninsula diagram adapted from [139] where the Bradley detonation peninsula is shown in dashed lines.

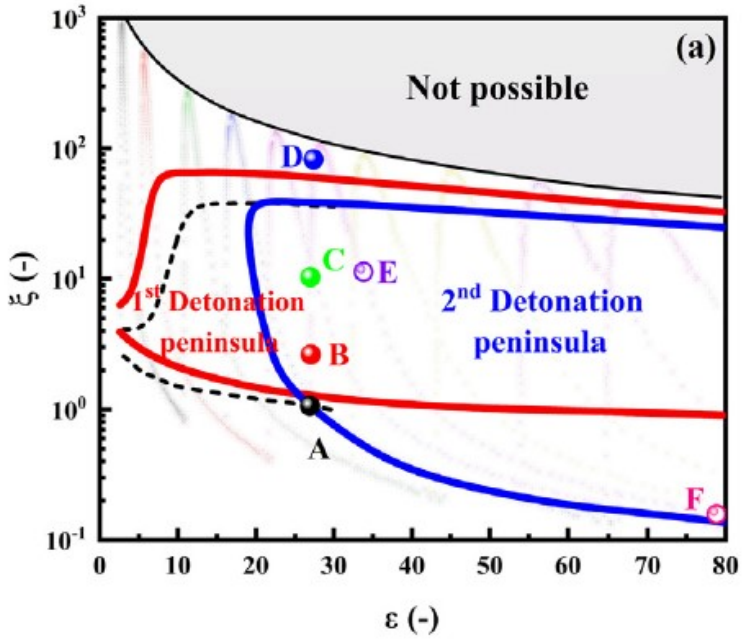

Figure 5-1 Detonation diagram in spherical coordinates. $\xi - \varepsilon$ diagram. The dashed lines denote the results of Ref. [130]. Figure adapted from [139].

Detonation response diagrams (hot spot radius vs ΔT) identify the regimes/modes of detonation as a consequence of increasing the radius of hot spot x_0 as well as the steepness of the temperature within the hot spot and hence ΔT. Because of the stretching effect of the reacting front in spherical coordinates and slower propagating reacting front as compared to one in a planar direction, different detonation response diagrams in spherical and planar coordinates are observed effecting the limits of both detonation peninsulas. This has been studied by Pan et al. [140] and the detonation response diagrams for both coordinates for H_2/air have been adapted to show in Figure 5-2.

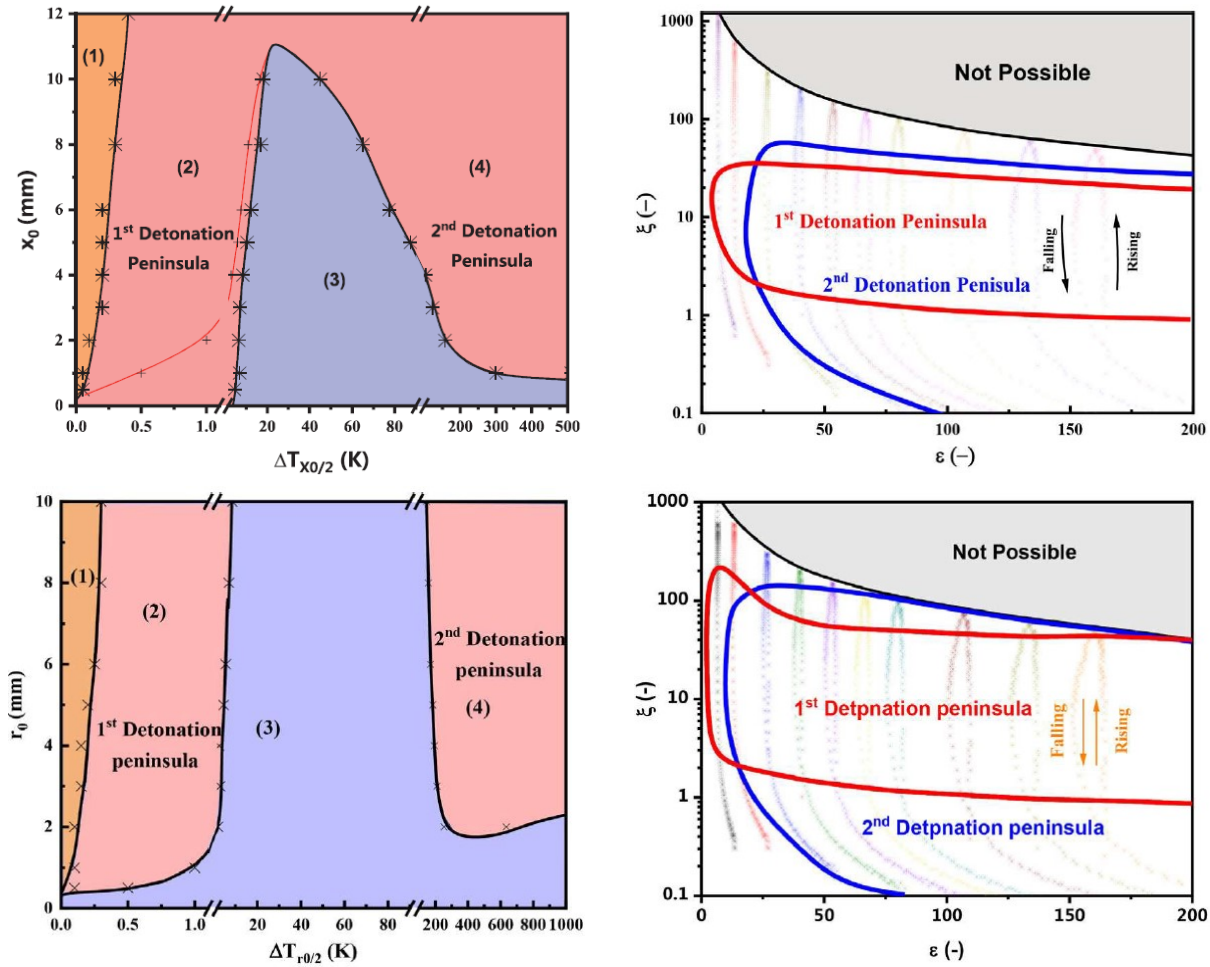

Figure 5-2 Detonation response diagram and $\xi - \varepsilon$ diagrams of multi-regime detonation development of H_2/air in planar configuration (top) and spherical configuration (bottom). Adapted from [140].

5.2.1 A classification diagram

A diagram introduced by Bradley and colleagues [141] and known also as "detonation peninsula" can be employed to classify the various modes of reaction propagation originating from an auto-ignition centre. It has been extensively used for analysing abnormal combustion mode in internal combustion engines and other applications [142], [143], [144], [145].

Bradley's diagram relies on Zel'dovich's theory, which was originally devised to investigate pre-ignition events triggered by hot spots [146]. The employed approach assumes that reactivity gradients arise solely from temperature changes within a small, assumed spherical volume. Consequently, the local propagation speed of the auto-ignition reaction wave, u_a, can be expressed as follows in a spherical coordinate frame [147]:

$$u_a^{-1} = \frac{d\tau}{dT}\frac{dT}{dr}, \tag{5-1}$$

where, r is the radial coordinate, and τ the ignition delay time. A linear temperature increase (i.e., $\frac{dT}{dr} = const$) was imposed along r, allowing the study of various modes of auto-ignition propagation by varying the steepness of the temperature gradient. According to this gradient mechanism, a dimensionless parameter, ξ, was introduced to ascertain the presence of resonance between auto-ignition and acoustic time. In the simplified case of hot spots, it can be defined as:

$$\xi(T) = \frac{dT}{dr}\left(\frac{dT}{dr}\right)_c^{-1}, \tag{5-2}$$

in which $\left(\frac{dT}{dr}\right)_c = \left(\frac{d\tau(T)}{dT}a\right)^{-1}$ expressed the critical temperature gradient leading to chemical resonance, being a the speed of sound evaluated at half of the hot spot radius. According to this definition, subsequent studies have referred to ξ as the normalized temperature gradient (cf., e.g., [148], [149]).

In addition, a detonation wave emerges as the heat released by the auto-ignitive front rapidly transfers into the acoustic wave. Thus, a second dimensionless parameter, ε, was introduced to assess the degree of coupling between acoustic effects and exothermic reactions:

$$\varepsilon = \frac{r/a}{\tau_e}. \tag{5-3}$$

It compares the time taken for the acoustic wave to traverse the hot spot with the excitation time, which evaluates the duration of the major heat releasing phase [150], defined as the time interval between 5% and maximum heat release rate [147].

It is noteworthy that, in this theory, ξ mirrors the dependence of τ upon the temperature (having assumed $\frac{dT}{dr}$ and a to be constant). To evaluate this dependence, 0D simulations employing an appropriate chemical reaction scheme can be conducted to assess the term $\frac{d\tau(T)}{dT}$ and readily obtain the value of ξ. From the same simulations, the excitation time, τ_e, can be extracted for calculating the dimensionless parameter ε. Considering that the speed of sound, ignition delay and excitation time vary within the hot spot, all the parameters were evaluated at half of the hot spot radius, i.e., at $r = \frac{r_0}{2}$.

Although Equation (5-2) indicates that chemical resonance occurs at $\xi = 1$, there exists a range of values of this parameter within which transitions to a developing

detonation is observable. The parameters ξ_l and ξ_u were introduced to designate the corresponding lower and upper limiting values, respectively, of the so-called "detonation peninsula". According to the classification proposed by Bradley and colleagues [141], [147], [151], [152] five modes of reaction front propagation can be visualized on the proposed classification diagram: for $\xi = 0$ auto-ignition occurs instantaneously without the need for a temperature gradient, thus there is a thermal explosion; the mode corresponding to $0 < \xi < \xi_l$ represents a supersonic auto-ignitive propagation of the reaction front; in the mode defined by $\xi_l < \xi < \xi_u$ both developing and developed detonations occur; subsonic auto-ignitive propagation is observed for $\xi_u < \xi < a/u_l$ (this mode can be also referred as "reactive-hydrodynamic wave" [153]); laminar burning deflagration at the laminar burning velocity characterises the mode corresponding to $\xi > a/u_l$ (i.e., a conventional flame propagating by molecular diffusive and conductive mechanisms).

Figure 5-3 (a) illustrates the classification diagram according to the results recently obtained by Pan et al. [148] (black lines). The boundaries originally obtained by Bradley and colleagues [141] are also reported for comparison (green lines). The numerical simulations performed by Pan et al. [148] are more recent and extended over a wider range of ε values in comparison to those considered by Bradley and colleagues [141]. Thus, the diagram by Pan et al. [148] is considered as a reference in this study (dashed lines in the plots of Figure 5-3 indicate extrapolated values).

It is worth highlighting that the diagram in Figure 5-3 (a) was obtained for an equimolar H_2/CO mixture at $T = 1000\,K$, $p = 40\,atm$ and $\phi = 1$. In the early studies, it was supposed that the detonation peninsula could be universally valid, as it was initially shown to be also applicable to iso-octane and n-heptane [152]. However, the related data were obtained for relatively small values of ε, not exceeding 9 and 4, respectively. Nevertheless, the classification diagram of Figure 5-3 (a) was used in subsequent studies without much further discussion (see, for instance, the work by Robert and Poinsot [145]). More recent studies (see, e.g., [154], [155], [156], [157]) have suggested that the peninsula boundaries may vary depending on the fuel mixture. In addition, although still not completely clear, such studies have suggested that the initial temperature, initial pressure, and equivalence ratio might have a non-negligible influence.

Therefore, in Figure 5-3 (b), the boundaries for pure H_2 obtained by Zhang et al. [156] (light-blue lines), Gao et al. [157] (pink lines), and Pan et al. [158] (yellow lines) under the same thermodynamic conditions are reported. Differences with the H_2/CO mixture are notable in the extent of the developing detonation region at low ε values. The deflagration limit also appears to be different. However, discrepancies among the results relative to pure H_2 are also evident at low ε, with

the results by Zhang et al. [156] suggesting that the developing detonation region might encompass lower ε values and higher ξ values. Further research is needed in this regard.

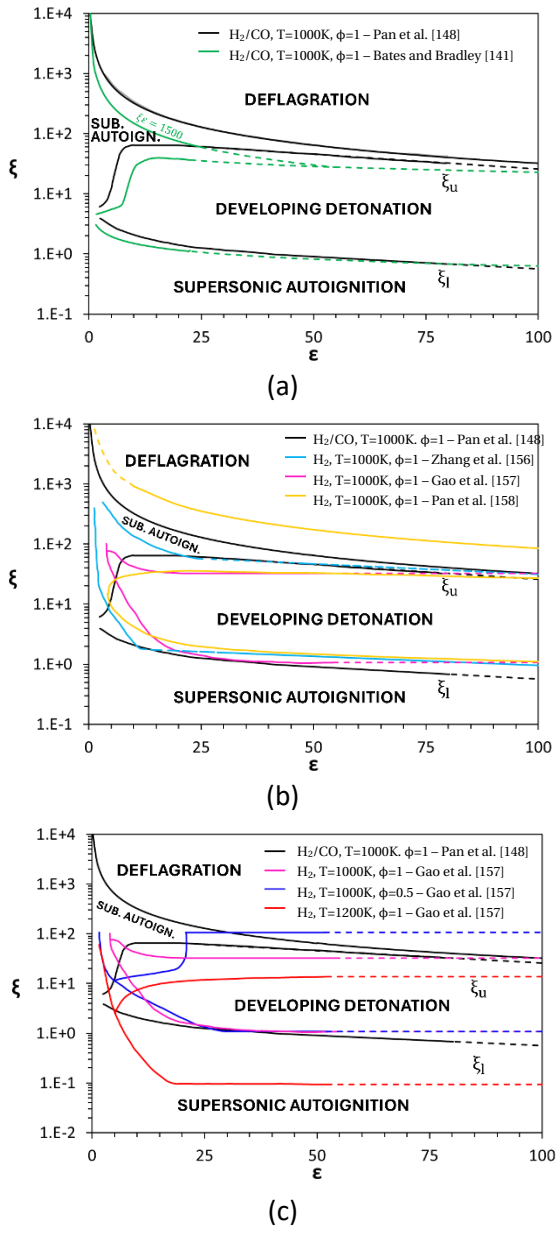

Figure 5-3 Classification diagram proposed by various research groups for different fuel mixtures and thermodynamic conditions.

Gao et al. [157] also studied the influence of thermodynamic conditions outside the “hot spot”, suggesting that the influence of pressure is limited, while that of temperature and equivalence ratio can be relevant. Figure 5-3 (c) reports the detonation peninsulas obtained for pure H_2 at 40 atm for $T = 1000\ K$ and $\phi = 0.5$ (blue lines) and for $T = 1200\ K$ and $\phi = 1$ (red lines). A reduction in the equivalence ratio value from 1 to 0.5 produces a significant modification of the

upper boundary of the detonation peninsula. Consequently, the risk of generating a detonation is reduced at low values of ε and increased at higher values. An increase in temperature shifts the developing detonation region towards lower ξ values, indicating that a lower temperature gradient is needed to generate a detonation. The effects induced by temperature appear more significant on the lower boundary. Unfortunately, there are no results available at temperatures lower than 1000 K. Therefore, for the present analysis, the diagram proposed by Gao et al. [157] for pure H_2 at $T = 1000\ K$ and $\phi = 0.5$ (blue lines) was considered in addition to the one obtained by Pan et al. [148] for H_2/CO (black lines).

5.3 Effects of initial temperature on multi-regime detonation development

As discussed thoroughly in Chapter 4, the autoignition time delay is highly sensitive to temperature. Similarly, the propagation of the reaction front in different initial homogeneous temperature fields results in slightly skewed detonation response diagrams because of an earlier or later transition between the various modes of detonation as shown in Figure 5-4. This causes a change in the dimensionless parameters ε and ξ and therefore the shape of the two detonation peninsulas particularly at higher hot spot diameters.

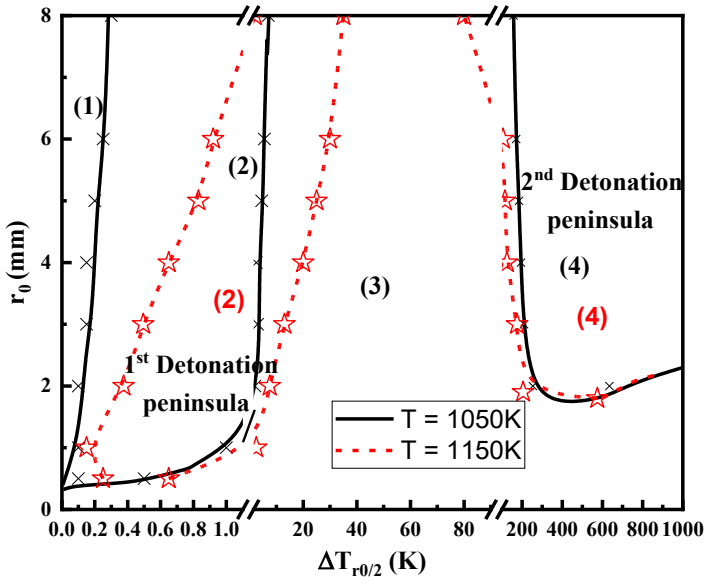

Figure 5-4 Detonation response diagrams for H_2/air in spherical coordinates at different initial temperatures. Reaction front propagation modes are (1) supersonic auto-ignition deflagration, (2) detonation development, (3) subsonic auto-ignition deflagration, and (4) detonation development. Adapted from supplementary materials in [140].

5.4 Numerical simulations setup

In this work transient auto-ignition processes of stochiometric H_2/air mixtures initiated by non-uniform initial temperatures in a one-dimensional "planar" domain are considered.

The initial temperature distribution within the hot spot will depend on the temperature trend variation with the independent axis (x) chosen among which are linear and exponential of x in the present work. The two respective temperature distributions compared in this study are represented by Equations (5-4) and (5-6).

Where t and x are the temporal and spatial coordinates, respectively; x_0 the radius of the hot spot; L the length of the planar domain; dT/dx is the temperature gradient; and T_0 is the uniform initial temperature outside the hot spot. Furthermore, L = 4.0 cm, T_0 = 1047.5 K ($\tau_{ID} \approx 1ms$), and p_0 = 40 atm are held for all cases studied. A hot spot value of $x_0 = 5mm$ has been used across all simulations.

1D transient auto-ignition simulations with detailed chemical kinetics were performed utilizing detonationFoam [159]: An open-source solver for simulation of gaseous detonation solver based on OpenFOAM v6. The solver considers the species' equations and detailed finite-rate chemistry and thereby the compressible, multi-component, reactive flow can be simulated. The mixture-averaged transport model is used to accurately evaluate the detailed transport coefficients. The improved HLLC-P approximate Riemann solver incorporated within the solver accurately captures the propagation of shock wave and contact discontinuity. Second-order CrankNicolson scheme in time and central difference schemes in space are used. The accuracy of the solver detonationFoam has been validated in [159] against commercial code A-SURF [134], [160].

For the initial validation of the solver in this work, mesh size equal to $1\mu m$ and corresponding timestep limited by a Courant number (Courant–Friedrichs–Lewy condition) equal to 0.015 is imposed to ensure adequate numerical resolution of the reaction front, pressure/shock wave, and detonation development. However, for faster acquisition of a large set of results but still adequately representative of the real phenomenon, a mesh size equal to $50\mu m$ is used. This mesh size equal to $50\mu m$ while maintaining a Co=0.015 gives Δt of about 2e-9 seconds and hence the resulting time of first sensible ignition in term of heat release rise is slightly advanced as compared to a mesh of $1\mu m$ with Δt = 1e-10 seconds.

Symmetry and zero-Gradient boundary conditions are imposed on the left and right boundaries, respectively. The total physical time is adjusted to ensure the completion of reaction front propagation in the entire domain. The reaction front

is defined as the location of the maximum heat release rate $Q\ \left[\frac{J}{m^3 \cdot s}\right]$. Considering the significance of chemical kinetics in the Deflagration to Detonation Transition (DDT), the same detailed reaction mechanism [24] is adopted as used in section 2.2 of Chapter 2. Figure 5-5 shows a schematic of the boundary and initial conditions for the simulations in planar coordinates.

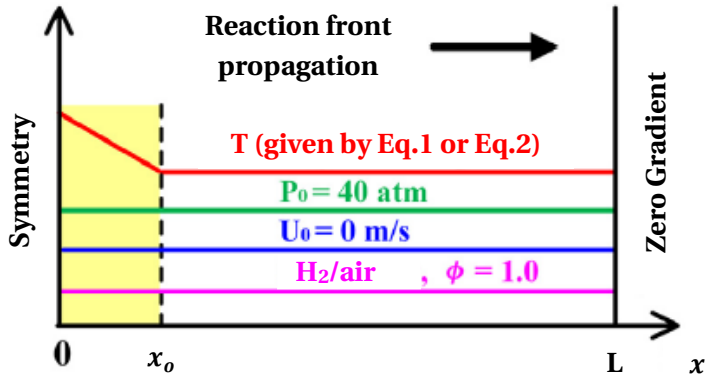

Figure 5-5 Schematic of the boundary and initial conditions for the 1D-simulations in planar coordinates used in this work.

5.5 Linear vs exponential gradient of temperature within the hot-spot in a stochiometric H_2-air mixture

Detonation response diagrams in planar coordinates [140] are used as reference for validation against the opensource detonationFoam solver used in this work. At a constant hot spot radius of 5 *mm*, the solver shows very good consistency with the data in the literature. The validation result is shown in Figure 5-6 identifying the limits of the 1st and 2nd peninsula. The solver itself has been validated by its authors against ASURF detonation simulations in [159]. The same results in Figure 5-6 have been superimposed on the original figure adapted from Pan et al 2023 [140] shown in Figure 5-7.

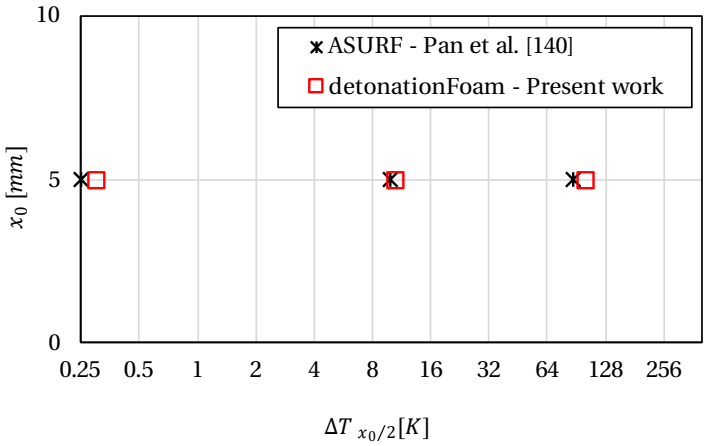

Figure 5-6 Validation of solver 'detonationFoam' against literature data [140] at $x_0 = 5\ mm$ with linear temperature gradient inside hot spot.

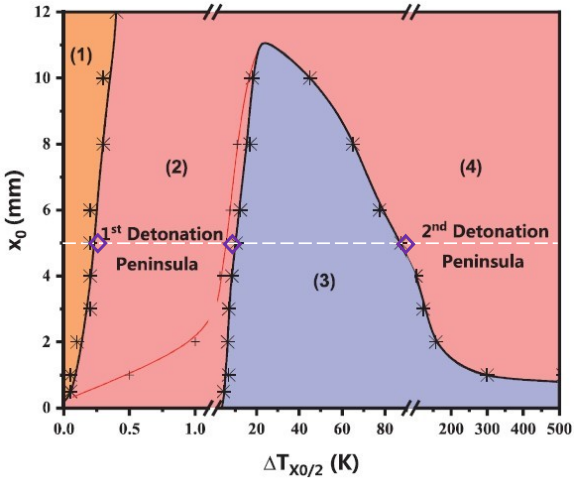

Figure 5-7 Detonation response diagram for H_2/air at $T_0 = 1050\ K$ and $p_0 = 40\ atm$ in planar coordinates (adapted from [140]). Simulation results from present work (purple diamond markers) using detonationFoam solver [159] have been superimposed for comparison.

In literature the gradient of temperature used for such simulations has always been linear.

$$T(x) = \begin{cases} T_{x_0/2} + \left(x - \frac{x_0}{2}\right)\frac{dT_0}{dx}, & 0 \le x < x_0 \\ T_0, & x \ge x_0 \end{cases} \tag{5-4}$$

However, A more realistic approach to model the temperature profile inside a hot spot is an exponential gradient of temperature. Turbulent convection inside the engine cylinder causes a rapid dissipation of heat at the radial limit of the hot spot, however the core remains at a comparatively much higher temperature which indeed is true for solid deposits acting as hot spots.

An exponential function of temperature in generic form would be

$$T = a \cdot e^{-x} + b \tag{5-5}$$

where a is the exponential growth coefficient, x being the normalized longitudinal axis of the reaction front propagation travel (the principal axis of a 1D domain), and b is the y-axis value of the exponential asymptote reached at $x = +\infty$.

The exponential function of temperature within the hot spot is given by Equation (5-6) and shown in Figure 5-8. ΔT_{max} is the y – intercept and hence the maximum temperature at the center of the hot spot ($x = 0$) and x_0 being the hot spot radius. Here the coefficient n has been introduced to calibrate the exponential decay within the hot spot between $x = 0$ and $x = x_0$, and is given by $n = -ln(\Delta T_{asymptote}/\Delta T_{max})$. $\Delta T_{asymptote} = 0.01K$ has been used to achieve the homogenous base temperature T_0 exactly at $x = x_0$.

$$T = \begin{cases} \Delta T_{max} \cdot e^{-n\frac{x}{x_0}} + (T_0 - \Delta T_{asymptote}), & x \le x_0 \\ T_0, & x \ge x_0 \end{cases} \tag{5-6}$$

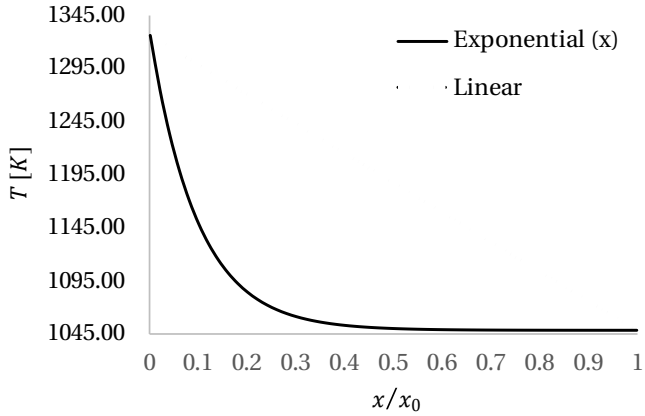

Figure 5-8 Linear and exponential temperature gradients inside the hot spot as given by equations (5-4)and (5-6) respectively.

Previous works [130], [139], [140] have used the centre of the hot spot ($x_0/2$) for **linear** temperature gradients as the reference to calculate ΔT which is given by:

$$\Delta T_{x_{ref}}^{linear} = \Delta T_{x_0/2} = T_{x_0/2} - T_0 \tag{5-7}$$

Where $T_{x_0/2}$ is the temperature at the center of hotspot. Here $x_{ref} = x_0/2$.

However, for the **exponential** temperature gradients used in this work, $\Delta T_{x_{ref}}$ is calculated from a reference value x_{ref} given by Equation (5-9) by evaluating Equation (5-9).

$$x_{ref} = \frac{1}{\left(\frac{x}{x_0}\right)_{ref}^{exponential}} \tag{5-8}$$

$$\left(\frac{x}{x_0}\right)_{ref}^{exponential} = -\frac{ln\left\{\frac{T_{x_0/2}^{linear} - \left(T_0 - \Delta T_{aymptote}\right)}{\Delta T_{max}}\right\}}{n} \tag{5-9}$$

The selection of a variable x_{ref} in case of an exponential temperature gradient lies in the nature of an exponential curve having almost negligible temperature difference between $x = x_0/2$ and $x = x_0$ even though the maximum temperature at the centre of hot spot ($x = 0$) is significantly high from T_0.

$$\Delta T_{x_{ref}}^{exponential} = T_{x_{ref}}^{exponential} - T_0 \tag{5-10}$$

A few test cases close to the boundaries as well as inside the two detonation peninsulas, seen in Figure 5-7, have been selected to compare a change in ΔT at which the transition occurs between the different modes of detonation for both the cases of linear and exponential gradients of temperature within the hot spot. Table 5-1 summarizes the cases studied in this work.

Table 5-1 Case studies parameters for comparison between linear and exponential dT/dx inside the hot spot and their effect on subsequent detonation transition.

Case	x_0 [mm]	ΔT [K]
A	5.0	2
B	5.0	100
C	5.0	200

5.5.1 Results and Discussion

The results being shown may not adhere quantitatively to the correct spatial and temporal position of the reacting and acoustic waves because of the comparatively large mesh size ($\Delta x = 50\ \mu m$) however, qualitatively, it is sufficient to illustrate the difference between the two cases studied in this work.

Figure 5-9 to Figure 5-11 show the pressure and temperature profiles of the representative cases in each regime at $x_0 = 5\,mm$. Solid lines represent exponential gradient, and dashed lines represent linear gradient of initial temperature within the hot spot.

Case A ($\Delta T = 2\ K$)

As compared to the Linear dT/dx, the first ignition in the case of an exponential dT/dx is delayed at such a low temperature different of $2\ K$ (Figure 5-9). This is associated with the profile of an exponential curve in this case, where only a small portion of the hot spot close to the centre ($x = 0$) has the highest temperature difference whereas in the linear dT/dx case, the whole hot spot can be averaged to have a temperature very close to T_0 leading to a faster thermal explosion. The ignition delay difference between the two cases causes their relative spatial position to be at a constant delta that is maintained across the whole domain because of the same constant supersonic velocity of around $900\ m/s$.

The reacting and pressure wave are both coupled in the two cases, with a peak of $190\ bars$ and a propagating detonation wave develops inside the hot spot and continues steadily till the end of the domain. Both these cases lie within the 1st detonation peninsula.

Case B ($\Delta T = 100\ K$)

In Figure 5-10, both exponential dT/dx and linear dT/dx cases represent supersonic detonation wave propagation. With such a high temperature difference between reference temperature inside the hotspot $T_{x_{ref}}$ and the ambient temperature T_0, the detonation due to the exponential dT/dx indicates now a much lower ignition delay difference as compared to the linear dT/dx. Once again, the nature of an exponential curve accumulates most of the high temperature region close to the centre of the hot spot ($x = x_0$) and because of a high $\Delta T = 100\ K$, the difference between the two cases starts to close.

Case C ($\Delta T = 200\ K$)

The very high $\Delta T = 200\ K$ (Figure 5-11) results in a similar temporal and spatial positioning of the detonation front for both exponential and linear dT/dx cases. Like Case B, a propagating detonation wave develops inside the hot spot and continues steadily till the end of the domain. This result identifies a similar ignition delay at very high ΔT values irrespective of the initial temperature gradient profile inside the hot spot.

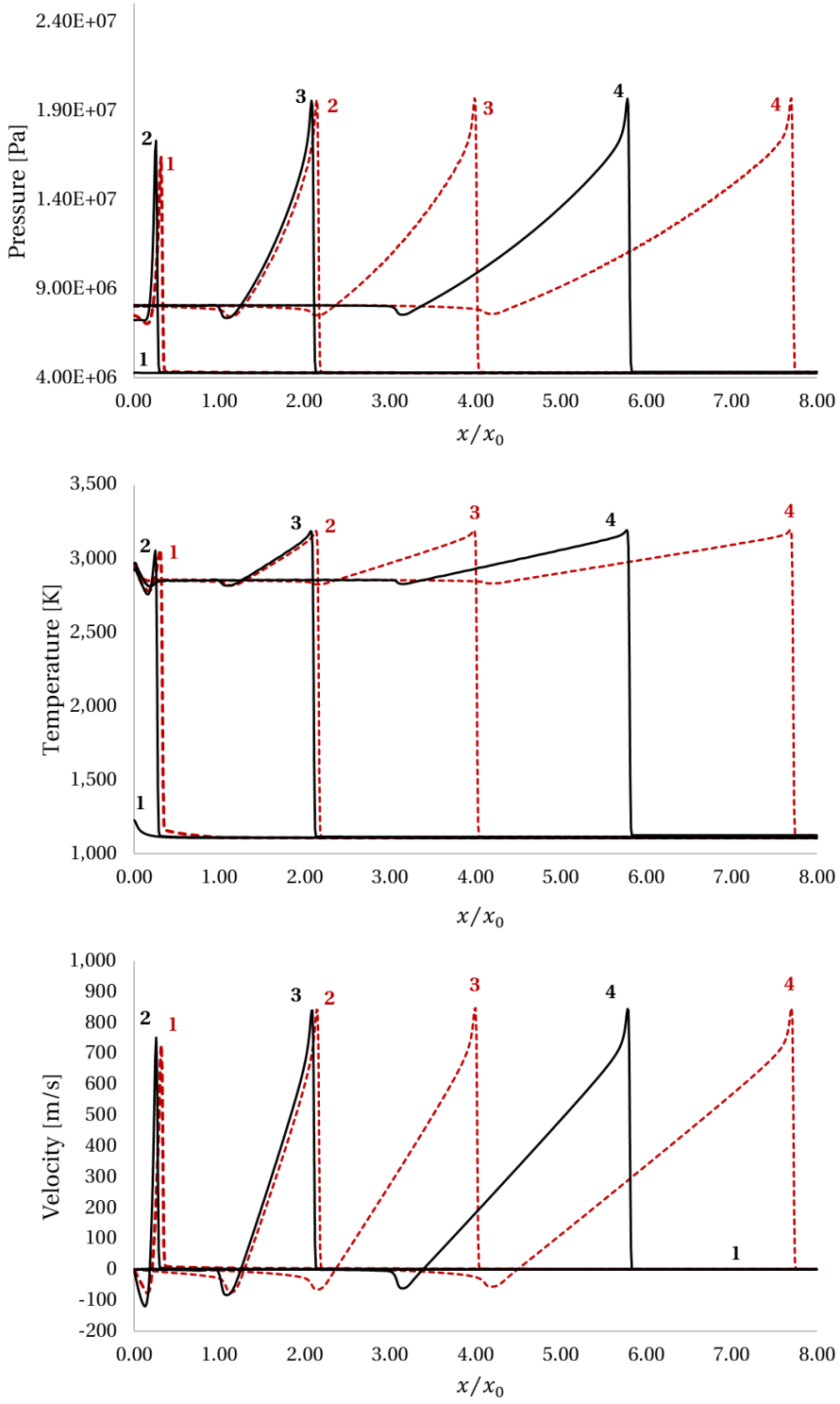

Figure 5-9 Case A ($\Delta T = 2\ K$): Temporal evolution of pressure and temperature. Solid black lines: Exponential dT/dx, Dashed maroon lines: Linear dT/dx. Time sequences are 1 – 1000 μs, 2 – 1005 μs, 3 – 1010 μs, 4 – 1020 μs.

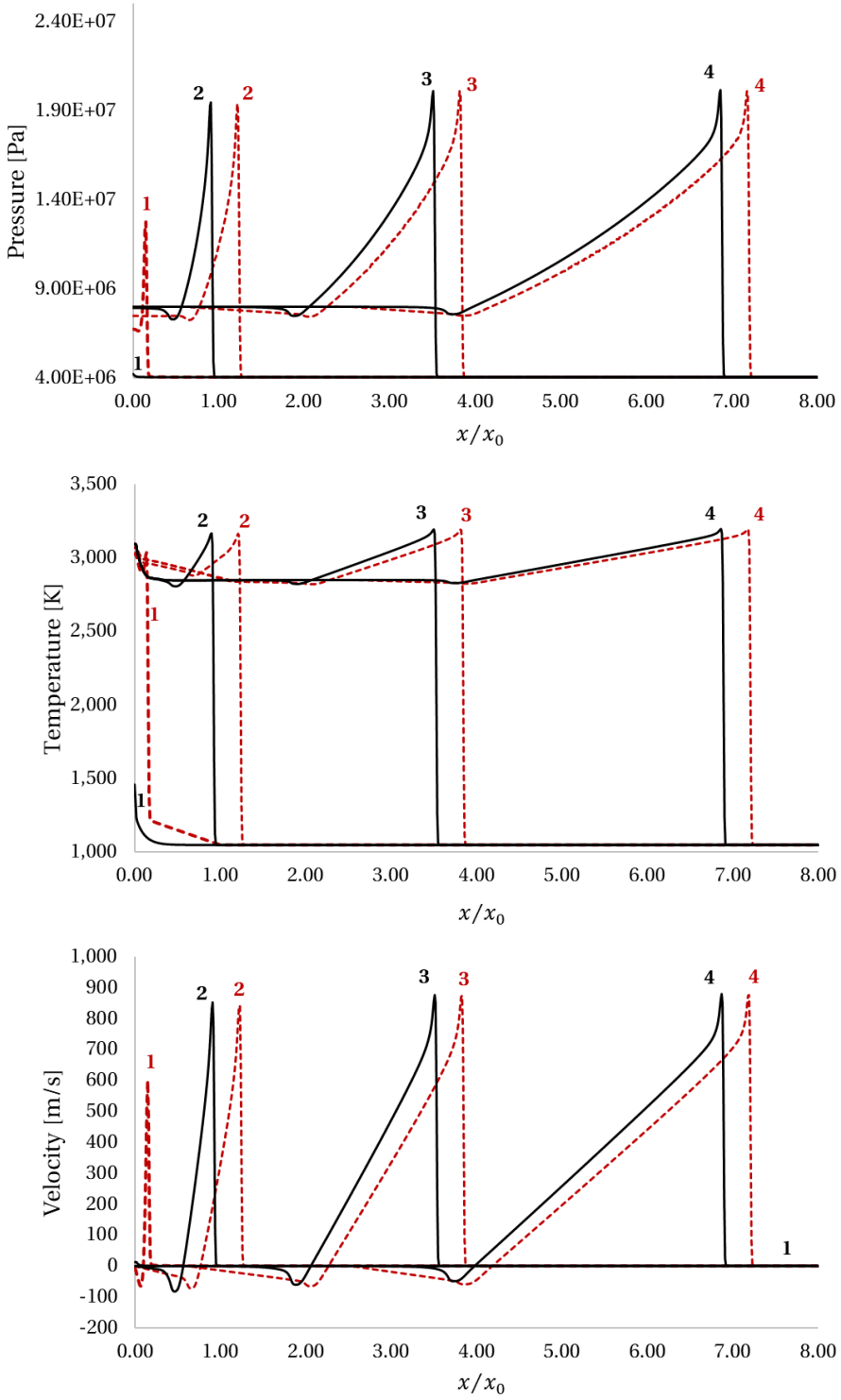

Figure 5-10 Case B ($\Delta T = 100\ K$): Temporal evolution of pressure and temperature. Solid black lines: Exponential dT/dx, Dashed maroon lines: Linear dT/dx. Time sequences are 1 – 31 μs, 2 – 34 μs, 3 – 41 μs, 4 – 50 μs.

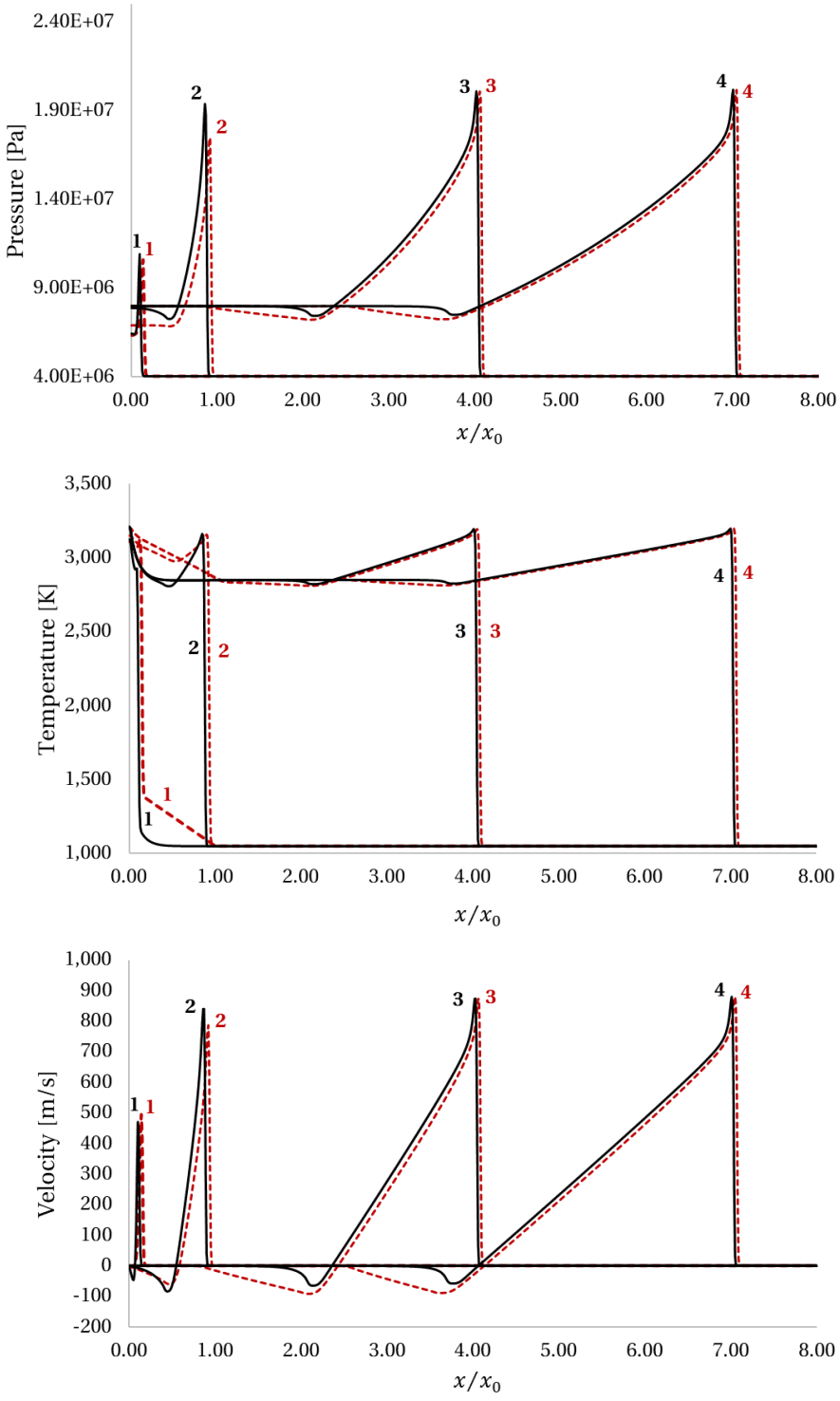

Figure 5-11 Case C ($\Delta T = 200\ K$): Temporal evolution of pressure and temperature. Solid black lines: Exponential dT/dx, Dashed Maroon lines: Linear dT/dx. Time sequences are 1 – 1.3 μs, 2 – 3.5 μs, 3 – 12 μs, 4 – 20 μs.

6 Summary and outlook

The ongoing development of hydrogen ICEs requires a design baseline that depends on analytical and numerical results performed on H_2-air combustion and its effect on engine geometry. The present work objectively made use of the chemical kinetics of H_2 to correlate its explosive behaviour to the thermodynamic state that can be present inside an ICE during its operation. The initial pressure, p_i, initial temperature, T_i, and the equivalence ratio, ϕ, of the mixture were taken into consideration to assess the occurrence of auto-ignition through a thorough analysis of the H_2-air explosion limit, which was essential for defining the Maximum Safe Geometrical Compression Ratio (MSGCR) of an engine. Three different criteria have been established in the present work, namely, static, time-based and an integral one.

The 3rd explosion limit, being that of interest to ICE applications, is numerically simulated in the present work implementing the Kéromnès kinetic mechanism and is expanded further in this study to develop a H_2 reactivity map for engine applications, spanning a wide range of ignition delay times, τ_{ID}, ($1\ sec\ to\ 1\ ms$) and ϕ ($0.1 - 1$). The map demonstrates this wide variation through a horizontal shift of the explosion limit on the $p - T$ plot. An increase in auto-ignition temperature at constant pressure is observed when moving from stochiometric ($\phi = 1$) to very lean ($\phi = 0.1$) mixture compositions. The reactivity map allows for the creation of a computational database for calculations of instantaneous τ_{ID} values corresponding to any arbitrary in-cylinder state (p, T, ϕ) as the piston travels through either a compression or an expansion stroke. Even though a lean combustion is the primary target, explosion limits for much higher ϕ up to 5 have been simulated to provide their applicability to DI H_2 engines in which the mass distribution of fuel is heterogeneous within the injected jet of hydrogen. The proximity of the mixture to auto-ignition has been quantitively explained through the three criteria established in the present work beginning from a fundamental static approach to more elaborate and conservative transient and integral approaches.

The static criterion employs the use of an explosion limit with a threshold iso-τ_{ID} value of 1 ms. GCR values with peak thermodynamic states on the right of this threshold explosion limit were defined to be unsafe while those on the left as safe. This criterion showed that for a constant GCR, the probability of autoignition is an order of magnitude more sensitive to T_i than p_i. For a stochiometric H_2-air mixture and $GCR = 20$, even a 25% increase in p_i (1 bar to 1.25 bar) still presented a safe condition whereas a mere $< 2\%$ increase in T_i (300 K to 305 K) rendered the mixture to be just marginally safe. An analogous deduction can be made from this result pertaining to the existence of hot spots, around which strong temperature gradients exist, causing a possible premature ignition of the mixture. To consider a broader range of more realistic peak states, influenced by the non-ideal behaviour of the gas during compression, the parameter ε with a range from 0.7 to 1.1 was introduced. It was also discussed that a safe condition might be rendered unsafe in the case of contamination of H_2-air mixture with even a minute amount of a hydrocarbon-based lubricating oil surrogate modifying the explosion limit both in shape and position on the $p - T$ plot.

The second time-based approach supersedes the static criterion because of its ability to evaluate instantaneous τ_{ID} of the charge as both p and T evolve during a compression stroke. This was made possible by fitting an interpolation surface over the H_2 reactivity map developed in the first stage. This approach allowed a more detailed use of the engine geometrical parameters like bore, stroke, conrod length along with the engine speed to translate τ_{ID} as a function of time and therefore the Crank Angle Degree (CAD). This approach, named as the tangency criterion ($t_{TDC} \leq \tau_{ID}$), is particularly helpful in identifying an unsafe condition close to the TDC where the piston displacement is much slower at the end of the stroke allowing a longer time for the charge to evolve into an autoignition.

The only limitation of the tangency criterion to not be a final definitive criterion is its inability to consider the accumulation of any heat release that occurs during the compression stroke as the p, T values rise promoting the initiation of the various reactions involving the species contributing to H_2 combustion. This limitation was identified during the comparison of autoignition scenarios using the tangency criterion with those achieved from alternate 0-D real-gas compression simulations with detailed chemistry. This effect of cumulative heat release was incorporated into a third criterion of the present work, namely, the “integral criterion”. The Livengood-Wu integral, I, was utilized in calculating the onset (i.e., the CAD) of auto-ignition as the mixture is compressed until TDC and then also expanded beyond that. This criterion gives a more conservative approach to the selection of a MSGCR and therefore evaluates the unsafe GCR values that might have been determined to be safe by the “tangency criterion”. Three unique cases of

autoignition around the TDC were analysed. The “integral criterion” clearly recognizes unsafe autoignition conditions that are deemed safe by the “tangency criterion”. This criterion also further validates the autoignition CAD (θ_{AI}) values simulated through the 0-D real gas compression simulations. The criterion was further expanded to include the entire ε range from 0.7 to 1.1 to consider the infinite possibilities of the occurrence of an auto-ignition event in the case of a real engine making the criterion more robust and inclusive.

In the present work the applicability of the “integral criterion” is encouraged to both Compression Ignition (CI) and Spark-Ignition (SI) HICEs. It may seem straight forward to be used in CI engines however for SI engines, it may be questioned because of the added dynamics of the flame front propagation and therefore the criterion’s ability to predict an ignition either pre-spark (pre-ignition) or post-spark (end-gas autoignition). Despite the added complexity due to a propagating flame, this criterion can still be confidently used to clearly identify, at least in a preliminary analysis, when to initiate the spark. A way to avoid pre-ignition can be to design the engine parameters such that the integral I does not achieve a value of 1 before the spark timing. A possible way to predict end-gas autoignition, however, could be made possible by a modification of the integral I taking into consideration the reduction of the unburnt volume as the flame propagates towards the cylinder walls.

As a synergy of Chapters 2 and 3 of present work, an analytical expression for MSGCR was developed as a function of fundamental variables p_i, T_i, and ϕ validated for stochiometric ($\phi = 1$) to very lean ($\phi = 0.1$) mixture compositions as well as intake conditions from atmospheric ($p_i = 1\ bar$, $T_i = 300\ K$) to a typical turbocharged and non-intercooled intake condition ($p_i = 1.5\ bar$, $T_i = 400\ K$). As observed, MSGCR does not vary much with ϕ except for $\phi < 0.3$. Once again, the intake temperature was the predominant parameter that significantly affected the MSGCR. The fundamental conclusion which can be reached from this analysis is that for the successful feasibility of safe HICE operation, the control of the in-cylinder temperature is most crucial. One has to be mindful that the analytical correlation developed in this study has its assumptions of adiabatic walls, absence of hot-spot and statistical uncertainties like cyclic effects. Such realities will be incorporated in future works. The analyses performed in this work provide a solid foundation of selected engine geometry parameters and operating conditions that, on a preliminary design phase, would be sufficient to ensure a safe operation for a HICE paving the way to faster prototypes for test bench experiments and validation.

The analysis conducted in this chapter 4 of the present work had the aim of ascertaining if a lubricant oil droplet can promote undesired self-ignition of the charge in hydrogen Internal Combustion Engines (ICEs). Namely, a one-dimensional analytical model was coupled with the OpenSMOKE++ open-source chemical code with the purpose of assessing ignition delay variations of the charge induced by the presence of oil vapour. The analytical model was developed to derive reasonable thermo-chemical conditions in the vicinity of a vaporizing lubricant oil droplet, while the latter is suspended in a H_2/air environment in which engine-like conditions reign. The obtained results were used as input parameters for performing zero-dimensional numerical simulations in the OpenSMOKE++ framework. A single surrogate chemical species was employed to model the chemical and physical behaviour of lubricant oil, namely, n-hexadecane (n-$C_{16}H_{34}$). A reduced chemical model, developed in a previous work for emulating the reactivity properties of H_2/n-$C_{16}H_{34}/air$ mixtures, was used in the chemical kinetic simulations.

The results clearly confirmed that the oil vapour significatively increases the charge reactivity. It was found that the charge ignition delay reaches a minimum in the region close to the droplet surface, where its value can be reduced by up to two orders of magnitude, independently of the droplet radius and the equivalence ratio of the H_2/air mixture surrounding the droplet. Such a behaviour has been observed also in thermodynamic conditions that would not allow hydrogen to ignite. The reason relies on the low-temperature chemistry involved in the oxidation of long straight-chained alkanes constituting lubricant oil. This might explain how certain abnormal combustion modes can arise in hydrogen ICEs even in the absence of any significant charge or temperature inhomogeneity.

Despite the relative simplicity of the model employed in the calculations, it was possible to provide an answer to the question posed in the title via a practical approach that required limited computational efforts. The potentially harmful influence that lubricant oil might have on combustion regularity in hydrogen ICEs has been unveiled, with the results suggesting that an oil droplet can effectively serve as a “sensitive” spot able to initiate an undesired ignition event that can potentially propagate to the remainder of the charge. Having assessed the importance of studying the fuel-lubricant interaction, more accurate calculations as well as experimental campaigns (also including secondary paths by which lubricant oil can interfere with the combustion process) might be now performed in order to provide more insight on the issue and accelerate the development of hydrogen combustion technology for ICEs.

Finally in chapter 5, the 1D transient detonation simulations observed for exponential temperature gradients within the hot spot, indicated the need to thoroughly study such aspects if a robust design of a HICE is required, free from abnormal combustion events. The results from the simulations in this work provides the qualitative idea to explore multiple different possibilities of temperature gradients that could rise to a different behaviour of detonation modes in engine relevant conditions.

Further steps are required to deepen the understanding of prevalent pre-ignition phenomenon in HICEs through detailed yet still fundamental studies taking into consideration all important parameters like peak thermodynamic states, compression ratio, stochastic analysis of the contamination of lubricant oil in the fresh charge in relation to parameters such as engine speed and geometrical tolerances. Comprehensive yet computationally cheap solutions can be found just through fundamental chemical kinetic analysis of the H_2-air combustion, lubricant oil vaporization modelling and detonating hot spots analysis.

Publications

Significant parts of this Ph.D. thesis have been published by the author beforehand in a journal paper and a conference proceeding. All these relevant prior printed publications are registered according to the valid doctoral regulations and listed below. However, not all of them are quoted explicitly everywhere as they are part of this present work being official documents. Whether these personal prior printed publications were referenced, depended on maintaining comprehensibility and providing all necessary context.

Distaso, Elia, Daniyal Altaf Baloch, Giuseppe Calò, Riccardo Amirante, and Paolo Tamburrano. "A chemical-kinetics-based approach for the preliminary design of hydrogen internal combustion engines." Energy Conversion and Management 315 (2024): 118736.

Distaso, E., G. Calò, R. Amirante, D. A. Baloch, P. De Palma, and P. Tamburrano. "Can lubricant oil promote undesired self-ignition of the charge in hydrogen engines?." In Journal of Physics: Conference Series, vol. 2648, no. 1, p. 012084. IOP Publishing, 2023.

Bibliography

[1] European Commission, “European Green deal.” [Online]. Available: https://commission.europa.eu/strategy-and-policy/priorities-2019-2024/european-green-deal_en

[2] E. Distaso *et al.*, “Analysis of the Combustion Process in a Lean-Burning Turbulent Jet Ignition Engine Fueled with Methane,” *Energy Convers Manag*, vol. 223, p. 113257, 2020.

[3] M. Olcuire, C. Iacovano, A. d’Adamo, S. Breda, T. Lucchini, and S. Fontanesi, “Combustion modelling of turbulent jet ignition in a divided combustion chamber,” *International Journal of Engine Research*, vol. 23, no. 11, pp. 1937–1953, 2022, doi: 10.1177/14680874211037118.

[4] I. Pielecha, J. Merkisz, P. Urbański, D. Gallas, and M. Andrych-Zalewska, “A Numerical Study of the Effect of Hydrogen Fuelled Turbulent Jet Ignition Engine,” in *SAE Powertrains, Fuels & Lubricants Conference & Exhibition*, SAE International, Aug. 2022. doi: https://doi.org/10.4271/2022-01-1007.

[5] W. P. Attard, N. Fraser, P. Parsons, and E. Toulson, “A Turbulent Jet Ignition Pre-Chamber Combustion System for Large Fuel Economy Improvements in a Modern Vehicle Powertrain,” *SAE Int J Engines*, vol. 3, no. 2, pp. 20–37, 2010, [Online]. Available: http://www.jstor.org/stable/26275544

[6] R. Mobasheri, A. Aitouche, Z. Peng, and X. Li, “Influence of Oxy-Fuel Combustion on Engine Operating Conditions and Combustion Characteristics in a High Speed Direct Injection (HSDI) Diesel Engine under Homogenous Charge Compression Ignition (HCCI) Mode,” in *WCX SAE World Congress Experience*, SAE International, Apr. 2020. doi: https://doi.org/10.4271/2020-01-1138.

[7] R. Diwakar and S. Singh, “Importance of Spray-Bowl Interaction in a DI Diesel Engine Operating under PCCI Combustion Mode,” in *SAE World*

Congress & Exhibition, SAE International, Apr. 2009. doi: https://doi.org/10.4271/2009-01-0711.

[8] S. Nüesch, E. Hellström, L. Jiang, and A. G. Stefanopoulou, "Mode switches among SI, SACI, and HCCI combustion and their influence on drive cycle fuel economy," in *2014 American Control Conference*, 2014, pp. 849–854. doi: 10.1109/ACC.2014.6858954.

[9] A. P. Singh, V. Kumar, and A. K. Agarwal, "Evaluation of comparative engine combustion, performance and emission characteristics of low temperature combustion (PCCI and RCCI) modes," *Appl Energy*, vol. 278, p. 115644, 2020, doi: https://doi.org/10.1016/j.apenergy.2020.115644.

[10] L. F. Ineza Havugimana, B. Liu, F. Liu, J. Zhang, B. Li, and P. Wan, "Review of Artificial Intelligent Algorithms for Engine Performance, Control, and Diagnosis," *Energies (Basel)*, vol. 16, no. 3, p. 1206, Jan. 2023, doi: 10.3390/en16031206.

[11] A. Norouzi, H. Heidarifar, M. Shahbakhti, C. R. Koch, and H. Borhan, "Model Predictive Control of Internal Combustion Engines: A Review and Future Directions," *Energies (Basel)*, vol. 14, no. 19, p. 6251, Oct. 2021, doi: 10.3390/en14196251.

[12] R. Amirante, C. Casavola, E. Distaso, and P. Tamburrano, "Towards the Development of the In-Cylinder Pressure Measurement Based on the Strain Gauge Technique for Internal Combustion Engines," *SAE Technical Paper 2015-24-2419*, 2015, doi: https://doi.org/10.4271/2015-24-2419.

[13] M. Bunce, A. Cairns, S. Krishna Pothuraju Subramanyam, N. Peters, and H. Blaxill, "The Influence of Charge Motion on Pre-Chamber and Main Chamber Combustion in a Highly Dilute Jet Ignition Engine," *Front Mech Eng*, vol. 6, 2021, [Online]. Available: https://www.frontiersin.org/articles/10.3389/fmech.2020.629243

[14] X. Zhao, R. Liu, H. Wang, Z. Zheng, and M. Yao, "Effects of charge motion on knocking combustion under boosted high load condition of a medium-duty gasoline engine," *Fuel*, vol. 326, p. 125040, 2022, doi: https://doi.org/10.1016/j.fuel.2022.125040.

[15] B. Korb, K. Kuppa, H. D. Nguyen, F. Dinkelacker, and G. Wachtmeister, "Experimental and numerical investigations of charge motion and combustion in lean-burn natural gas engines," *Combust Flame*, vol. 212, pp. 309–322, 2020, doi: https://doi.org/10.1016/j.combustflame.2019.11.005.

[16] B. Mohan, W. Yang, and S. kiang Chou, "Fuel injection strategies for performance improvement and emissions reduction in compression ignition engines—A review," *Renewable and Sustainable Energy Reviews*, vol. 28, pp. 664–676, 2013, doi: https://doi.org/10.1016/j.rser.2013.08.051.

[17] T. Simpson and C. Depcik, "Multiple Fuel Injection Strategies for Compression Ignition Engines," *Energies (Basel)*, vol. 15, no. 14, 2022, doi: 10.3390/en15145214.

[18] R. Amirante, C. Coratella, E. Distaso, G. Rossini, and P. Tamburrano, "Optical device for measuring the injectors opening in common rail systems," *International Journal of Automotive Technology*, vol. 18, no. 4, pp. 729–742, 2017, doi: https://doi.org/10.1007/s12239-017-0072-y.

[19] S. Marelli and V. Usai, "Experimental analysis and 1D simulation of an advanced hybrid boosting system for automotive applications in transient operation," *International Journal of Engine Research*, vol. 24, no. 2, pp. 639–651, Feb. 2023, doi: 10.1177/14680874211060173.

[20] Y. He, D. Sun, J. Liu, and B. Zhu, "Optimization of a turbocharger and supercharger compound boosting system for a Miller cycle engine," *Proceedings of the Institution of Mechanical Engineers, Part D: Journal of Automobile Engineering*, vol. 232, no. 2, pp. 238–253, Feb. 2018, doi: 10.1177/0954407017695136.

[21] S. Meer, M. Mallampati, A. RamaRao, S. Anantha, and P. Balu, "Compression ignition of Hydrogen (H2) in a direct injection diesel engine Modified to operate as a Low Heat Rejection," *YMER Digital*, vol. 21, pp. 180–189, Mar. 2022, doi: 10.37896/YMER21.02/19.

[22] M. Pochet, H. Jeanmart, and F. Contino, "A 22:1 Compression Ratio Ammonia-Hydrogen HCCI Engine: Combustion, Load, and Emission Performances," *Front Mech Eng*, vol. 6, pp. 1–16, Mar. 2020, doi: 10.3389/fmech.2020.00043.

[23] Q. Luo and B. Sun, "Experiments on the effect of engine speed, load, equivalence ratio, spark timing and coolant temperature on the energy balance of a turbocharged hydrogen engine," *Energy Convers Manag*, vol. 162, pp. 1–12, Mar. 2018, doi: 10.1016/j.enconman.2017.12.051.

[24] R. Sierens and E. Rosseel, "Backfire mechanism in a carburetted hydrogen fuelled engine," in *HYDROGEN ENERGY PROGRESS XII, VOLS 1-3*, J. C. Bolcich and T. N. Veziroglu, Eds., INT ASSOC HYDROGEN ENERGY, 1998, pp. 1537–1546.

[25] G. A. Karim, "Hydrogen as a spark ignition engine fuel," *Int J Hydrogen Energy*, vol. 28, no. 5, pp. 569–577, 2003, doi: https://doi.org/10.1016/S0360-3199(02)00150-7.

[26] J. Gao, X. Wang, P. Song, G. Tian, and C. Ma, "Review of the backfire occurrences and control strategies for port hydrogen injection internal combustion engines," *Fuel*, vol. 307, p. 121553, 2022, doi: https://doi.org/10.1016/j.fuel.2021.121553.

[27] S. J. Navale, R. R. Kulkarni, and S. S. Thipse, "An experimental study on performance, emission and combustion parameters of hydrogen fueled spark ignition engine with the timed manifold injection system," *Int J Hydrogen Energy*, vol. 42, no. 12, pp. 8299–8309, 2017, doi: https://doi.org/10.1016/j.ijhydene.2017.01.059.

[28] K. V Shivaprasad, R. Rajesh, W. A. Wogasso, B. Nigatu, and F. Addisu, "Usage of Hydrogen as a Fuel in Spark Ignition Engine," *IOP Conf Ser Mater Sci Eng*, vol. 376, no. 1, p. 12037, Jun. 2018, doi: 10.1088/1757-899X/376/1/012037.

[29] P. M. Diéguez, J. C. Urroz, D. Sáinz, J. Machin, M. Arana, and L. M. Gandía, "Characterization of combustion anomalies in a hydrogen-fueled 1.4 L commercial spark-ignition engine by means of in-cylinder pressure, block-engine vibration, and acoustic measurements," *Energy Convers Manag*, vol. 172, pp. 67–80, 2018, doi: https://doi.org/10.1016/j.enconman.2018.06.115.

[30] Y. Zhenzhong, W. Lijun, H. Manlou, and C. Yongdi, "Research on optimal control to resolve the contradictions between restricting abnormal combustion and improving power output in hydrogen fueled engines," *Int J Hydrogen Energy*, vol. 37, no. 1, pp. 774–782, 2012, doi: https://doi.org/10.1016/j.ijhydene.2011.04.062.

[31] T. Tsujimura and Y. Suzuki, "The utilization of hydrogen in hydrogen/diesel dual fuel engine," *Int J Hydrogen Energy*, vol. 42, no. 19, pp. 14019–14029, 2017, doi: https://doi.org/10.1016/j.ijhydene.2017.01.152.

[32] E. Distaso, R. Amirante, G. Calò, P. De Palma, P. Tamburrano, and R. D. Reitz, "Investigation of Lubricant Oil influence on Ignition of Gasoline-like Fuels by a Detailed Reaction Mechanism," *Energy Procedia*, vol. 148, pp. 663–670, 2018, doi: https://doi.org/10.1016/j.egypro.2018.08.155.

[33] M. Kassai *et al.*, "Research on the effect of lubricant oil and fuel properties on LSPI occurrence in boosted SI engines," 2016.

[34] T. Kuboyama, Y. Moriyoshi, and K. Morikawa, "Visualization and analysis of LSPI mechanism caused by oil droplet, particle and deposit in highly

boosted SI combustion in low speed range," *SAE Int J Engines*, vol. 8, no. 2015-01–0761, pp. 529–537, 2015.

[35] E. Distaso, R. Amirante, G. Calò, P. De Palma, and P. Tamburrano, "Lubricant-Oil-Induced Pre-ignition Phenomena in Modern Gasoline Engines: Using Experimental Data and Numerical Chemistry to Develop a Practical Correlation," *SAE Tech. paper 2021-24-0052*, 2021, doi: 10.4271/2021-24-0052.Abstract.

[36] E. Distaso, R. Amirante, G. Calò, P. De Palma, P. Tamburrano, and R. D. Reitz, "Predicting lubricant oil induced pre-ignition phenomena in modern gasoline engines: The reduced GasLube reaction mechanism," *Fuel*, vol. 281, p. 118709, 2020, doi: https://doi.org/10.1016/j.fuel.2020.118709.

[37] E. Distaso, G. Calò, R. Amirante, D. A. Baloch, P. De Palma, and P. Tamburrano, "Can lubricant oil promote undesired self-ignition of the charge in hydrogen engines?," in *Journal of Physics: Conference Series*, 2023, p. 12084.

[38] E. Distaso *et al.*, "Highlighting the Role of Lubricant Oil in the Development of Hydrogen Internal Combustion Engines by means of a Kinetic Reaction Model," *J Phys Conf Ser*, vol. 2385, no. 1, p. 12078, Dec. 2022, doi: 10.1088/1742-6596/2385/1/012078.

[39] R. Amirante *et al.*, "Effects of lubricant oil on particulate emissions from port-fuel and direct-injection spark-ignition engines," *International Journal of Engine Research*, vol. 18, no. 5–6, pp. 606–620, 2017, doi: https://doi.org/10.1177/1468087417706602.

[40] R. Amirante *et al.*, "Experimental Investigations on the Sources of Particulate Emission within a Natural Gas Spark-Ignition Engine," *SAE Tech Pap 2017-24-0141*, 2017, doi: https://doi.org/10.4271/2017-24-0141.

[41] E. Distaso, R. Amirante, P. Tamburrano, and R. D. Reitz, "Understanding the role of soot oxidation in gasoline combustion: A numerical study on the effects of oxygen enrichment on particulate mass and number emissions in a spark-ignition engine," *Energy Convers Manag*, vol. 184, pp. 24–39, 2019, doi: https://doi.org/10.1016/j.enconman.2019.01.022.

[42] R. Amirante *et al.*, "Effects of natural gas composition on performance and regulated, greenhouse gas and particulate emissions in spark-ignition engines," *Energy Convers Manag*, vol. 143, pp. 338–347, 2017, doi: https://doi.org/10.1016/j.enconman.2017.04.016.

[43] E. Distaso, R. Amirante, P. Tamburrano, and R. D. Reitz, "Steady-state Characterization of Particle Number Emissions from a Heavy-Duty Euro VI Engine Fueled with Compressed Natural Gas," *Energy Procedia*, vol. 148, pp. 671–678, 2018, doi: https://doi.org/10.1016/j.egypro.2018.08.156.

[44] E. Distaso, R. Amirante, G. Calò, P. De Palma, and P. Tamburrano, "Evolution of Soot Particle Number, Mass and Size Distribution along the Exhaust Line of a Heavy-Duty Engine Fueled with Compressed Natural Gas," *Energies (Basel)*, vol. 13, no. 15, p. 3993, 2020, doi: 10.3390/en13153993.

[45] C. D. MILLER, "Roles of Detonation Waves and Autoignition in Spark - Ignition Engine Knock as Shown by Photographs Taken at 40,000 and 200,000 Frames Per Sec," in *Pre-1964 SAE Technical Papers*, SAE International, Jan. 1947. doi: https://doi.org/10.4271/470207.

[46] Z. Wang, H. Liu, and R. D. Reitz, "Knocking combustion in spark-ignition engines," *Prog Energy Combust Sci*, vol. 61, pp. 78–112, 2017.

[47] A. H. Willbourn, D. Phil, and C. N. Hinshelwood, "The mechanism of the hydrogen-oxygen reaction I. The third explosion limit," *Proc R Soc Lond A Math Phys Sci*, vol. 185, no. 1003, pp. 353–369, 1946, doi: 10.1098/rspa.1946.0023.

[48] B. Bahri, M. Shahbakhti, K. Kannan, and A. A. Aziz, "Identification of ringing operation for low temperature combustion engines," *Appl Energy*, vol. 171, pp. 142–152, Jun. 2016, doi: 10.1016/j.apenergy.2016.03.033.

[49] R. K. Maurya and M. R. Saxena, "Characterization of Ringing Operation in Ethanol-Fueled HCCI Engine Using Chemical Kinetics and Artificial Neural Network," in *Advances in Internal Combustion Engine Research*, D. K. Srivastava, A. K. Agarwal, A. Datta, and R. K. Maurya, Eds., Singapore: Springer Singapore, 2018, pp. 43–61. doi: 10.1007/978-981-10-7575-9_3.

[50] R. K. Maurya and M. R. Saxena, "Characterization of ringing intensity in a hydrogen-fueled HCCI engine," *Int J Hydrogen Energy*, vol. 43, no. 19, pp. 9423–9437, 2018, doi: https://doi.org/10.1016/j.ijhydene.2018.03.194.

[51] B. Lewis and G. von Elbe, *Combustion, Flames and Explosions of Gases*. Elsevier, 1987. doi: 10.1016/c2009-0-21751-x.

[52] G. Mittal, C.-J. Sung, and R. A. Yetter, "Autoignition of H2/CO at elevated pressures in a rapid compression machine," *Int J Chem Kinet*, vol. 38, no. 8, pp. 516–529, 2006.

[53] C.-J. Sung and H. J. Curran, "Using rapid compression machines for chemical kinetics studies," *Prog Energy Combust Sci*, vol. 44, pp. 1–18, 2014, doi: https://doi.org/10.1016/j.pecs.2014.04.001.

[54] E. Hu, L. Pan, Z. Gao, X. Lu, X. Meng, and Z. Huang, "Shock tube study on ignition delay of hydrogen and evaluation of various kinetic models," *Int J Hydrogen Energy*, vol. 41, no. 30, pp. 13261–13280, 2016.

[55] ANSYS Reaction Design, "ANSYS CHEMKIN Pro 17.2," 2016, *ANSYS Reaction Design, San Diego*: 17.2. Accessed: Apr. 17, 2024. [Online]. Available: https://www.ansys.com/products/fluids/ansys-chemkin-pro

[56] X. Wang and C. K. Law, "An analysis of the explosion limits of hydrogen-oxygen mixtures," *J Chem Phys*, vol. 138, no. 13, p. 134305, 2013.

[57] A. Kéromnès *et al.*, "An experimental and detailed chemical kinetic modeling study of hydrogen and syngas mixture oxidation at elevated pressures," *Combust Flame*, vol. 160, no. 6, pp. 995–1011, 2013.

[58] W. Liang, J. Liu, and C. K. Law, "On explosion limits of H2/CO/O2 mixtures," *Combust Flame*, vol. 179, pp. 130–137, 2017.

[59] K. J. Laidler, "A glossary of terms used in chemical kinetics, including reaction dynamics (IUPAC Recommendations 1996)," *Pure and Applied Chemistry*, vol. 68, no. 1, pp. 149–192, Jan. 1996, doi: 10.1351/pac199668010149.

[60] "modified Arrhenius equation," 2014, *International Union of Pure and Applied Chemistry (IUPAC)*. doi: 10.1351/goldbook.m03963.

[61] A. E. Lutz, R. J. Kee, J. A. Miller, H. A. Dwyer, and A. K. Oppenheim, "Dynamic effects of autoignition centers for hydrogen and C1,2-hydrocarbon fuels," *Symposium (International) on Combustion*, vol. 22, no. 1, pp. 1683–1693, 1989, doi: https://doi.org/10.1016/S0082-0784(89)80181-X.

[62] D. Bradley, "Autoignitions and detonations in engines and ducts," *Philosophical transactions of the Royal Society A.*, vol. 370, pp. 689–714, 2012, doi: 10.1098/rsta.2011.0367.

[63] X. J. Gu, D. R. Emerson, and D. Bradley, "Modes of reaction front propagation from hot spots," *Combust Flame*, vol. 133, no. 1, pp. 63–74, 2003, doi: https://doi.org/10.1016/S0010-2180(02)00541-2.

[64] R. Modiyani *et al.*, "Effect of intake valve closure modulation on effective compression ratio and gas exchange in turbocharged multi-cylinder engines

utilizing EGR," *International Journal of Engine Research - INT J ENGINE RES*, vol. 12, pp. 617–631, May 2011, doi: 10.1177/1468087411415180.

[65] C. M. White, R. R. Steeper, and A. E. Lutz, "The hydrogen-fueled internal combustion engine: a technical review," *Int J Hydrogen Energy*, vol. 31, no. 10, pp. 1292–1305, 2006.

[66] F. E. Lynch, "Parallel induction: a simple fuel control method for hydrogen engines," *Int J Hydrogen Energy*, vol. 8, no. 9, pp. 721–730, 1983.

[67] J. M. G. Antunes, R. Mikalsen, and A. P. Roskilly, "An experimental study of a direct injection compression ignition hydrogen engine," *Int J Hydrogen Energy*, vol. 34, no. 15, pp. 6516–6522, 2009.

[68] P. G. Aleiferis and M. F. Rosati, "Controlled autoignition of hydrogen in a direct-injection optical engine," *Combust Flame*, vol. 159, no. 7, pp. 2500–2515, 2012.

[69] S. Welscher *et al.*, "A Detailed Reaction Kinetics-Based Calculation Tool for Internal Combustion Engine-Related Ignition Processes," 2022.

[70] J. B. Heywood, *Internal Combustion Engine Fundamentals*, 2nd edition. New York: McGraw-Hill Education, 2018. [Online]. Available: https://www.accessengineeringlibrary.com/content/book/9781260116106

[71] J. C. Livengood and P. C. Wu, "Correlation of autoignition phenomena in internal combustion engines and rapid compression machines," *Symposium (International) on Combustion*, vol. 5, no. 1, pp. 347–356, 1955, doi: https://doi.org/10.1016/S0082-0784(55)80047-1.

[72] D. Robertson and R. Prucka, "A Review of Spark-Assisted Compression Ignition (SACI) Research in the Context of Realizing Production Control Strategies," *SAE Technical Paper 2019-24-0027*, 2019.

[73] A. Paykani, A.-H. Kakaee, P. Rahnama, and R. D. Reitz, "Progress and recent trends in reactivity-controlled compression ignition engines," *International Journal of Engine Research*, vol. 17, no. 5, pp. 481–524, 2016.

[74] E. Toulson, H. J. Schock, and W. P. Attard, "A Review of Pre-Chamber Initiated Jet Ignition Combustion Systems," *SAE Technical Paper Series*, vol. 1, 2010, doi: 10.4271/2010-01-2263.

[75] E. Distaso *et al.*, "Analysis of the Combustion Process in a Lean-Burning Turbulent Jet Ignition Engine Fueled with Methane," *Energy Convers Manag*, vol. 223, p. 113257, 2020.

[76] E. Distaso *et al.*, "Experimental and Numerical Analysis of a Pre-Chamber Turbulent Jet Ignition Combustion System," *SAE Technical paper 2019-24-0018*, 2019, doi: https://doi.org/10.4271/2019-24-0018.

[77] A. Di Mauro, H. Chen, and V. Sick, "Neural network prediction of cycle-to-cycle power variability in a spark-ignited internal combustion engine," *Proceedings of the Combustion Institute*, vol. 37, no. 4, pp. 4937–4944, 2019.

[78] V. Ravaglioli, F. Ponti, M. De Cesare, F. Stola, F. Carra, and E. Corti, "Combustion Indexes for Innovative Combustion Control," *SAE Int J Engines*, vol. 10, no. 5, pp. 2371–2381, 2017.

[79] T. Kuronita *et al.*, "A Study of Dynamic Combustion Control for High Efficiency Diesel Engine," *SAE Technical Paper 2020-01-0297*, 2020.

[80] R. Amirante, C. Casavola, E. Distaso, and P. Tamburrano, "Towards the Development of the In-Cylinder Pressure Measurement Based on the Strain Gauge Technique for Internal Combustion Engines," *SAE Technical Paper 2015-24-2419*, 2015, doi: https://doi.org/10.4271/2015-24-2419.

[81] B. Ashok, S. D. Ashok, and C. R. Kumar, "A review on control system architecture of a SI engine management system," *Annu Rev Control*, vol. 41, pp. 94–118, 2016.

[82] R. Amirante, C. Coratella, E. Distaso, G. Rossini, and P. Tamburrano, "Optical device for measuring the injectors opening in common rail systems," *International Journal of Automotive Technology*, vol. 18, no. 4, pp. 729–742, 2017, doi: https://doi.org/10.1007/s12239-017-0072-y.

[83] W. Eckerle, V. Sujan, and G. Salemme, "Future Challenges for engine manufacturers in view of future emissions legislation," *SAE Technical paper 2017-01-1923*, 2017, doi: https://doi.org/10.4271/2017-01-1923.

[84] R. Amirante, E. Distaso, P. Tamburrano, and R. D. Reitz, "Laminar Flame Speed Correlations for Methane, Ethane, Propane and their Mixtures, and Natural Gas and Gasoline for Spark-Ignition Engine Simulations," *International Journal of Engine Research*, vol. 18, no. 9, pp. 951–970, 2017, doi: https://doi.org/10.1177/1468087417720018.

[85] S. E. Hosseini and B. Butler, "An overview of development and challenges in hydrogen powered vehicles," *Int J Green Energy*, vol. 17, no. 1, pp. 13–37, 2020.

[86] M. Faizal *et al.*, "Review of hydrogen fuel for internal combustion engines," *Journal of Mechanical Engineering Research and Developments*, vol. 42, no. 3, pp. 35–46, 2019.

[87] H. L. Yip *et al.*, "A review of hydrogen direct injection for internal combustion engines: Towards carbon-free combustion," *Applied Sciences*, vol. 9, no. 22, pp. 1–30, 2019, doi: 10.3390/app9224842.

[88] H. Xu *et al.*, "Experimental and numerical investigation on effects of pre-ignition positions on knock intensity of hydrogen fuel," *Int J Hydrogen Energy*, vol. 46, no. 52, pp. 26631–26645, 2021, doi: 10.1016/j.ijhydene.2021.05.154.

[89] S. K. Aggarwal, O. Awomolo, and K. Akber, "Ignition characteristics of heptane-hydrogen and heptane-methane fuel blends at elevated pressures," *Int J Hydrogen Energy*, vol. 36, no. 23, pp. 15392–15402, 2011, doi: 10.1016/j.ijhydene.2011.08.065.

[90] F. C.-Y. Wang and L. Zhang, "Chemical composition of group II lubricant oil studied by high-resolution gas chromatography and comprehensive two-dimensional gas chromatography," *Energy & Fuels*, vol. 21, no. 6, pp. 3477–3483, 2007.

[91] J.-M. Zaccardi and D. Escudié, "Overview of the main mechanisms triggering low-speed pre-ignition in spark-ignition engines," *International Journal of Engine Research*, vol. 16, no. 2, pp. 152–165, 2015.

[92] Z. Wang, H. Liu, and R. D. Reitz, "Knocking combustion in spark-ignition engines," *Prog Energy Combust Sci*, vol. 61, pp. 78–112, 2017.

[93] E. Distaso, R. Amirante, G. Calò, P. De Palma, P. Tamburrano, and R. D. Reitz, "Investigation of Lubricant Oil influence on Ignition of Gasoline-like Fuels by a Detailed Reaction Mechanism," *Energy Procedia*, vol. 148, pp. 663–670, 2018, doi: https://doi.org/10.1016/j.egypro.2018.08.155.

[94] M. Amann and T. Alger, "Lubricant reactivity effects on gasoline spark ignition engine knock," *SAE Int J Fuels Lubr*, vol. 5, no. 2012-01–1140, pp. 760–771, 2012.

[95] J. Gao, X. Wang, P. Song, G. Tian, and C. Ma, "Review of the backfire occurrences and control strategies for port hydrogen injection internal combustion engines," *Fuel*, vol. 307, no. x, p. 121553, 2022, doi: 10.1016/j.fuel.2021.121553.

[96] L. Rouleau, F. Duffour, B. Walter, R. Kumar, and L. Nowak, "Experimental and Numerical Investigation on Hydrogen Internal Combustion Engine," *SAE Tech.Papers*, no. 2021, 2021, doi: 10.4271/2021-24-0060.

[97] R. Amirante *et al.*, "Effects of lubricant oil on particulate emissions from port-fuel and direct-injection spark-ignition engines," *International Journal*

of Engine Research, vol. 18, no. 5–6, pp. 606–620, 2017, doi: https://doi.org/10.1177/1468087417706602.

[98] R. Amirante *et al.*, "Experimental Investigations on the Sources of Particulate Emission within a Natural Gas Spark-Ignition Engine," *SAE Tech Pap 2017-24-0141*, 2017, doi: https://doi.org/10.4271/2017-24-0141.

[99] E. Distaso, R. Amirante, G. Calò, P. De Palma, and P. Tamburrano, "Evolution of Soot Particle Number, Mass and Size Distribution along the Exhaust Line of a Heavy-Duty Engine Fueled with Compressed Natural Gas," *Energies (Basel)*, vol. 13, no. 15, p. 3993, 2020, doi: 10.3390/en13153993.

[100] E. Distaso, R. Amirante, P. Tamburrano, and R. D. Reitz, "Steady-state Characterization of Particle Number Emissions from a Heavy-Duty Euro VI Engine Fueled with Compressed Natural Gas," *Energy Procedia*, vol. 148, pp. 671–678, 2018, doi: https://doi.org/10.1016/j.egypro.2018.08.156.

[101] E. Distaso, R. Amirante, P. Tamburrano, and R. D. Reitz, "Understanding the role of soot oxidation in gasoline combustion: A numerical study on the effects of oxygen enrichment on particulate mass and number emissions in a spark-ignition engine," *Energy Convers Manag*, vol. 184, pp. 24–39, 2019, doi: https://doi.org/10.1016/j.enconman.2019.01.022.

[102] Y. Huang, Y. Li, W. Zhang, F. Meng, and Z. Guo, "3D simulation study on the influence of lubricant oil droplets on pre-ignition in turbocharged DISI engines," *Proceedings of the Institution of Mechanical Engineers, Part D: Journal of Automobile Engineering*, vol. 232, no. 12, pp. 1677–1693, 2018.

[103] M. Ohtomo, T. Suzuoki, H. Miyagawa, M. Koike, N. Yokoo, and K. Nakata, "Fundamental analysis on auto-ignition condition of a lubricant oil droplet for understanding a mechanism of low-speed pre-ignition in highly charged spark-ignition engines," *International Journal of Engine Research*, vol. 20, no. 3, pp. 292–303, 2019.

[104] E. Distaso, R. Amirante, G. Calò, P. De Palma, and P. Tamburrano, "Lubricant-Oil-Induced Pre-ignition Phenomena in Modern Gasoline Engines: Using Experimental Data and Numerical Chemistry to Develop a Practical Correlation," *SAE Tech. paper 2021-24-0052*, 2021, doi: 10.4271/2021-24-0052.Abstract.

[105] A. Gupta *et al.*, "Relative Impact of Chemical and Physical Properties of the Oil-Fuel Droplet on Pre-Ignition and Super-Knock in Turbocharged Gasoline Engines," 2016.

[106] E. Distaso, R. Amirante, G. Calò, P. De Palma, P. Tamburrano, and R. D. Reitz, "Predicting Lubricant Oil Induced Pre-Ignition Phenomena in Modern Gasoline Engines: the Reduced GasLube Reaction Mechanism," *Fuel*, vol. 281, p. 118709, 2020.

[107] S. Palaveev, M. Magar, H. Kubach, R. Schiessl, U. Spicher, and U. Maas, "Premature flame initiation in a Turbocharged DISI engine - Numerical and experimental investigations," *SAE Int J Engines*, vol. 6, no. 1, pp. 54–66, 2013, doi: 10.4271/2013-01-0252.

[108] O. A. Kuti *et al.*, "A fundamental investigation into the relationship between lubricant composition and fuel ignition quality," *Fuel*, vol. 160, pp. 605–613, 2015.

[109] E. Distaso *et al.*, "Highlighting the Role of Lubricant Oil in the Development of Hydrogen Internal Combustion Engines by means of a Kinetic Reaction Model," in *Journal of Physics: Conference Series*, 2022, p. 12078.

[110] H. Zhang and C. K. Law, "Effects of temporally varying liquid-phase mass diffusivity in multicomponent droplet gasification," *Combust Flame*, vol. 153, no. 4, pp. 593–602, 2008.

[111] C. K. Law and F. A. Williams, "Kinetics and convection in the combustion of alkane droplets," *Combust Flame*, vol. 19, no. 3, pp. 393–405, 1972.

[112] A. Y. Snegirev, "Transient temperature gradient in a single-component vaporizing droplet," *Int J Heat Mass Transf*, vol. 65, pp. 80–94, 2013.

[113] H. Zhang and C. K. Law, "Effects of temporally varying liquid-phase mass diffusivity in multicomponent droplet gasification," *Combust Flame*, vol. 153, no. 4, pp. 593–602, 2008.

[114] S. A. Monogenidou, M. J. Assael, and M. L. Huber, "Reference Correlation for the Thermal Conductivity of n-Hexadecane from the Triple Point to 700 K and up to 50 MPa," *J Phys Chem Ref Data*, vol. 47, no. 1, p. 13103, 2018.

[115] T. N. Abramenko, V. I. Aleinikova, L. E. Golovicher, and N. E. Kuz'mina, "Generalization of experimental data on thermal conductivity of nitrogen, oxygen, and air at atmospheric pressure," *Journal of engineering physics and thermophysics*, vol. 63, no. 3, pp. 892–897, 1992.

[116] T. L. Bergman, T. L. Bergman, F. P. Incropera, D. P. Dewitt, and A. S. Lavine, *Fundamentals of heat and mass transfer*. John Wiley \& Sons, 2011.

[117] S. Mathur, P. K. Tondon, and S. C. Saxena, "Thermal conductivity of binary, ternary and quaternary mixtures of rare gases," *Mol Phys*, vol. 12, no. 6, pp. 569–579, 1967.

[118] V. P. Zhukov and M. Pätz, "On thermal conductivity of gas mixtures containing hydrogen," *Heat and Mass Transfer*, vol. 53, pp. 2219–2222, 2017.

[119] T. N. Abramenko, V. I. Aleinikova, L. E. Golovicher, and N. E. Kuz'mina, "Generalization of experimental data on thermal conductivity of nitrogen, oxygen, and air at atmospheric pressure," *Journal of engineering physics and thermophysics*, vol. 63, no. 3, pp. 892–897, 1992.

[120] T. L. Bergman, T. L. Bergman, F. P. Incropera, D. P. Dewitt, and A. S. Lavine, *Fundamentals of heat and mass transfer*. John Wiley \& Sons, 2011.

[121] W. M. Haynes, *CRC handbook of chemistry and physics*. CRC press, 2016.

[122] B. T. Johnson, G. K. Hargrave, B. A. Reid, V. J. Page, and others, "Optical analysis and measurement of crankcase lubricant oil atomisation," 2012.

[123] Z. Wang, D. Zhang, Y. Fang, M. Song, Z. Gong, and L. Feng, "Experimental and numerical investigation of the auto-ignition characteristics of cylinder oil droplets under low-speed two-stroke natural gas engines in-cylinder conditions," *Fuel*, vol. 329, p. 125498, 2022.

[124] A. Cuoci, M. Mehl, G. Buzzi-Ferraris, T. Faravelli, D. Manca, and E. Ranzi, "Autoignition and burning rates of fuel droplets under microgravity," *Combust Flame*, vol. 143, no. 3, pp. 211–226, 2005.

[125] B. Thirouard and T. Tian, "Oil transport in the piston ring pack (Part I): identification and characterization of the main oil transport routes and mechanisms," 2003.

[126] Y. Long *et al.*, "Effect of Oil and Gasoline Properties on Pre-Ignition and Super-Knock in a Thermal Research Engine (TRE) and an Optical Rapid Compression Machine (RCM)," 2016.

[127] A. Cuoci, A. Frassoldati, T. Faravelli, and E. Ranzi, "OpenSMOKE++: An object-oriented framework for the numerical modeling of reactive systems with detailed kinetic mechanisms," *Comput Phys Commun*, vol. 192, pp. 237–264, 2015.

[128] Z. Zheng *et al.*, "Study on the flame development patterns and flame speeds from homogeneous charge to stratified charge by fueling n-heptane in an optical engine," *Combust Flame*, vol. 199, pp. 213–229, 2019, doi: https://doi.org/10.1016/j.combustflame.2018.10.027.

[129] Ya. B. Zeldovich, "Regime classification of an exothermic reaction with nonuniform initial conditions," *Combust Flame*, vol. 39, no. 2, pp. 211–214, 1980, doi: https://doi.org/10.1016/0010-2180(80)90017-6.

[130] X. J. Gu, D. R. Emerson, and D. Bradley, "Modes of reaction front propagation from hot spots," *Combust Flame*, vol. 133, no. 1, pp. 63–74, 2003, doi: https://doi.org/10.1016/S0010-2180(02)00541-2.

[131] J. Rudloff, J.-M. Zaccardi, S. Richard, and J. M. Anderlohr, "Analysis of pre-ignition in highly charged SI engines: Emphasis on the auto-ignition mode," *Proceedings of the Combustion Institute*, vol. 34, no. 2, pp. 2959–2967, 2013, doi: https://doi.org/10.1016/j.proci.2012.05.005.

[132] O. Dounia, O. Vermorel, A. Misdariis, and T. Poinsot, "Influence of kinetics on DDT simulations," *Combust Flame*, vol. 200, pp. 1–14, 2019, doi: https://doi.org/10.1016/j.combustflame.2018.11.009.

[133] M. A. Liberman, A. D. Kiverin, and M. F. Ivanov, "Regimes of chemical reaction waves initiated by nonuniform initial conditions for detailed chemical reaction models," *Phys Rev E*, vol. 85, no. 5, p. 56312, May 2012, doi: 10.1103/PhysRevE.85.056312.

[134] P. Dai, Z. Chen, S. Chen, and Y. Ju, "Numerical experiments on reaction front propagation in n-heptane/air mixture with temperature gradient," *Proceedings of the Combustion Institute*, vol. 35, no. 3, pp. 3045–3052, 2015, doi: https://doi.org/10.1016/j.proci.2014.06.102.

[135] P. Dai and Z. Chen, "Effects of NOx addition on autoignition and detonation development in DME/air under engine-relevant conditions," *Proceedings of the Combustion Institute*, vol. 37, no. 4, pp. 4813–4820, 2019, doi: https://doi.org/10.1016/j.proci.2018.06.063.

[136] T. Zhang, W. Sun, and Y. Ju, "Multi-scale modeling of detonation formation with concentration and temperature gradients in n-heptane/air mixtures," *Proceedings of the Combustion Institute*, vol. 36, no. 1, pp. 1539–1547, 2017, doi: https://doi.org/10.1016/j.proci.2016.06.192.

[137] J. Pan, L. Chen, H. Wei, D. Feng, S. Deng, and G. Shu, "On autoignition mode under variable thermodynamic state of internal combustion engines," *International Journal of Engine Research*, vol. 21, no. 5, pp. 856–865, Sep. 2018, doi: 10.1177/1468087418796617.

[138] J. Pan, H. Wei, G. Shu, Z. Chen, and P. Zhao, "The role of low temperature chemistry in combustion mode development under elevated pressures,"

Combust Flame, vol. 174, pp. 179–193, 2016, doi: https://doi.org/10.1016/j.combustflame.2016.09.012.

[139] J. Pan, L. Wang, W. Liang, C. K. Law, H. Wei, and G. Shu, "Multi-regime reaction front and detonation initiation by temperature inhomogeneity," *Proceedings of the Combustion Institute*, vol. 39, no. 4, pp. 4929–4937, 2023, doi: https://doi.org/10.1016/j.proci.2022.07.260.

[140] J. Pan, L. Wang, D. Yi, W. Liang, C. K. Law, and H. Wei, "Identification of multi-regime detonation development for hydrocarbon fuels," *Combust Flame*, vol. 255, p. 112864, 2023, doi: https://doi.org/10.1016/j.combustflame.2023.112864.

[141] L. Bates and D. Bradley, "Deflagrative, auto-ignitive, and detonative propagation regimes in engines," *Combust Flame*, vol. 175, pp. 118–122, 2017.

[142] D. Bradley and G. T. Kalghatgi, "Influence of autoignition delay time characteristics of different fuels on pressure waves and knock in reciprocating engines," *Combust Flame*, vol. 156, no. 12, pp. 2307–2318, 2009.

[143] J. Rudloff, J.-M. Zaccardi, S. Richard, and J. M. Anderlohr, "Analysis of pre-ignition in highly charged SI engines: Emphasis on the auto-ignition mode," *Proceedings of the Combustion Institute*, vol. 34, no. 2, pp. 2959–2967, 2013.

[144] J. Pan, H. Wei, G. Shu, Z. Chen, and P. Zhao, "The role of low temperature chemistry in combustion mode development under elevated pressures," *Combust Flame*, vol. 174, pp. 179–193, 2016.

[145] A. Robert, S. Richard, O. Colin, and T. Poinsot, "LES study of deflagration to detonation mechanisms in a downsized spark ignition engine," *Combust Flame*, vol. 162, no. 7, pp. 2788–2807, 2015.

[146] Y. B. Zeldovich, "Regime Classification of an Exothermic Reaction with Nonuniform Initial Conditions," 1980.

[147] X. J. Gu, D. R. Emerson, and D. Bradley, "Modes of reaction front propagation from hot spots," *Combust Flame*, vol. 133, no. 1–2, pp. 63–74, 2003.

[148] J. Pan, L. Wang, W. Liang, C. K. Law, H. Wei, and G. Shu, "Multi-regime reaction front and detonation initiation by temperature inhomogeneity," *Proceedings of the Combustion Institute*, vol. 39, no. 4, pp. 4929–4937, Jan. 2023.

[149] P. Dai, Z. Chen, and X. Gan, "Autoignition and detonation development induced by a hot spot in fuel-lean and CO2 diluted n-heptane/air mixtures," *Combust Flame*, vol. 201, pp. 208–214, 2019.

[150] A. E. Lutz, R. J. Kee, J. A. Miller, H. A. Dwyer, and A. K. Oppenheim, "Dynamic effects of autoignition centers for hydrogen and C1, 2-hydrocarbon fuels," in *Symposium (International) on combustion*, 1989, pp. 1683–1693.

[151] D. Bradley, "Autoignitions and detonations in engines and ducts," *Philosophical Transactions of the Royal Society A: Mathematical, Physical and Engineering Sciences*, vol. 370, no. 1960, pp. 689–714, 2012.

[152] L. Bates, D. Bradley, G. Paczko, and N. Peters, "Engine hot spots: Modes of auto-ignition and reaction propagation," *Combust Flame*, vol. 166, pp. 80–85, 2016.

[153] A. K. Kapila, D. W. Schwendeman, J. J. Quirk, and T. Hawa, "Mechanisms of detonation formation due to a temperature gradient," *Combustion Theory and Modelling*, vol. 6, no. 4, p. 553, 2002.

[154] P. Dai, C. Qi, and Z. Chen, "Effects of initial temperature on autoignition and detonation development in dimethyl ether/air mixtures with temperature gradient," *Proceedings of the Combustion Institute*, vol. 36, no. 3, pp. 3643–3650, 2017.

[155] J. Pan, L. Chen, H. Wei, D. Feng, S. Deng, and G. Shu, "On autoignition mode under variable thermodynamic state of internal combustion engines," *International Journal of Engine Research*, vol. 21, no. 5, pp. 856–865, Jun. 2020.

[156] J. Zhang, M. B. Luong, and H. G. Im, "Detonation peninsula of different stoichiometric ammonia/hydrogen/air mixtures under engine-relevant conditions," *Combust Flame*, vol. 253, Jul. 2023, doi: 10.1016/j.combustflame.2023.112793.

[157] Y. Gao, P. Dai, and Z. Chen, "Numerical studies on autoignition and detonation development from a hot spot in hydrogen/air mixtures," *Combustion Theory and Modelling*, vol. 24, no. 2, pp. 245–261, Mar. 2020, doi: 10.1080/13647830.2019.1674923.

[158] J. Pan, L. Wang, D. Yi, W. Liang, C. K. Law, and H. Wei, "Identification of multi-regime detonation development for hydrocarbon fuels," *Combust Flame*, vol. 255, p. 112864, 2023.

[159] J. Sun, Y. Wang, B. Tian, and Z. Chen, "detonationFoam: An open-source solver for simulation of gaseous detonation based on OpenFOAM," *Comput*

Phys Commun, vol. 292, p. 108859, 2023, doi: https://doi.org/10.1016/j.cpc.2023.108859.

[160] Z. Chen, M. P. Burke, and Y. Ju, "Effects of Lewis number and ignition energy on the determination of laminar flame speed using propagating spherical flames," *Proceedings of the Combustion Institute*, vol. 32, no. 1, pp. 1253–1260, 2009, doi: https://doi.org/10.1016/j.proci.2008.05.060.

La borsa di dottorato è stata cofinanziata con risorse del Programma Operativo Nazionale Ricerca e Innovazione 2014-2020, risorse FSE REACT-EU
Azione IV.4 "Dottorati e contratti di ricerca su tematiche dell'innovazione"
e
Azione IV.5 "Dottorati su tematiche Green"